# Investigation of Optical Cavity Modes and Ultrafast Carrier Dynamics in ZnO Rods Using Second-Harmonic Generation and Transient Absorption Pump-Probe Microscopy

Brian Peter Mehl

A dissertation submitted to the faculty of the University of North Carolina at Chapel Hill in partial fulfillment of the requirements for the degree of Doctor of Philosophy in the Department of Chemistry

Chapel Hill
2011

Approved by:

Dr. Chris Fecko (chair)

Dr. John Papanikolas

Dr. Tomas Baer

Dr. Mark Schoenfisch

Dr. Sergei Sheiko

## ABSTRACT

Brian Peter Mehl: Investigation of Optical Cavity Modes and Ultrafast Carrier Dynamics in ZnO Rods Using Second-Harmonic Generation and Transient Absorption Pump-Probe Microscopy
(Under the direction of John M. Papanikolas)

The polydispersity intrinsic to nanoscale and microscale semiconductor materials poses a major challenge to using individual objects as building blocks for device applications. The ability to manipulate the shape of ZnO structures is enormous, making it an ideal material for studying shape-dependent phenomena. We have built a nonlinear microscope used to directly image optical cavity modes in ZnO rods using second-harmonic generation. Images of second-harmonic generation in needle-shaped ZnO rods obtained from individual structures show areas of enhanced second-harmonic intensity along the longitudinal axis of the rod that are periodically distributed and symmetrically situated relative to the rod midpoint. The spatial modulation is a direct consequence of the fundamental optical field coupling into standing wave resonator modes of the ZnO structure, leading to an enhanced backscattered second-harmonic condition that cannot be achieved in bulk ZnO. A more complicated second-harmonic image is observed when excitation is below the band gap, which is attributed to whispering gallery modes. Additionally, the nonlinear microscope was combined with transient absorption pump-probe to follow the electron-hole recombination dynamics at different points within individual needle-shaped ZnO rods to characterize spatial differences in dynamical behavior. The results from pump-

probe experiments are correlated with spatially resolved ultrafast emission measurements, and scanning electron microscopy provides structural details. Dramatically different electron-hole recombination dynamics are observed in the narrow tips compared to the interior, with the ends exhibiting a greater propensity for electron-hole plasma formation and faster recombination of carriers across the band gap that stem from a physical confinement of the charge carriers. In the interior of the rod, a greater fraction of the electron-hole recombination is trap-mediated and occurs on a significantly longer time scale.

*To my family and friends.*

## ACKNOWLEDGEMENTS

First and foremost, I wish to express my gratitude and thanks to Dr. John Papanikolas for his infinite advice and patience in my unflagging pursuit of transient absorption pump-probe microscopy. I am also indebted to Dr. Ralph House for his initial trailblazing, construction and evolution of the optical table. Additional recognition is required for Justin Kirschbrown for his assistance at the SEM and development of an upgraded data acquisition program. Last but not least, I would like to thank the rest of the Papanikolas past, current and future members; especially Dr. Brittany Westlake, Dr. Kyle Brennaman, and Stephanie Bettis. The primary funding from this project came from a grant from the National Science Foundation (CHE-0809045). The project also made use of instrumentation purchased by the UNC-EFRC on Solar Fuels and Next Generation Photovoltaics, an Energy Frontier Research Center funded by the U.S. Department of Energy, Office of Science, Office of Basic Energy Sciences under Award Number DE-SC0001011.

## TABLE OF CONTENTS

## LIST OF TABLES

## LIST OF FIGURES

## LIST OF ABBREVIATIONS

| | |
|---|---|
| AOM | acousto-optic modulator |
| BE | band edge emission |
| CCD | charged-coupled device |
| DC | direct current |
| DFG | difference frequency generation |
| e-h | electron-hole |
| EHP | electron-hole plasma |
| FDFD | finite difference frequency domain |
| FDTD | finite difference time domain |
| FLIM | fluorescence lifetime imaging microscopy |
| FP | Fabry-Pérot |
| FRET | fluorescence resonance energy transfer |
| LBO | lithium triborate |
| MCP | microchannel plate |
| NSOM | near-field scanning microscopy |
| OPO | optical parametric oscillator |
| PLL | phase-locked loop |
| PSD | phase sensitive detector |
| rf | radio frequency |
| SEM | scanning electron microscopy |
| SFG | sum frequency generation |
| SHG | second-harmonic generation |
| STM | scanning tunneling microscopy |
| TEM | transmission electron microscopy |
| WGM | whispering gallery mode |

## LIST OF SYMBOLS

| | |
|---|---|
| $a$ | second-order nonlinearity proportionality constant (Chapter 2) |
| $a$ | radius of aperture (Chapter 3) |
| $\alpha$ | polarizability |
| $a_B^{ex}$ | exciton Bohr radius |
| $a_B^H$ | hydrogen Bohr radius |
| $A_i$ | amplitude of $i^{th}$ component |
| $A^{(2)}$ | autocorrelation intensity from a second-order nonlinear process |
| $A_{FRAC}$ | fringed resolved autocorrelation intensity |
| $b$ | third-order nonlinearity proportionality constant |
| $\beta$ | two-photon absorption coefficient |
| $c$ | speed of light in vacuum |
| $d$ | diameter of aperture (Chapter 3) |
| $d$ | diameter of a diffraction limited spot |
| $d_0$ | diameter of optical beam waist inside modulator |
| $d_1$ | diameter of optical beam waist input |
| $d_{FP}$ | diameter of Fabry Pérot cavity from hexagon (smallest) |
| $d_r$ | diameter of hexagon (largest) |
| $\mathbf{D}$ | displacement field vector |
| $D_b$ | diameter of Gaussian beam |
| $D_t$ | diameter of limiting aperture |
| $e$ | charge of electron |
| $\mathbf{E}$ | electric field vector |
| $E(k)$ | energy dispersion |
| $E_{at}$ | atomic electric field |
| $E_b$ | exciton binding energy |
| $E_{ex}$ | energy of exciton |
| $E_g$ | energy of band gap |
| $\Delta E_g$ | energy shift in band gap |

| | |
|---|---|
| $E_{sig}^{(2)}$ | electric field cross correlation from a second-order nonlinear process |
| $E_+$ | energy band from positively traveling wavefunction |
| $E_-$ | energy band from negatively traveling wavefunction |
| $\varepsilon(\omega)$ | complex dielectric function |
| $\varepsilon_0$ | vacuum permittivity constant |
| $\varepsilon_1$ | real component of dielectric function |
| $\varepsilon_2$ | imaginary component of dielectric function |
| $\varepsilon_b$ | background dielectric constant |
| $f$ | oscillator strength (Chapter 2) |
| $f$ | frequency of acoustic wave (Chapter 3) |
| $f/\#$ | f-number |
| $f_{-3dB}$ | -3 dB frequency of filter |
| $F$ | cavity finesse |
| $F_{electric}$ | static electric force |
| $F_{restoring}$ | restoring force |
| $\gamma$ | damping constant |
| $\mathbf{H}$ | magnetic field vector |
| $I$ | intensity |
| $I_{sig}^{(2)}$ | intensity cross correlation from a second-order nonlinear process |
| $I_\omega$ | intensity of fundamental |
| $I_{2\omega}$ | intensity of second-harmonic |
| $IPSF$ | illumination point spread function |
| $J_1(x)$ | Bessel function of the first kind |
| $k$ | wavevector |
| $k_{bind}$ | binding strength |
| $k_B$ | Boltzmann constant |
| $\Delta k$ | phase mismatch |
| $\boldsymbol{K}$ | total translational wavevector |
| $K$ | diameter proportionality constant |
| $\kappa$ | imaginary component of index of refraction: absorption coefficient |
| $l_c$ | critical screening length |

| | |
|---|---|
| $l_s$ | screening length |
| $\Delta l$ | diffraction limited distance between two Airy disks |
| $L$ | interaction length |
| $L_c$ | coherence length |
| $\lambda$ | wavelength |
| $m$ | integer number (Chapter 5) |
| $m_e$ | effective mass of electron |
| $m_h$ | effective mass of hole |
| $m_0$ | free electron mass |
| $M$ | total translational mass |
| $\mu$ | reduced mass |
| $\mu$ | dipole moment |
| $\mu_0$ | permeability of vacuum |
| $n$ | real component of index of refraction |
| $\tilde{n}$ | complex index of refraction |
| $n_0$ | linear refractive index |
| $n_1$ | index of refraction outside |
| $n_2$ | index of refraction inside (Chapter 5) |
| $n_2$ | nonlinear index of refraction |
| $n_m$ | Mott density |
| $n_p$ | number of charge carrier pairs |
| $NA$ | numerical aperture |
| $N$ | microscopic dipoles per unit volume |
| $p_+$ | probability density |
| $p_-$ | probability density |
| $\mathbf{P}$ | polarization vector |
| $P^{(2)}$ | second-order polarization |
| $P_L$ | power loss |
| $P_{NL}$ | nonlinear polarization |
| $r_s$ | shift in band gap energy |
| $R$ | distance between aperature and far field images |
| $Ry^*$ | Rydberg energy:  exciton binding energy |

| | |
|---|---|
| $s$ | length of side of cross section |
| $t_c$ | time constant |
| $t_r$ | modulation rise time |
| $T$ | temperature |
| $T$ | trunctation ratio |
| $\tau$ | time delay |
| $\theta$ | angle observed in far-field |
| $\theta_B$ | Bragg diffraction angle |
| $U(\tilde{x})$ | potential energy |
| $v$ | acoutic velocity |
| $V_{in}$ | voltage input |
| $V_{out}$ | voltage output |
| $V(\overrightarrow{r_e} - \overrightarrow{r_h})$ | Yukawa potential |
| $V_{TPE}$ | 2-photon emission volume |
| $v_g$ | group velocity |
| $\omega$ | resonant angular frequency |
| $\omega_0$ | resonant angular frequency |
| $\omega_L$ | longitudinal mode frequency |
| $\omega_{xy}$ | diffraction limited lateral |
| $\omega_z$ | diffraction limited axial |
| $\phi$ | phase component |
| $\tilde{x}$ | displacement from equilibrium |
| $\chi$ | electric susceptibility |
| $\chi^{(1)}$ | linear susceptibility |
| $\chi^{(2)}$ | second-order nonlinearity susceptibility |
| $\chi^{(3)}$ | third-order nonlinearity susceptibility |
| $\chi_r^{(3)}$ | real component of third-order nonlinear susceptibility |
| $\chi_i^{(3)}$ | imaginary component of third-order nonlinear susceptibility |
| $\psi$ | waveform |
| $\psi_+$ | wavefunction |
| $\psi_-$ | wavefunction |

# CHAPTER 1. INTRODUCTION

Knowledge of the physical processes that provide materials their unique properties is of utmost importance for advancing technological innovations. Understanding of underlying phenomena permits intelligent design of properties achieving enhanced performance in all applications. Spectroscopy has become an indispensible instrument for uncovering optical and electronic properties of materials through observations of electro-magnetic radiation and matter interactions.[1]

The properties of bulk semiconductors have been extensively studied through spectroscopic means.[2] However, with the recent synthetic acceleration of nano-sized architectures (wires, dots, sheets, etc...), new structure dependent phenomena have emerged.[3] Pioneering experiments established that a material's optical and electronic properties can be drastically altered through manipulation of a structure's size and shape.[4,5] Presently, reduction in dimensionalities, quantum confinement effects, and optical microcavities are used for improved performance in nano-optical and nano-electronic devices.[6-9]

However, as technology continues to move towards smaller scales, differences between structures becomes increasingly important and poses a major challenge to those wishing to understand and exploit nanoscience. Continued advances rely on spectroscopic measurements made from single structures removing the characteristic polydispersity within ensemble measurements. Though, this brings up an important question. With increased complexity of individual architectures, along with size and shape dependent properties, does even a perfectly monodisperse sample experience heterogeneous behavior? Does the end of a structure behave differently than the middle? Development of spectroscopic methods used to answer these questions must achieve both temporal and spatial resolution. This project

focuses on answering these questions through spectroscopic development of a time-resolved microscope.

The simplest implementations of specific spectroscopic techniques include steady state absorption and luminescence. The amount of transmission or emission is monitored as a function of incident radiation energy upon a sample. The generated spectra express the energy transitions of the material. However, any dynamical information is hidden in the inherit time integrated measurement. Spectral evolutions are monitored through time-resolved spectroscopic methods. These methods generally are initiated through excitation of the sample with a pulsed laser source and absorption or emission is monitored as a function of time. The incorporation of time-correlation single photon counting [10,11] or streak camera[12] detection are two common techniques. Unfortunately, temporal resolution is ultimately determined by current electronic limitations, typically in the picosecond range.

Increased resolution is achieved through pump-probe measurements.[1] Conceptually a pump pulse excites a sample and a probe pulse is used for monitoring the change in the sample after an adjustable delay time. Here the time resolution is fundamentally limited by the duration of the pump and probe pulses. Temporal resolution of in the femtosecond range are commonly achieved since the inception of pulsed ultrafast Ti:sapphire lasers. Currently, the best time-resolved measurements are achieved with pump-probe techniques. In the proceeding experiments a transient absorption pump-probe technique is employed to ensure superior temporal resolution.

Spatial resolution is obtained in combination with microscopy. Currently, the greatest spatial resolution is observed with electron microscopy. Techniques such as scanning-electron (SEM) and transmission electron (TEM) microscopy employ electron

beams in the imaging process. Resolutions in the nanometer range are easily achieved due to the small characteristic wavelength of electrons. While time-resolved measurements are readily obtainable with cathodoluminescence incorporation of pump-probe methods have proven to be much more difficult and expensive.[13]

Scanning probe microscopies are another convenient method for achieving sub-optical spatial resolutions. Near-field scanning (NSOM)[14,15] and scanning tunneling (STM)[16] employ sub-wavelength sized probes that monitor changes in the near-field. Traditionally, when combined with pump-probe methods a far-field pump is employed.[17,18] Consequently, excitation is uniformly distributed over the whole structure concealing dynamics from localized excitations. However, appealing new sub-diffraction limited sized sources are currently available (~20 nm).[19,20] While these new nanoscopic light sources are very attractive, our initial experiments have utilized optical microscopic techniques in order to avoid additional complexities.

While traditional optical microscopies such as confocal microscopy are limited to the diffraction limit of light they have been applied to the study of a wide variety of problems. Time-resolved confocal methods are typically luminescence based approaches and include fluorescence lifetime imaging (FLIM) and fluorescence resonant energy transfer (FRET).[21] These techniques are heavily relied upon in the biological sciences to observe biological processes due to their ability to be performed on live cells and tissues with minimal invasiveness. In optical microscopy spatial resolution may be increased when nonlinear multi-photon processes are made of use. These methods involve the simultaneous absorption of two or more photons. Consequently, absorption and subsequent emission is localized at the focal point of the objective, eliminating excess background emission.[22] In order to

progress to from ensemble to single structure spectroscopic measurements and start to characterize intra-object heterogeneity a nonlinear microscope was developed in combination with pump-probe capabilities.

ZnO posses several key qualities that makes it an ideal target for single structure microscopy. First, the recent renessiance of ZnO has peaked interest for its potential use in UV-blue optoelectronic, photovoltaic, and laser-based applications. Further, it has a high potential for synthetic manipulation, with a variety of nano- and micro-scale shapes, including nanoparticles, nanowires, ribbons and more complicated tetrapod and flower-shaped structures. Single crystal wires can be synthesized with nanometer-sized diameters and length scales ranging from nanometers to microns, the larger of which are well-matched for the microscopy projects proposed herein. Additionally, ZnO has a large $\chi^{(2)}$ that results in efficient SHG, a large two-photon cross-section that provides flexibility in experimental design, and is photochemically robust, enabling it to withstand intense optical fields.[23]

This dissertation is divided into six chapters. In accordance with the development of the nonlinear microscope, **Chapter 2** contains an overview of nonlinear optics along with specific instances which are utilized within our experiments. These nonlinear processes include second-harmonic generation, two-photon absorption, and the Kerr effect. **Chapter 3** is dedicated to the experimental setup. This encompasses the description of the microscope, acousto-optic modulators, lock-in detection, as well as streak camera operation. Additionally a report of the temporal and spatial resolution of the transient absorption pump-probe microscopy setup is included. **Chapter 4** presents relevant background information on ZnO including its band structure, excitons, and high density effects. Our first result from the development of the nonlinear microscope is presented **Chapter 5**; the direct imaging of

optical cavity modes in ZnO rods using second-harmonic generation. Finally, **Chapter 6** explores the initial characterization of the spatial differences in electron-hole recombination dynamics using transient absorption pump-probe microscopy in needle-shaped ZnO rods.

# CHAPTER 2. NONLINEAR OPTICS

Until the early 1960's, it was unknown that the frequency of light could be altered by passage through a medium. With the recent availability of coherent light sources, it was the discovery of optical second-harmonic generation by Franken et al. in 1961 which ushered in the branch of nonlinear optics.[24] Soon after, experimental demonstrations of sum and difference frequency generation[25], as well as optical parametric amplification[26] and oscillation[27] were revealed. These initial discoveries would have an enormous impact on the future of optics. In fact, countless current optical systems utilize these nonlinear properties including the setup described herein.

Nonlinear behavior requires the interaction of an optical field with matter and is not observed when light travels through free space. In a nonlinear process, the interaction of an optical field with the medium alters its properties which subsequently, causes another optical field or the original field itself to be modified. The following chapter first illustrates the physical origin of nonlinear behavior starting from the harmonic and anharmonic oscillator models. Next, the relationship between the polarization and electric field vectors are explored resulting in a depiction of a nonlinear interaction. Additionally, a specific nonlinear process, second-harmonic generation is discussed. Finally, an introduction to the complex dielectric function and index of refraction are established to relate the third-order nonlinear susceptibility with that of two-photon absorption and the Kerr effect, both of which are essential in obtaining and comprehension of the experimental data. The ideas from the proceeding sections within this chapter have been referenced from various nonlinear optics textbooks.[28-34]

## 2.1. HARMONIC AND ANHARMONIC OSCILLATORS

To understand the origin of nonlinear behavior it is valuable to start with a harmonic oscillator model. In classical mechanics, a harmonic oscillator is a system that when perturbed from its equilibrium experiences a restoring force that is proportional to its displacement from equilibrium, $\tilde{x}$. This linearity, also known as Hooke's law is applied to an electron of charge $e$ and mass bound to a nucleus, where the binding strength between them is described by $k_{bind}$,

$$F_{restoring} = -k_{bind}\tilde{x} \tag{2.1}$$

When a static electric force is applied,

$$F_{electric} = -eE \tag{2.2}$$

where $E$ is the electric field, the dipole moment, $\mu$ becomes displaced,

$$\mu = -e\tilde{x} \tag{2.3}$$

As a result, a new equilibrium distance between the electron and nucleus exists where the two opposing forces are balanced,

$$\tilde{x} = -\frac{eE}{k_{bind}} \tag{2.4}$$

The resulting induced dipole moment is then proportional to the electric field by the following,

$$\mu = \frac{e^2E}{k_{bind}} = \alpha E \tag{2.5}$$

As binding strength, $k_{bind}$ decreases the polarizability, $\alpha$ increases. Consequently, the electron is influenced more by the electric field. Further, the magnitude of the induced dipole moment is linearly proportional to the strength of the electric field.

When an oscillating electric field is applied the binding strength may be described by the mass, $m_0$ and angular frequency, $\omega_0$ of the electron. Subsequently, the potential energy of the electron as a function of displacement from its equilibrium is given by the following,

$$U(\tilde{x}) = -\int F_{restoring} = \frac{1}{2} m_0 \omega_0^2 \tilde{x}^2 \qquad (2.6)$$

Represented as black in Figure 2.1 is the potential energy for an electron bound to a nucleus oscillating at a wavelength of 400 nm. The potential takes the form of parabola, which is a direct consequence of Hooke's law. In reality, Eq. 2.6 is valid only at small applied electric fields. Conversely, when the applied electric field approaches the characteristic atomic electric field ($10^5$-$10^8$ V/m), Hooke's law is violated, such that the restoring force is better described by a power series expansion,

$$F_{restoring} = -m_0 \omega_0^2 \tilde{x} - m_0 a \tilde{x}^2 + m_0 b \tilde{x}^3 + \cdots \qquad (2.7)$$

Constants, $a$ and $b$ correspond to the strength of the second and third-order nonlinearities respectively.

Consider now an anharmonic oscillator where the second-order correction term has been added to the restoring force. The corresponding potential energy function is now given by the following,

$$U(\tilde{x}) = -\int F_{restoring} d\tilde{x} = \frac{1}{2} m_0 \omega_0^2 \tilde{x}^2 + \frac{1}{3} m_0 a \tilde{x}^3 \qquad (2.8)$$

Represented as red in Figure 2.1 is the potential energy described by Eq. 2.8. Compared to the black line (Eq. 2.6), the parabola is now asymmetric. This result is a direct consequence from the violation of Hooke's law with the addition of the second-order correction term. The second-order term in the restoring force is directly related to the second-order nonlinear susceptibility, $\chi^{(2)}$ described below. Further, the potential is a summation of both even and

odd functions. As a result, $U(\tilde{x}) \neq U(-\tilde{x})$ and potentials such as Eq. 2.8 only occur in non-centrosymmetric crystals. Therefore, lacking inversion symmetry is a requirement for any finite value of $\chi^{(2)}$ which is required for nonlinear optical process such as second-harmonic generation.

Now examine an anharmonic oscillator where the third-order correction term has been added to the restoring force. The corresponding potential energy function is given by the following,

$$U(\tilde{x}) = -\int F_{restoring} d\tilde{x} = \frac{1}{2} m_0 \omega_0^2 \tilde{x}^2 - \frac{1}{4} m_0 b \tilde{x}^4 \qquad (2.9)$$

Represented as blue in Figure 2.1 is the potential energy described by Eq. 2.9. Notice the parabola is again symmetric with respect to the equilibrium displacement, a consequence of the summation of two even functions. However, at a large distance away from equilibrium the potential is much lower compared to Eq. 2.6. This result is a direct consequence form the addition of the third-order correction term. The third-order term in the restoring force is directly related to the third-order nonlinear susceptibility, $\chi^{(3)}$ described below. The third-order correction term can give rise to various nonlinear optical behaviors. Important to the proceeding experiments are nonlinear absorption (e.g. two-photon absorption) and refraction (e.g. Kerr effect).

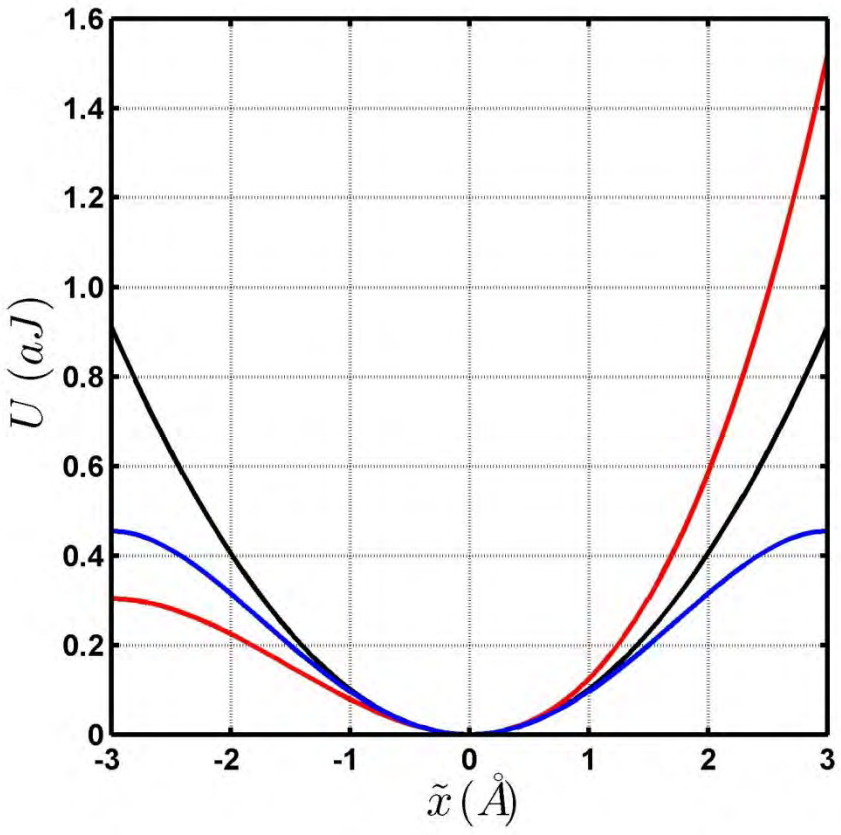


**Figure 2.1:** The potential energy plotted as a function of distance away from equilibrium for an electron bound to a nucleus at three different restoring forces (linear, second-order, and third-order). The parabolic potential from a linear restoring force (Eq. 2.6) is shown in black. The asymmetric parabolic potential from a second-order restoring force (Eq. 2.8) is shown in red. The strength of the second-order nonlinearity was approximated as $a = \omega_0^2/d$. The potential from a third-order restoring force (Eq. 2.9) is shown in blue. The strength of the third-order nonlinearity was approximated as $b = \omega_0^2/d^2$. An oscillation at 400 nm is utilized, with a lattice constant, $d = 3$ Å.

## 2.2. POLARIZATION AND ELECTRIC FIELD VECTORS

The response of the atomic nuclei and their bound electrons from an applied electric field in a dielectric medium result in a collection of induced dipole moments. The induced polarization density, $P$ is defined by the number of microscopic dipoles per unit volume, $N$ and the ensemble average over all of the dipoles, $\mu$ in the medium,

$$P = N\langle\mu\rangle \tag{2.10}$$

The properties of a dielectric medium through which optical fields propagate are described by the relation of the polarization vector and electric field vector, $E$. In a linear medium this induced polarization is related to the electric field by the electric susceptibility $\chi$, a scalar factor that measures how easily the medium is polarized in response to an electric field,

$$P = \varepsilon_0 \chi E \tag{2.11}$$

where $\varepsilon_0$ is the vacuum permittivity constant.

As mentioned above, in systems with large applied electric fields Hooke's law is violated. Accordingly, a relationship between $P$ and $E$ is better expressed in a Taylor series expansion,

$$P = \varepsilon_0\left(\chi^{(1)}E + \chi^{(2)}E^2 + \chi^{(3)}E^3 + \cdots\right) \tag{2.12}$$

where $\chi^{(2)}$ and $\chi^{(3)}$ are the second and third-order nonlinear optical susceptibilities respectively. Displayed in Figure 2.2 is a plot of the polarization as a function of electric field strength for a linear (black), second-order (red), and third-order (blue) correction terms.

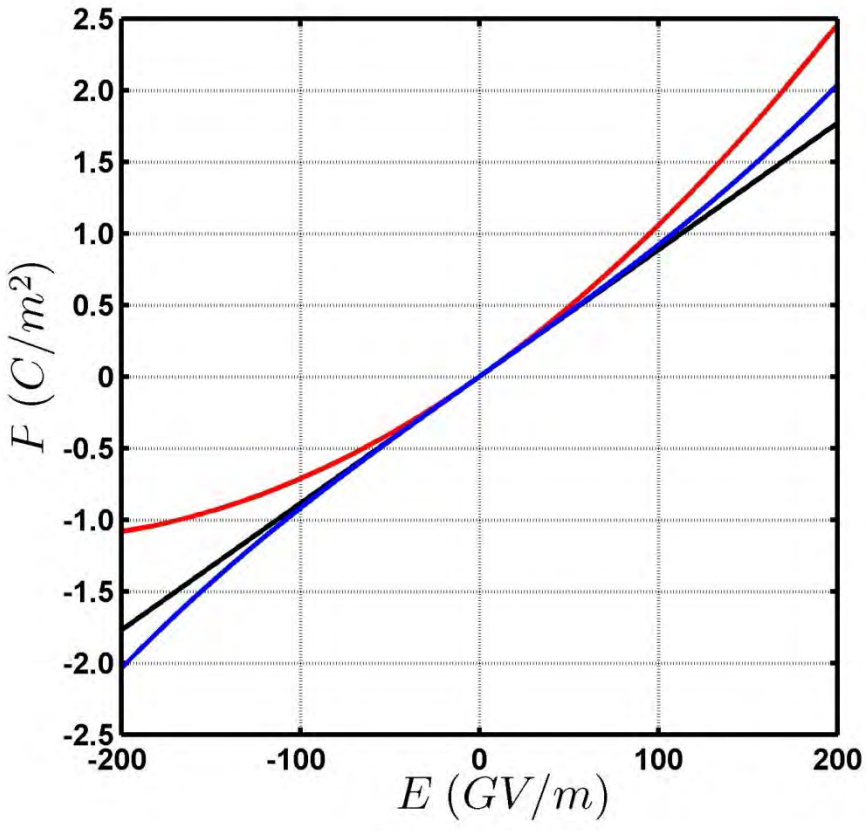


**Figure 2.2**: The polarization as a function of electric field for three different descriptions of the polarization vector: $P = \varepsilon_0 \chi^{(1)}$ (black); $P = \varepsilon_0 \left(\chi^{(1)} E + \chi^{(2)} E^2\right)$ (red); $P = \varepsilon_0 \left(\chi^{(1)} E + \chi^{(3)} E^3\right)$ (blue). The nonlinear components become significant when the applied electric field becomes comparable to the atomic electric fields, $E_{at} = (1/4\pi\varepsilon_0)(e/a_B^2)$. The linear, second-order, and third-order nonlinearities can be approximated by $\chi^{(1)} \approx 1$, $\chi^{(2)} \approx 1/E_{at}$ and $\chi^{(3)} \approx 1/E_{at}^2$ respectively. In the above figure the Bohr radius is utilized, $a_B = 5.29 \times 10^{-11}$ m.

In an isotropic medium, the induced polarization is always parallel to the electric field. However, for anisotropic media the induced polarization depends on both magnitude and direction of the applied electric field. Consequently, these vectors obey tensor relationships. However, for the simplicity of the descriptions below the tensor notations for the second and third-order nonlinearities have been avoided. It is the second and third-order nonlinearities that are responsible for second-harmonic generation, two-photon absorption, and the Kerr effect. All of which are essential components in the proceeding experiments. In the following section is a brief mathematical description deriving the source of nonlinear processes.

## 2.3. NONLINEAR INTERACTION

To mathematically describe the source of the nonlinear interaction consider an electromagnetic wave, $E_0$ of angular frequency, $\omega_0$ and complex amplitude, $A_0$,

$$E_0(t) = A_0 e^{i\omega_0 t} + A_0^* e^{-i\omega_0 t} \tag{2.13}$$

Suppose that this electromagnetic wave is composed of two different frequencies, $\omega_1$ and $\omega_2$ incident on a nonlinear medium,

$$E(t) = A_1 e^{i\omega_1 t} + A_2 e^{i\omega_2 t} + c.c. \tag{2.14}$$

where, $c.c.$ indicates the complex conjugate of the preceding terms. The nonlinear polarization created in response to the electric field (Eq. 2.14) is determined by insertion into Eq. (2.12) limited to the second-order term, $P^{(2)} = \varepsilon_0 \chi^{(2)} E^2$. The result is the following,

$$\begin{aligned} P^{(2)}(t) = \varepsilon_0 \chi^{(2)} \{ [ & A_1^2 e^{i2\omega_1 t} + A_2^2 e^{i2\omega_2 t} + 2A_1 A_2 e^{i(\omega_1+\omega_2)t} \\ & + 2A_1 A_2^* e^{i(\omega_1-\omega_2)t} + c.c] + 2(A_1 A_1^* + A_2 A_2^*) \} \end{aligned} \tag{2.15}$$

The second-order polarization term is composed of various different frequency components. The first and second terms in brackets specify components at $2\omega_1$ and $2\omega_2$ respectively, commonly referred to a second-harmonic generation (SHG). The third and fourth terms specify components at the sum $(\omega_1 + \omega_2)$ and difference $(\omega_1 - \omega_2)$ frequency generation (SFG & DFG) respectively. The last term is a DC term, or sometimes referred to as an optical rectifier. The nonlinear susceptibility amplitudes of various frequency components that arise from Eq. 2.15 are listed below.

(SHG) $$P^{(2)}(2\omega_1) = \varepsilon_0 \chi^{(2)}(2\omega_1; \omega_1, \omega_1) E_1^2 \tag{2.16}$$

(SHG) $$P^{(2)}(2\omega_2) = \varepsilon_0 \chi^{(2)}(2\omega_2; \omega_2, \omega_2) E_2^2 \tag{2.17}$$

(SFG) $$P^{(2)}(\omega_1 + \omega_2) = 2\varepsilon_0 \chi^{(2)}(\omega_1 + \omega_2; \omega_1, \omega_2) E_1 E_2 \tag{2.18}$$

(DFG) $$P^{(2)}(\omega_1 - \omega_2) = 2\varepsilon_0 \chi^{(2)}(\omega_1 - \omega_2; \omega_1, -\omega_2) E_1 E_2^* \tag{2.19}$$

(DC) $$P^{(2)}(0) = 2\varepsilon_0 \chi^{(2)}(0; \omega_1, -\omega_1) E_1 E_1^* + 2\varepsilon_0 \chi^{(2)}(0; \omega_2, -\omega_2) E_2 E_2^* \tag{2.20}$$

Similar equations can be written for the complex conjugates. While all of these nonlinear processes may occur within a medium determination of the dominant process depend on what is referred to as phase matching, which is discussed in proceeding subsection.

### 2.3.1. Second-Harmonic Generation

Second-harmonic generation (SHG) is a second-order nonlinear process in which two photons of equal energy interact within a nonlinear medium and combine to produce a single photon with twice the energy. In order to discuss the basic theoretical description of SHG it is imperative to summon Maxwell's equations in a form which includes the polarization,

$$\nabla \times \mathbf{H} = \frac{\partial \mathbf{D}}{\partial \mathrm{t}} = \frac{\partial}{\partial \mathrm{t}}(\varepsilon_0 \mathbf{E} + \mathbf{P})$$
$$\nabla \times \mathbf{E} = -\frac{\partial}{\partial t}(\mu_0 \mathbf{H}) \tag{2.21}$$

The variables **H**, **D**, **E**, and **P** are the magnetic, displacement, electric, and polarization vectors respectively. Constants $\varepsilon_0$ and $\mu_0$ are the permittivity and permeability of vacuum respectively. As stated earlier, the polarization vector is made of linear and nonlinear components,

$$\mathbf{P} = \varepsilon_0 \chi^{(1)} \mathbf{E} + \mathbf{P}_{NL} \tag{2.22}$$

These equations are the foundation in describing the propagation of light through a dielectric medium. Operation of $\nabla \times$ on both sides of Eq. 2.21 results in a nonlinear wave equation.

$$\nabla^2 \mathbf{E} = \mu_0 \varepsilon \frac{\partial^2 \mathbf{E}}{\partial t^2} + \mu_0 \frac{\partial^2 \mathbf{P}_{NL}}{\partial t^2} \tag{2.23}$$

where

$$\varepsilon = \varepsilon_0 \left(1 + \chi^{(1)}\right)$$

This generalized wave equation will be used as the basis for the theoretical discussion of SHG. It is the nonlinear polarization vector that is the source of the second-harmonic frequency.

In order to solve Eq. 2.23 it is important to reduce the dimensionality to just one dimension. Consider propagation along the z-axis in Cartesian coordinates (i.e. $\partial/\partial x = \partial/\partial y = 0$) at the fundamental ($\omega_1 = \omega_2$) and second-harmonic ($2\omega_1$) frequencies. Secondly, the electric fields are described as linearly-polarized monochromatic plane waves,

$$E_1(\omega_1, z) = A_1(z)e^{i(\omega_1 t - k_1 z)}$$

$$E_2(\omega_2, z) = A_2(z)e^{i(\omega_2 t - k_2 z)} \tag{2.24}$$

where

$$k_j = \frac{2\pi}{\lambda_j} n(\omega_j)$$

In the above equation, $A$ is the amplitude, $k$ is the wave vector, $\lambda$ is the wavelength and $n(\omega)$ is the refractive index at $\omega$. Insertion of Eq. 2.24 into the left hand side of Eq. 2.23 results in the following,

$$\nabla^2 E_2(\omega_2, z) = -\left[k_2^2 A_2 + 2ik_2 \frac{dA_2}{dz} - \frac{d^2 A_2}{dz^2}\right] e^{i(\omega_2 t - k_2 z)} \tag{2.25}$$

A similar equation exists for $E_1(\omega_1, z)$ but is left out for simplicity.

Assuming energy transfer is usually significant only after the wave travels over a distance much longer than their corresponding wavelengths. It is presumed that the amplitude does not vary over small distances. This is known as the slow-varying amplitude approximation, mathematically depicted as,

$$\frac{dA_2}{dz} k_2 \gg \frac{d^2 A_2}{dz^2} \tag{2.26}$$

The physical implication of this assumption is the neglect of the oppositely propagating field generated by $\mathbf{P}_{NL}$. This assumption is poor for nonlinear interactions in a microcavity. Nevertheless, Eq. 2.25 is reduced,

$$\nabla^2 E_2(\omega_2, z) = -\left[k_2^2 A_2 + 2ik_2 \frac{dA_2}{dz}\right] e^{i(\omega_2 t - k_2 z)} \tag{2.27}$$

Now that the left side of Eq. 2.23 may be substituted, consider the $\mathbf{P}_{NL}$ term on the right side. Taking only into account the second-order corrections, the corresponding polarization components of the waves becomes,

$$\mathbf{P}_{NL} = P^{(2)}(2\omega_1, z) = \varepsilon_0 \chi^{(2)}(2\omega_1; \omega_1, \omega_1) A_1^2 e^{i(2\omega_1 t - 2k_1 z)} \qquad (2.28)$$

Substitution of Eq. 2.27 and Eq. 2.28 into the nonlinear wave equation (Eq. 2.23) the amplitude change of $E_2(2\omega_1, z)$ is given by the following using relations: $1/c^2 = \varepsilon_o \mu_0$, $k_j = n_j \omega_j / c$, and $k_j^2 = \omega_j^2 \mu_0 \varepsilon$.

$$\frac{dA_2(z)}{dz} = -\frac{i\omega_1}{n_{(2\omega_1)} c} \chi^{(2)}(2\omega_1; \omega_1, \omega_1) A_1^2(z) e^{i\Delta k z}$$

where (2.29)

$$\Delta k = k_2 - 2k_1 = \frac{4\pi}{\lambda_1}\left[n_{(2\omega_1)} - n_{(\omega_1)}\right]$$

The phase mismatch, $\Delta k$ is proportional to the refractive index difference at frequencies $2\omega_1$ and $\omega_1$. Assuming that the amplitude lost from $E_1(\omega_1, z)$ is insignificant (i.e. $A_1(z) \approx 0$) and that the amplitude of second-harmonic at the start of interaction is negligible (i.e. $A_2(0) \approx 0$). The change in amplitude of $E_2(2\omega_1, z)$ becomes,

$$A_2(z) = -\frac{i\omega_1}{\mathrm{n}_{(2\omega_1)}} \chi^{(2)} A_1^2(0) L \frac{sin\, \Delta k/2}{\Delta k/2} e^{i\Delta k L/2} \qquad (2.30)$$

where $L$ is the interaction length within the material. Consequently, the intensity change of the second-harmonic wave is given by,

$$I_2(z) \propto A_2 A_2^* \propto I_1^2(0) L^2 \left(\frac{sin\, \Delta k/2}{\Delta k/2}\right)^2 \qquad (2.31)$$

The intensity of the second-harmonic is proportional to the square of the intensity of the fundamental as well as the length of the interaction. The term in parenthesis is the phase-matching term. If $\Delta k \neq 0$, the driving polarization, $P^{(2)}(2\omega_1)$ goes in and out of phase with the generated second-harmonic wave and conversion from the fundamental to the second-harmonic oscillates as $sin(\Delta \mathrm{kL}/2)$. The maximum crystal length that is useful in producing

the second-harmonic is defined as the coherence length, $L_c = \frac{\pi}{\Delta k}$. Plotted in Figure 2.3 is the normalized SHG efficiency as a function of the distance within a medium. As the phase mismatch is reduced the efficiency is increased. Therefore, it is essential to minimize the phase mismatch between the fundamental and second-harmonic frequencies for the largest efficiencies.

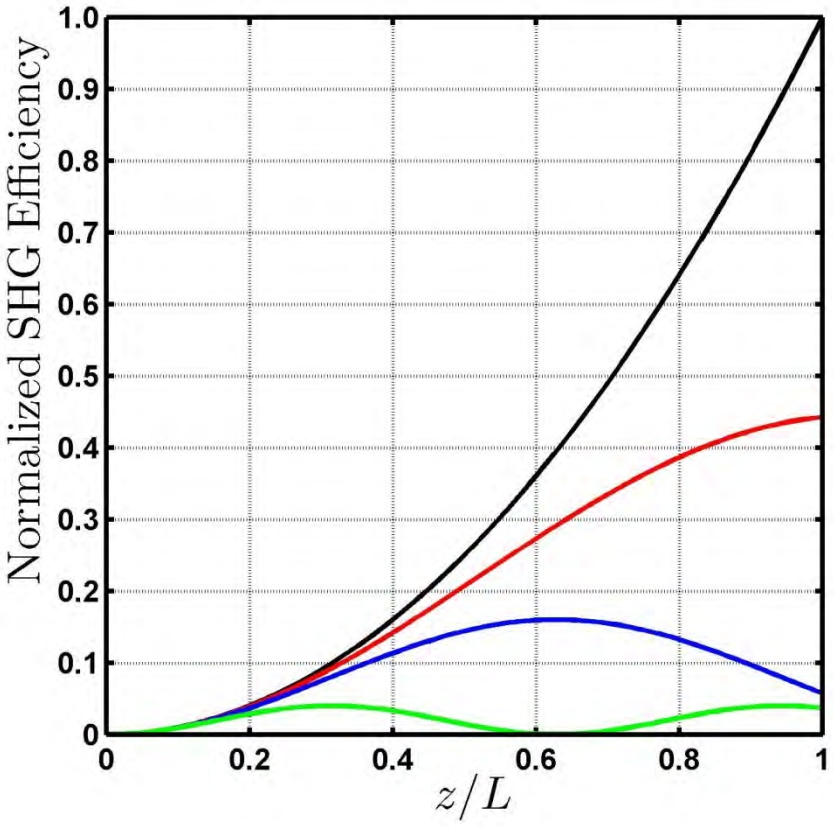


**Figure 2.3:** The normalized SHG efficiency as a function of the distance, $z$ within a medium of length, $L$ at four different phase matching values, $\Delta kL = 0, 3, 5, 10$ (black, red, blue, green). For perfect phase-matching $\Delta kL = 0$, and the efficiency goes as $z^2$. An increase in phase matching drastically enhances the efficiency of the SHG.

## 2.4. COMPLEX DIELECTRIC AND INDEX OF REFRACTION

In addition to second-order susceptibilities observed in second-harmonic generation, third-order susceptibilities are apparent in nonlinear absorption and refraction. In order to understand the manifestation of such third-order nonlinearities it is valuable to start with a brief description of the dielectric function and the complex index of refraction.[35] In the proceeding section these concepts are further expanded by description of wave propagation through a nonlinear material with a third-order susceptibility which are subsequently used to describe two important physical phenomena; two-photon absorption and the Kerr effect.

The permittivity or dielectric function measures the ability of an applied electric field to polarize the medium. Through classical mechanics the Lorentz oscillator model describes the permittivity by the following,

$$\varepsilon(\omega) = \varepsilon_b \left(1 + \frac{f}{\omega_0^2 - \omega^2 - i\omega\gamma}\right) \tag{2.32}$$

where $\omega$ is the angular frequency, $\varepsilon_b$ is the background dielectric constant, $\omega_0$ is the resonant frequency, $\gamma$ is the damping constant, and $f$ is the oscillator strength. This complex dielectric function can be separated into real and imaginary parts as follows,

$$\varepsilon(\omega) = \varepsilon_b \left(1 + \frac{f(\omega_0^2 - \omega^2)}{(\omega_0^2 - \omega^2)^2 + \omega^2\gamma^2} + i\frac{\omega\gamma f}{(\omega_0^2 - \omega^2)^2 + \omega^2\gamma^2}\right) \tag{2.33}$$

or

$$\varepsilon(\omega) = \varepsilon_1(\omega) + i\varepsilon_2(\omega)$$

Plotted in Figure 2.4 are the real, $\varepsilon_1(\omega)$ and imaginary, $\varepsilon_2(\omega)$ components of the dielectric function for two different damping constants, $\gamma = [0, 0.2(\omega_L - \omega_0)]$. The real component corresponds to the extent a material is polarized when an electric field is applied due to creation of electric dipoles in the material. The imaginary component is proportional

to the absorption coefficient. When the damping constant approaches zero, $\gamma \to 0$ there exists a discontinuity and delta function around resonance for $\varepsilon_1(\omega_0)$ and $\varepsilon_2(\omega_0)$ respectively. Therefore, as the frequency approaches resonance from the right $\omega \to \omega_0$ the material is easily polarized and the permittivity increases dramatically. The delta function signifies that absorption losses only occur at a single frequency, $\omega_0$. Additionally, as the damping constant is increased the discontinuity ceases and a connection of the branches resumes for $\varepsilon_1(\omega)$, while $\varepsilon_2(\omega)$ broadens to a Lorentzian line shape.

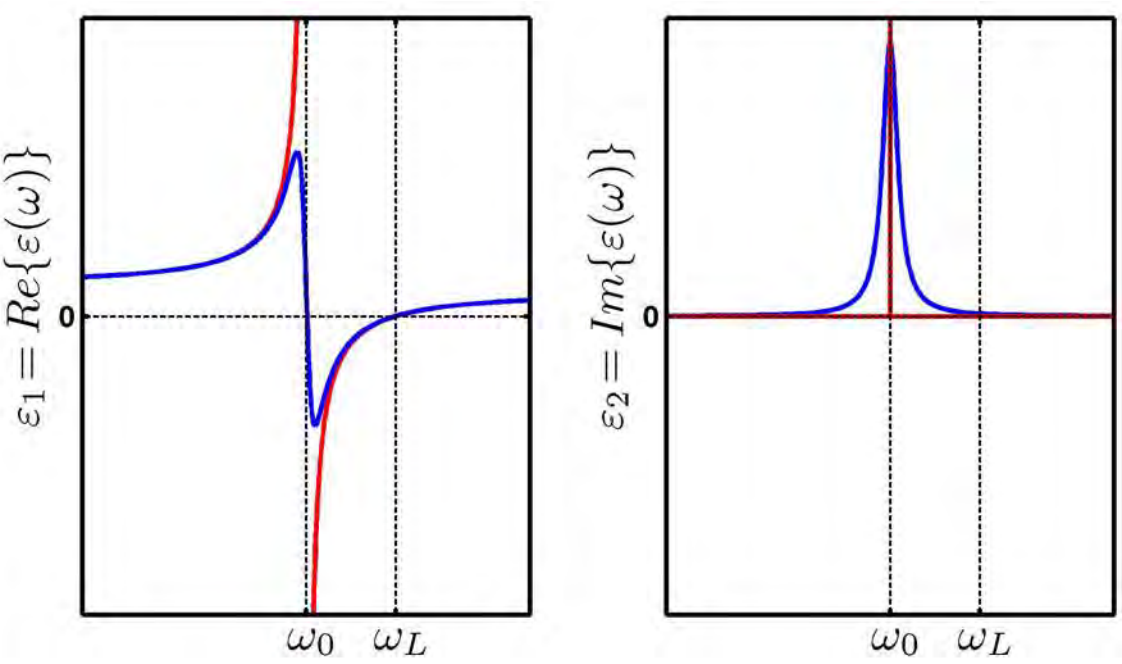


**Figure 2.4**: The real, $\varepsilon_1(\omega)$ and imaginary, $\varepsilon_2(\omega)$ components of the dielectric function for two different damping constants, $\gamma = 0$ (red) and $\gamma = 0.2(\omega_L - \omega_0)$ (blue) (Eq. 2.33). The longitudinal frequency $\omega_L$ corresponds to the frequency at which $\varepsilon(\omega) = 0$.

The complex index of refraction, $\tilde{n}(\omega)$ is related to the dielectric function by the following,

$$\tilde{n}(\omega) = \varepsilon^{1/2}(\omega) = n(\omega) + i\kappa(\omega)$$

where

$$n(\omega) = \left(\frac{1}{2}\left\{\varepsilon_1(\omega) + [\varepsilon_1^2(\omega) + \varepsilon_2^2(\omega)]^{1/2}\right\}\right)^{1/2} \tag{2.34}$$

$$\kappa(\omega) = \left(\frac{1}{2}\left\{-\varepsilon_1(\omega) + [\varepsilon_1^2(\omega) + \varepsilon_2^2(\omega)]^{1/2}\right\}\right)^{1/2}$$

Here the real component, $n(\omega)$ generally referred to as the refractive index which corresponds to the speed of light through the material. The imaginary component, $\kappa(\omega)$ is also known as the absorption coefficient, which refers to the amount of absorption loss when an electric field propagates through a material.

Plotted in Figure 2.5 are the real, $n(\omega)$ and imaginary, $\kappa(\omega)$ components of the complex refractive index for two different damping constants, $\gamma = [0,0.2(\omega_L - \omega_0)]$. When the damping constant approaches zero, $\gamma \to 0$ there exists a portion of the spectrum $\omega_0 \leq \omega \leq \omega_L$ where $n(\omega) = 0$. Therefore, an electric field does not propagate within the material between these angular frequencies. On the contrary, as the damping constant is increased $n(\omega) \neq 0$ between $\omega_0 \leq \omega \leq \omega_L$ and some light can infiltrate the medium. However, $\kappa > n$ and the light is strongly absorbed.

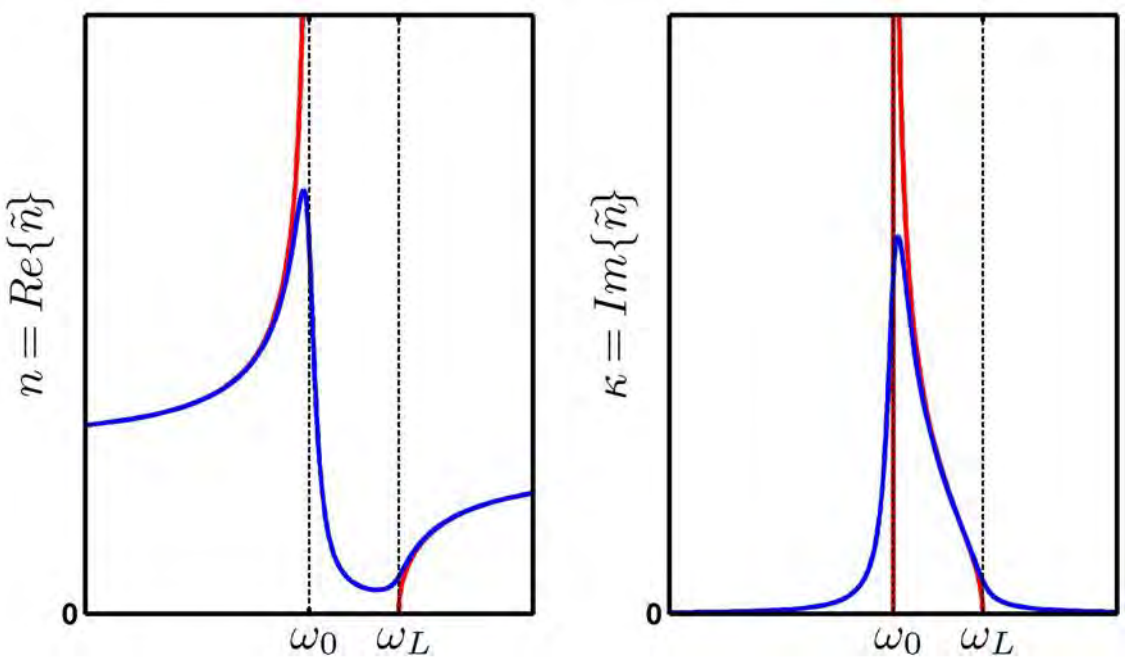


**Figure 2.5:** The real, $n(\omega)$ and imaginary, $\kappa(\omega)$ components of the index of refraction for two different damping constants, $\gamma = 0$ (red) and $\gamma = 0.2(\omega_L - \omega_0)$ (blue) (Eq. 2.34).

## 2.5. THIRD ORDER TERMS

Given that both the permittivity and complex refraction of index have been introduced, consider the affect of nonlinear polarization on the refractive index. With the formulations of the nonlinear interactions described above, the wave equation (Eq. 2.23) in conjunction with the slow varying amplitude approximation (Eq. 2.26) is solved for a material that is isotropic and only the third-order polarization term is considered. This approach is analogous to the method used to derive the equations for second-harmonic generation (Eq. 2.29), where only the second-order corrections were considered. The change in amplitude as a function of propagation along the z-axis is given by the following,

$$\frac{dA}{dz} = \frac{i\omega}{4nc}\chi^{(3)}(\omega;\omega,-\omega,\omega)|A|^2 A \tag{2.35}$$

However, the third order susceptibility, $\chi^{(3)}$ present in Eq. 2.35 can be broken it to its real, $\chi_r^{(3)}$ and imaginary, $\chi_i^{(3)}$ components.

$$\frac{dA}{dz} = \frac{i\omega}{4nc}\left(\chi_r^{(3)} + i\chi_i^{(3)}\right)|A|^2 A \tag{2.36}$$

Assuming that the amplitude can be described by a complex envelope function that contains both amplitude, $|A(z)|$ and phase, $\phi$ components,

$$A(z) = |A(z)|e^{i\phi(z)} \tag{2.37}$$

Insertion of Eq. 2.37 into Eq. 2.36 and applying the chain rule results in the following.

$$\frac{d|A|}{dz} + i|A|\frac{d\phi}{dz} = \frac{\omega}{4nc}\left(i\chi_r^{(3)}|A|^3 - \chi_i^{(3)}|A|^3\right) \tag{2.39}$$

Separation of Eq. 2.39 into its real and imaginary portions results in a pair of equations in which the change in amplitude and phase along the z-axis are proportional to the imaginary and real components of the third-order susceptibility respectively.

$$\frac{d|A|}{dz} = -\frac{\omega}{4nc}\chi_i^{(3)}|A|^3 \tag{2.40}$$

$$\frac{d\phi}{dz} = \frac{\omega}{4nc}\chi_r^{(3)}|A|^2 \tag{2.41}$$

In the proceeding subsections it will be shown that the real and imaginary components of the third-order nonlinear susceptibility are related to the two-photon absorption coefficient, $\beta$ and nonlinear refraction index, $n_2$ respectively. Both variables are essential in describing the origin of the transient absorption pump-probe signal discussed in chapter 6.

### 2.5.1. Nonlinear Absorption (Two-Photon)

The following is a brief derivation relating the imaginary component of the third-order nonlinear susceptibility to the two-photon absorption coefficient. Starting with Eq. 2.40, subsequent multiplication of $|A|$ to both sides of results in the following,

$$|A|\frac{d|A|}{dz} = \frac{-\omega}{4nc}\chi_i^{(3)}|A|^4 = \frac{1}{2}\frac{d|A|^2}{dz} \tag{2.42}$$

After simple reorganization, Eq. 2.42 may be rewritten as,

$$\frac{d|A|^2}{dz} = \frac{-\omega}{2nc}\chi_i^{(3)}|A|^4 \tag{2.43}$$

Using the definition for intensity, $I$,

$$|A|^2 = \frac{2}{n\varepsilon_0 c}I \tag{2.44}$$

Next substitution of Eq. 2.44 into Eq. 2.43 results in the following,

$$\frac{dI}{dz} = \frac{-\omega}{n^2c^2\varepsilon_0}\chi_i^{(3)}I^2 \tag{2.45}$$

Finally, the imaginary component of the third-order nonlinear susceptibility is encompassed within $\beta$, the two-photon absorption coefficient.

$$\frac{dI}{dz} = -\beta I^2 \tag{2.46}$$

The coefficient is related to the probability of simultaneously absorbing two-photons. The fact that the two-photon coefficient is related to the square of the intensity provides nonlinear microscopy its advantageous capabilities described herein. To increase the probability of two photons absorbing simultaneously a pulsed femtosecond laser is traditionally utilized in conjunction with a microscope objective. The net result is a large concentration of photons in a very small area (large $I$).

### 2.5.2. Nonlinear Refraction (Kerr Effect)

The following is a brief derivation relating the real component of the third-order nonlinear susceptibility to the intensity dependent index of refraction (i.e. Kerr effect). The solution of Eq. 2.41 results in a linear relationship between the phase and propagation along the z-axis.

$$\phi = \frac{\omega}{4nc}\chi_r^{(3)}|A|^2 z \tag{2.47}$$

Subsequently, Eq. 2.47 may be substituted into the real part of the fundamental wave. The real part of the electric field is then described by the following,

$$Re\{E(z,t)\} = A(z)cos\left[\left(n_0 + \frac{1}{4n_0}\chi_r^{(3)}|A|^2\right)k_0 z - \omega t\right] \tag{2.48}$$

noting that,

$$k = \frac{n_0\omega}{c} = n_0 k_0$$

The total index of refraction is described by two terms that reside within parenthesis in Eq. 2.48,

$$n = n_0 + \frac{1}{4n_0}\chi_r^{(3)}|A|^2 \tag{2.49}$$

Next, the real component of the third-order susceptibility maybe written in terms of $n_2$, the nonlinear index of refraction. With an additional substitution an intensity dependent index of refraction is found,

$$n(I) = n_0 + n_2 I \tag{2.50}$$

where

$$n_2 = \frac{1}{2n_0^2\varepsilon_0 c}\chi_r^{(3)}$$

and

$$I = \frac{cn_0\varepsilon_0}{2}|A|^2$$

Consequently, the real component of the third-order nonlinearity adds an intensity dependent index of refraction term. The sign of the nonlinear index coefficient leads to physical phenomena of self-defocusing $(n_2 < 0)$and self-focusing $(n_2 > 0)$. Eq. 2.50 will be revisited in chapter 6 where the transient absorption pump-probe signal contains a Kerr lensing component originating from a spatial variation in the index of refraction due to the localized charge carrier distribution produced by the excitation.

# CHAPTER 3. EXPERIMENTAL SETUP

## 3.1. OPTICAL TABLE

The experimental setup consists of a thoughtful arrangement of optical elements and devices. A schematic diagram of the nonlinear microscope used in the proceeding experiments is displayed in Figure 3.1. The coherent radiation is derived from a commercially available diode-pumped continuous wave visible laser system (Spectra-Physics: Millennia Pro-15sJ). The Millennia uses the output from a diode laser to pump $Nd^{3+}$ ions doped in a yttrium vanadate crystalline matrix ($Nd:YVO_4$). The resulting 1064 nm laser emission is frequency doubled in a temperature tuned lithium triborate (LBO; $LiB_3O_5$) crystal which is capable of outputting 15 W of continuous wave laser radiation at 532 nm. The ultrafast pulses are derived from a commercially available mode-locked Ti:sapphire laser system (Spectra-Physics: Tsunami). The output of the Millennia pumps $Ti^{3+}$ ions doped within a sapphire crystalline matrix ($Ti:Al_2O_3$). The resulting stimulated emission generates tunable (700-1000 nm) laser pulses that are approximately 80 fs in duration at a repetition rate of 80.4 MHz. Typically, the Tsunami outputs greater than 3 W at 810nm. The majority of the Ti:sapphire output is sent to a commercially available optical parametric oscillator (OPO) (Spectra-Physics: Opal). Parametric down conversion is achieved in a LBO crystal. The Opal generates tunable (1.1-1.6 μm) pulses that are less than 120 fs in duration. Typically, the Opal outputs approximately 600 mW at 1640 nm when pumped at 810 nm.

The excitation pulse at 730 nm is generated from the frequency doubled output of the OPO. A focusing lens (L3) is placed before the nonlinear crystal (O3) in order to increase the intensity and conversion efficiency. A second lens (L4) is used to re-collimate the frequency doubled light. Conversion efficiencies of 20% are regularly obtained. Imaging is achieved by raster scanning the sample across the focal point of the microscope objective

(O6) with a piezoelectric nano-positioning stage (M5). The spatial resolution of the two-photon microscope is approximately 350 nm.

Pump-probe microscopy is accomplished by picking off a small portion of the Ti:sapphire output with an ultrafast beam sampler (O1) for use as the probe pulse. Two acousto-optic modulator pulse pickers (A2) reduce the repetition rate of the pump and probe beams to 1.6 MHz to ensure complete relaxation before the next pump-probe pair arrives. In order for the pulse pickers to achieve good efficiency and extinction ratio a rise time of < 7ns must be ensured. This is achieved by focusing the pump and probe beams with corresponding lenses (L1 & L5). Subsequently, a second set of lenses (L2 & L6) are used to re-collimate and expand the beams such that their diameters overfill the microscope objective. Next, an optical delay line consisting of a motorized linear stage (M1) and hollow retro reflector (O2) is inserted into the path of the probe beam to control the time delay between excitation and probe pulses. Both pump and probe are sent collinear to a microscope objective (O6) by transmission and reflection from a second ultrafast beam sampler (O1) respectively. The beams are focused to a diffraction limited spot by a microscope objective whose focal plan is controlled with a nano-piezoelectric actuator (M4). The probe beam is collected by a condenser lens (O7) and focused onto the entrance slit of a monochromator (D1) and detected by a photomultiplier tube (D2) and current pre-amplifier (D3). A long-pass filter (O8) placed before the monochromator rejects unwanted pump light. An optical chopper modulates the excitation beam at 4 kHz, and pump induced changes in the intensity of the probe pulse are monitored by a digital lock-in amplifier (D4). Analog data acquisition (D5) is handled in conjunction with MATLAB. The microscope can measure $\Delta I/I$ as low as $10^{-4}$. The pump and probe polarizations were parallel to each other

and oriented perpendicular to the long axis of the rod. A second acousto-optic modulator (A1) is placed in the path of the probe beam for ease of modulation of the probe beam for ease of lock-in detection for probe transmission images (i.e. no pump present). It should be noted that the optical chopper is left in continuous wave mode during pump-probe experiments.

In the time resolved fluorescence measurements, light emanating from the sample is recollected by the objective, transmitted through a dichroic beam-splitter (O5), and focused onto the entrance slit of a streak camera (D6). The instrument response of the streak camera is approximately (9-20 ps). This value is strongly affected by the source of the trigger (See section 3.1.3).

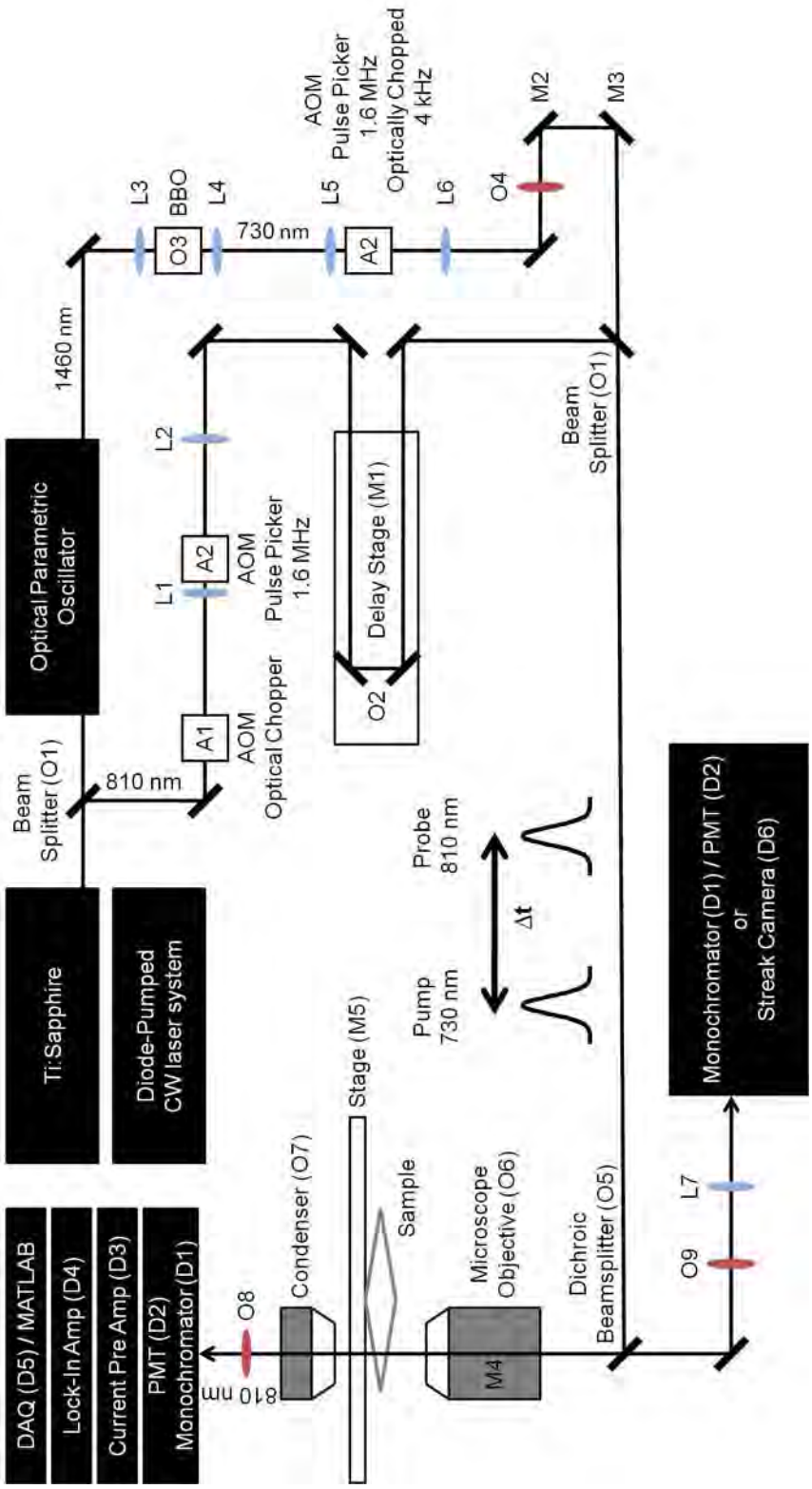


**Figure 3.1:** Schematic of optical table setup

## Acoustio-Optic Modulators

(A1) Gooch & Housego: 2308-2-.85-LTD; Acousto Optic Modulator

(A2) Gooch & Housego: 17389.93-FOA; Six Nanosecond Infrared AOM

## Detection

(D1) Spectral Products: CM110; Compact 1/8 Meter Monochromator

(D2) Hamamatsu: R928; Photomultiplier Tube

(D3) Stanford Research Systems: SR570; Low Noise Current Preamplifier

(D4) Stanford Research Systems: SR830; DSP Dual Phase Lock-In Amplifier

(D5) National Instruments: PCI-6221; Data Acquisition 16-Bit, 250 kS/s, 16 Analog Inputs

(D6) Hamamatsu: C10627; Streak Scope

## Lenses

(L1) Thorlabs: LA1131-B; N-BK7 Plano-Convex Lens, Ø1", f = 50.0 mm, ARC: 650-1050

(L2) Thorlabs: LA1433-B; N-BK7 Plano-Convex Lens, Ø1", f = 150.0 mm, ARC: 650-1050

(L3) Thorlabs: LA1131-C; N-BK7 Plano-Convex Lens, Ø1", f = 50.0 mm, ARC: 1050-1620

(L4) Thorlabs: LA1131-B; N-BK7 Plano-Convex Lens, Ø1", f = 50.0 mm, ARC: 650-1050

(L5) Thorlabs: LA1131-B; N-BK7 Plano-Convex Lens, Ø1", f = 50.0 mm, ARC: 650-1050

(L6) Thorlabs: LA1509-B; N-BK7 Plano-Convex Lens, Ø1", f = 100.0 mm, ARC: 650-1050

(L7) Thorlabs: LA1131-A; N-BK7 Plano-Convex Lens, Ø1", f = 50.0 mm, ARC: 350-700

## Motorized Stages & Actuators

(M1) Newport: ILS250CCHA; High Performance Mid-Range Travel Linear Stage

(M2) Newport: CMA-25CCCL; Compact Motorized Actuator, 25 mm Travel, Closed-loop DC Servo (x2)

(M3) Newport: TRA25CC; Miniature Motorized Actuator, 25 mm Travel, DC Servo Motor (x2)

(M4) Newport: PZA12; NanoPZ Ultra-High Resolution Actuator, 12.5mm Travel

(M5) Queensgate Instruments: NPS-XY-100A

**Optical Components**

(O1) Newport: 10B20-01NC.2; Ultrafast Beam Sampler

(O2) Edmund Optics: NT46-186; 25.4 Diameter Gold Hollow Retroreflector 30 Arc Sec

(O3) Castech: BBO, $\theta=32^{o}$, $\Phi=0^{o}$, 5 x 5 x 2 $mm^3$, S1,S2:P-400nm

(O4) Semrock: FF01-775/SP-25; 775 nm blocking edge BrightLine® short-pass filter

(O5) Semrock: FF670-SDi07-25x36; 670 nm edge BrightLine® multiphoton short-pass dichroic beamsplitter

(O6) Olympus: Microscope Objective, MSPlan 50x, NA 0.8

(O7) Olympus: Condenser, 1.25 (taken from another microscope)

(O8) Semrock: LP02-785RS-25; 785 nm RazorEdge® ultrasteep long-pass edge filter

(O9) Semrock: FF01-680/SP-25; 680 nm blocking edge BrightLine® multiphoton short-pass emission filter

### 3.1.1. Acousto-Optic Modulators

The repetition rate of the Ti:sapphire is 80.4 MHz or approximately 12.4 ns between pulses. However, excited charge carriers trapped in defect sites in ZnO can subsist for several nanoseconds. Consequently, to assure that all the excited charge carriers have ample time to relax the repetition rates of both excitation and probe pulses must be reduced. Further, the pump induced signals are monitored using lock-in detection to increase signal to noise through modulation of the excitation pulse. Experimentally, the reduction and modulation of pulses is accomplished through a combination of acousto-optic devices.

Acousto-optics describes the interaction of optical waves with acoustic waves in a medium. When a sound wave propagates through the medium a periodic strain within the medium

creates an index of refraction grating.[33] Accordingly, the resulting interaction of incident light and grating results in Bragg diffraction of the pulse. The Bragg diffraction angle, $\theta_B$ is given by the following,

$$\theta_B = \frac{\lambda f}{2v} \tag{3.1}$$

where $\lambda$ is the wavelength of light, $f$ is the frequency of the acoustic wave, $v$ is the acoustic velocity of the material. This diffraction is exploited in devices as a switch used to direct the path of the pulses. Displayed in Figure 3.2 is a schematic of an acoustic-optic modulator (AOM) used to reduce and modulate pulses in the proceeding pump-probe microscopy experiments. When a radio frequency (rf) is applied to the crystal the pulse is diffracted. Contrary, when no rf is applied no Bragg diffraction is observed and the pulse is unaffected.

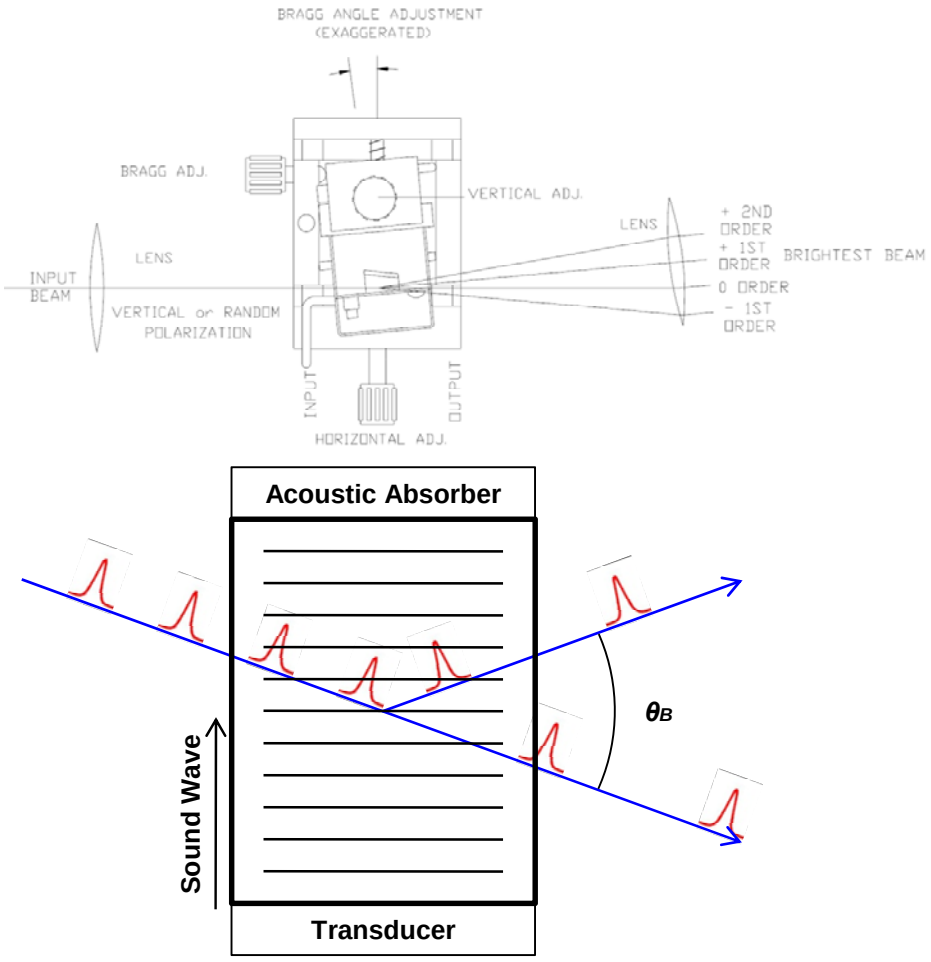


**Figure 3.2:** (Upper) Experimental setup of an AOM from Gooch and Housego (17389-.93-FOA). An input beam is focused into the crystal and when rf signal is applied the beam is diffracted. A second lens is used to collimate the diffracted beam. A three-axis manual positioning stage is used to adjust the Bragg angle as well as horizontal and vertical positioning within the crystal. (Lower) Diagram of pulse train entering the AOM, when rf is applied the pulse is diffracted at the Bragg angle, $\theta_B$. When no rf is applied the pulse in unaffected.

In practice, the optimum diffraction efficiency is related to the how fast the time-dependent index of refraction grating can be turned on and off. Consequently, it is essential to have a rise time that is substantially less than the time between pulses (12.4 ns). The

Gooch & Housego pulse picker (17389.92-FOA) provides optimum diffraction efficiency with a rise time of < 7 ns. However, this occurs only in a small spatial region inside the modulator. As a result, focusing the input beam inside the modulator is essential. The waist diameter inside the modulator, $d_0$ is given by the following equation,

$$d_0 = \frac{4 f_{lens} \lambda}{\pi d_1} \tag{3.2}$$

where $f_{lens}$ is the lens focal length, $\lambda$ is the wavelength of light, and $d_1$ is the input optical beam diameter. The modulator rise $t_r$ is then related to the waist diameter inside the modulator and the acoustic velocity of the material,

$$t_r = \frac{1.3 d_0}{2v} \tag{3.3}$$

The 17389.92-FOA modulator consists of a Tellurium Dioxide ($TeO_2$) crystal $v = 4260\ \mathrm{m/s}$. Optimum diffraction efficiency will be provided with a rise time of < 7 ns correlating to a waist diameter in the $TeO_2$ crystal of 35 μm. The focal length of the lens is then determined by $f/\#$ of the lens and the input beam diameter,

$$f/\#\, d_1 = f_{lens} \tag{3.4}$$

In order to change the repetition rate (pulse pick) both pump and probe pulses two separate AOM are implemented. Further, immense care must be taken in the timing of the rf drivers such that the pump and probe pulses are picked simultaneously. This involves synchronicity of both rf drivers to coincide with the pulses arriving in their corresponding AOM. While various timing schemes are available, the one used in the pump-probe experiments described herein is depicted in Figure 3.3.

Foremost, the probe AOM must be encountered before the delay stage for static timing between pump and probe rf drivers. The electronics module (Spectra-Physics: 3995)

associated with the Ti:Sapphire laser contains a sync output allowing for synchronized timing to other electronic devices. This sync output waveform depends on the operating wavelength, power and photodiode response within the Ti:sapphire. The sync out in conjunction with a level shifter allows coincident timing of the probe rf driver (Gooch & Housego: 64381.9-SYN-9.5-1) with the output of the Ti:sapphire.

In order for the picked pump and probe pulses to coincide, consider the following. Experimentally the pump and probe pulses are derived from the same source and physically the probe pulse arrives much earlier than the pump pulse to their corresponding AOM. Consequently, a delay must be placed in between the sync out of the probe rf driver and analog modulation input of the pump rf driver (Gooch & Housego: R31389.5-5AS). Currently, this is achieved with a digital delay generator (SRS: 645DG). The maximum external trigger rate of this device is $1/(100\text{ns} + \text{delay})$. Unfortunately, the delay needed for synchronicity is approximately 400 ns in the current experimental setup, corresponding to a maximum trigger rate of 2 MHz As a result, the fastest laser repetition rate that allows dual pulse picking is 1.61 MHz (80.4 MHz/50). If a different electronic or physical delay were used such that a faster trigger rate could be obtained, pulse picking at higher repetition rates could be achieved. Finally, slight adjustments of the three-axis manual positioning stage and digital delay generator produce synchronous picked pump and probe pulses.

Modulation of the excitation pulse is derived from a digital timing computer card (NI: PCI-6601) controlled through MATLAB. These conventional TTL outputs at are sent to a four-channel high input impedance 50 Ω TTL line driver (PRL-444). The first output is sent to the lock-in amplifier (SRS: SR830) as a reference. The second is sent to the inhibit channel in the back of the digital delay generator such that when the TTL is high, the AB

output is inhibited. The resulting waveform sent to the pump rf driver is modulated at a frequency originating from digital timing computer card. The third and forth channels are optional and can be used as triggers for the rf drivers (Gooch & Housego: R2180-2DS) in conjunction with additional AOM (Gooch & Housego: 23080-2-.85-LTD) used for optical chopping. Currently, a single optical chopper is used to characterize the probe beam in the microscope with lock-in detection.

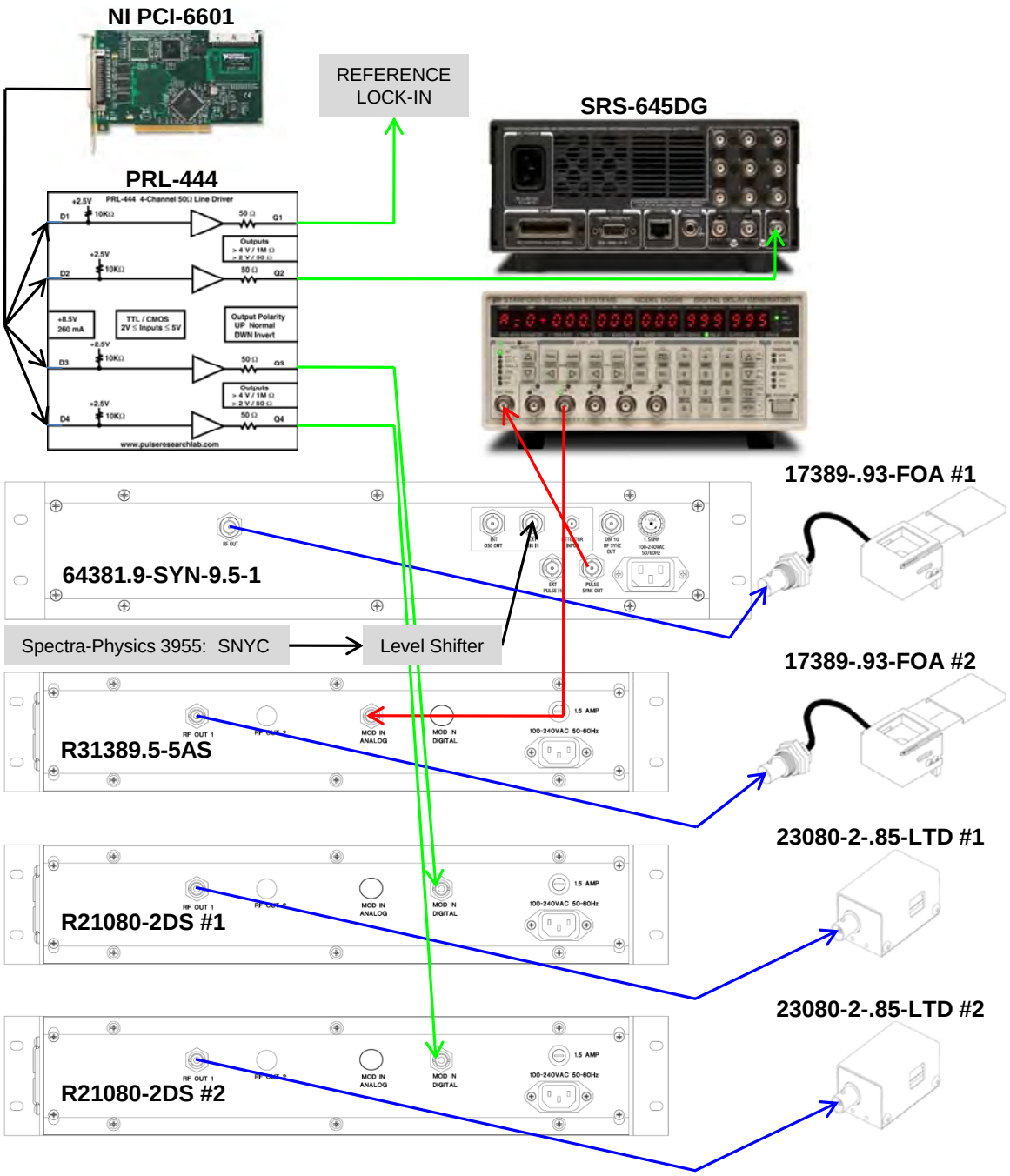


**Figure 3.3:** Experimental schematic used to reduce the repetition rate and modulate both pump and probe pulses. The pulse picking system consists of a probe rf driver (Gooch & Housego: 64381.9-SYN-9.5-1) and pump rf driver (Gooch & Housego: R31389.5-5AS) and corresponding AOM (Gooch & Housego: 17389-.93-FOA). The probe rf driver is synchronized with the Ti:sapphire laser through the electronics module (Spectra-Physics: 3995) in series with a level shifter. The pump and probe pulses are synchronized with the

insertion of delay from a digital delay generator (SRS-645DG). Modulation of the pump beam originates from a digital timing card (NI: PCI-6601) in series with a four channel high input impedance 50 Ω TTL line driver (PRL-444). One channel is used as a reference for the lock-in detection. The second channel inhibits the AB output of the digital delay generator at the frequency derived from digital timing computer card. The optical chopping system consists of two rf drivers (Gooch & Housego: R21080-2DS) and corresponding AOM (Gooch & Housego: 23080-2-.85-LTD) controlled by the third and fourth channels of the line driver.

### 3.1.2. Lock-In Detection

Lock-in amplification extracts a signal with a known carrier wave from an extremely noisy environment.[36,37] It uses a phase sensitive detector (PSD) which selects a component of the signal at a specific phase-locked-loop (PLL) reference frequency and phase. Signal extraction can be simplified as a two step process. First, the PSD multiplies the PLL reference frequency by an amplified input signal, after which the multiplied signal is sent through a low-pass filter. Lock-in detection heavily attenuates any signal that does not match the reference frequency. Experimentally, when the reference is synced to the optically chopped excitation pulse, detection of signal (SHG, emission, pump-probe) occurs only at the chopped frequency while all other frequencies are attenuated achieving a large signal to noise ratio. For example consider two waveforms, $\psi_1$ and $\psi_2$,

$$\begin{aligned} \psi_1 &= A_1 cos(\omega_1 t + \phi_1) \\ \psi_2 &= A_2 cos(\omega_2 t + \phi_2) \end{aligned} \tag{3.5}$$

where, $A_i$, $\omega_i$ and $\phi_i$ are the amplitude, frequency and phase components of the $i^{th}$ wave respectively. Since the PSD multiplies the PLL reference frequency by the signal, consider the multiplication of $\psi_1$ and $\psi_2$ taking into account the product to sum identity,

$$\psi_1\psi_2$$

$$= \frac{cos[(\omega_1 + \omega_2)t + (\phi_1 + \phi_2)] + cos[(\omega_1 - \omega_2)t + (\phi_1 - \phi_2)]}{2} \quad (3.6)$$

Notice that the multiplication of the waveforms contains components at the sum and difference frequencies. When the two waveforms have the same frequency and phase the difference component produces DC with amplitude equal to $V = A_1A_2/2$ (Figure 3.4). This situation is analogous to the experimental setup where the detection and the optically chopped reference frequency are the same. However, when the two waveforms have the same frequency but a phase shift of π/2 the difference component produces DC with amplitude of zero (Figure 3.5). Consequently, the magnitude of the output signal is related to the phase relationship between the input signal and PLL reference where the maximum amplitude occurs when the input and PLL frequencies are phase-matched.

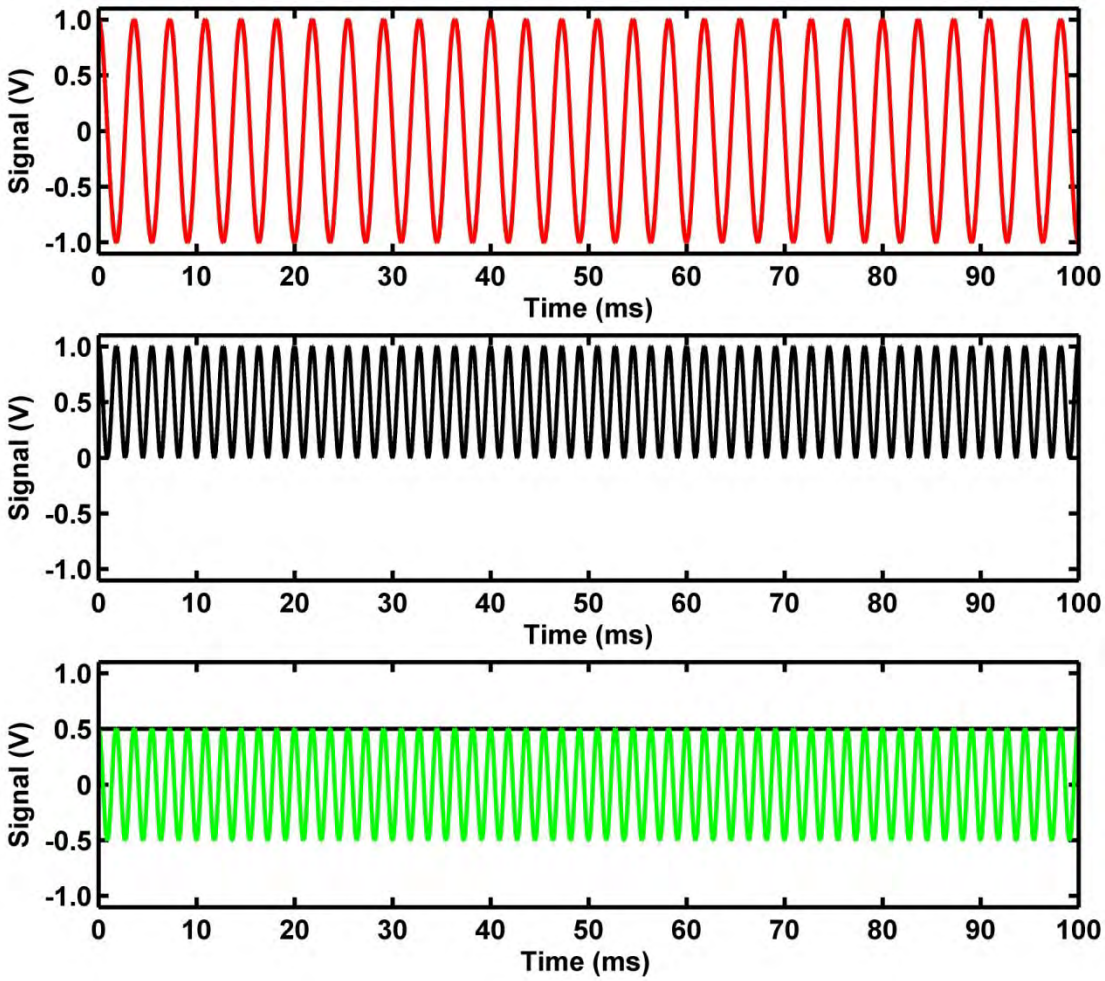


**Figure 3.4**: (Upper) plot of $\psi_1$ (red), $\omega_1 = \omega_2 = 275$ Hz, $\phi_1 = \phi_2 = 0$. (Middle) Multiplication of waveforms $\psi_1$ and $\psi_2$. (Lower) Difference frequency (black) and sum frequency (green) components of the multiplication of $\psi_1$ and $\psi_2$.

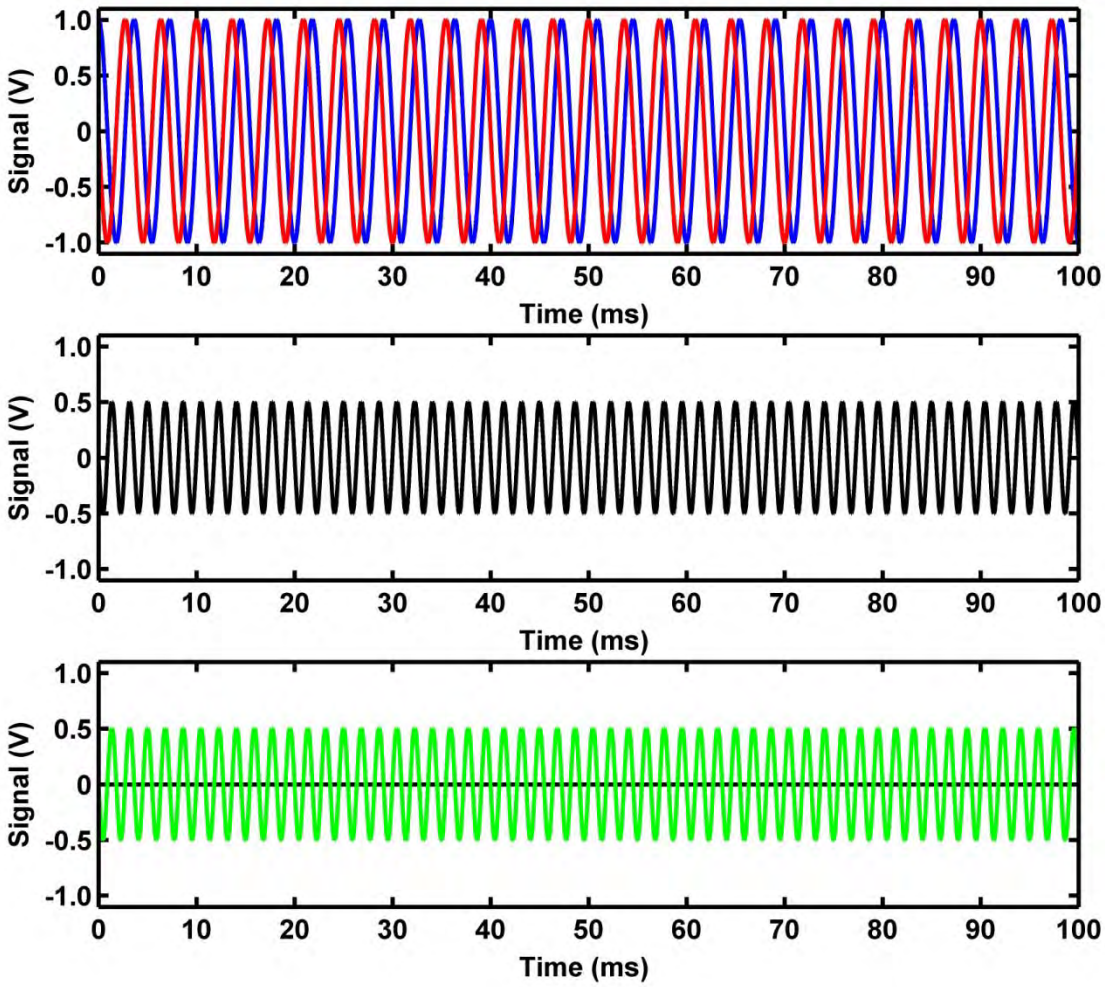


**Figure 3.5**: (Upper) plot of $\psi_1$ (blue); $\omega_1 = 275$ Hz, $\phi_1 = 0$ and $\psi_2$ (red); $\psi_2 = 275$ Hz, $\phi_2 = \pi/2$. (Middle) Multiplication of waveforms $\psi_1$ and $\psi_2$. (Lower) Difference frequency (black) and sum frequency (green) components of the multiplication of $\psi_1$ and $\psi_2$.

After multiplication of the waveforms the signal is sent through a low-pass filter. The output voltage, $V_{out}$ is given by the following,

$$V_{out} = \frac{V_{in}}{\sqrt{1 + (\tau_c \omega)^2}} \tag{3.7}$$

where $\tau_c$, is the time constant. Notice that at the difference frequency $\omega = \omega_1 - \omega_2$ there is no attenuation. While at the sum frequency $\omega = \omega_1 + \omega_2$ there is large attenuation. Further,

the greater the time constant the larger the attenuation. The time constant is related to the bandwidth of the filter by the following,

$$\tau_c = \frac{1}{2\pi f_{-3dB}} \tag{3.8}$$

where $f_{-3dB}$ is the -3 dB frequency of the filter. For example, a $\tau_c = 1$ s has a $f_{-3dB} = 0.16$ Hz where the SR830 the signal is rolled off at 6 dB/oct beyond $f_{-3dB}$. The SR830 has 4 filter stages with up to 24 dB/oct roll-off. While greater roll-off decreases noise the wait time for the output signal to settle to its final value is increased (Table 3.1). Displayed in Figure 3.6 is a plot of two waveforms with the same frequencies and phases after passing through a low-pass filter for a series of different time constants. As the time constant is increased the size of the noise on top of the DC signal is reduced.

| **Slope (dB/oct)** | **Wait time ($\times \tau_c$)** |
|---|---|
| 6 | 5 |
| 12 | 7 |
| 18 | 9 |
| 24 | 10 |

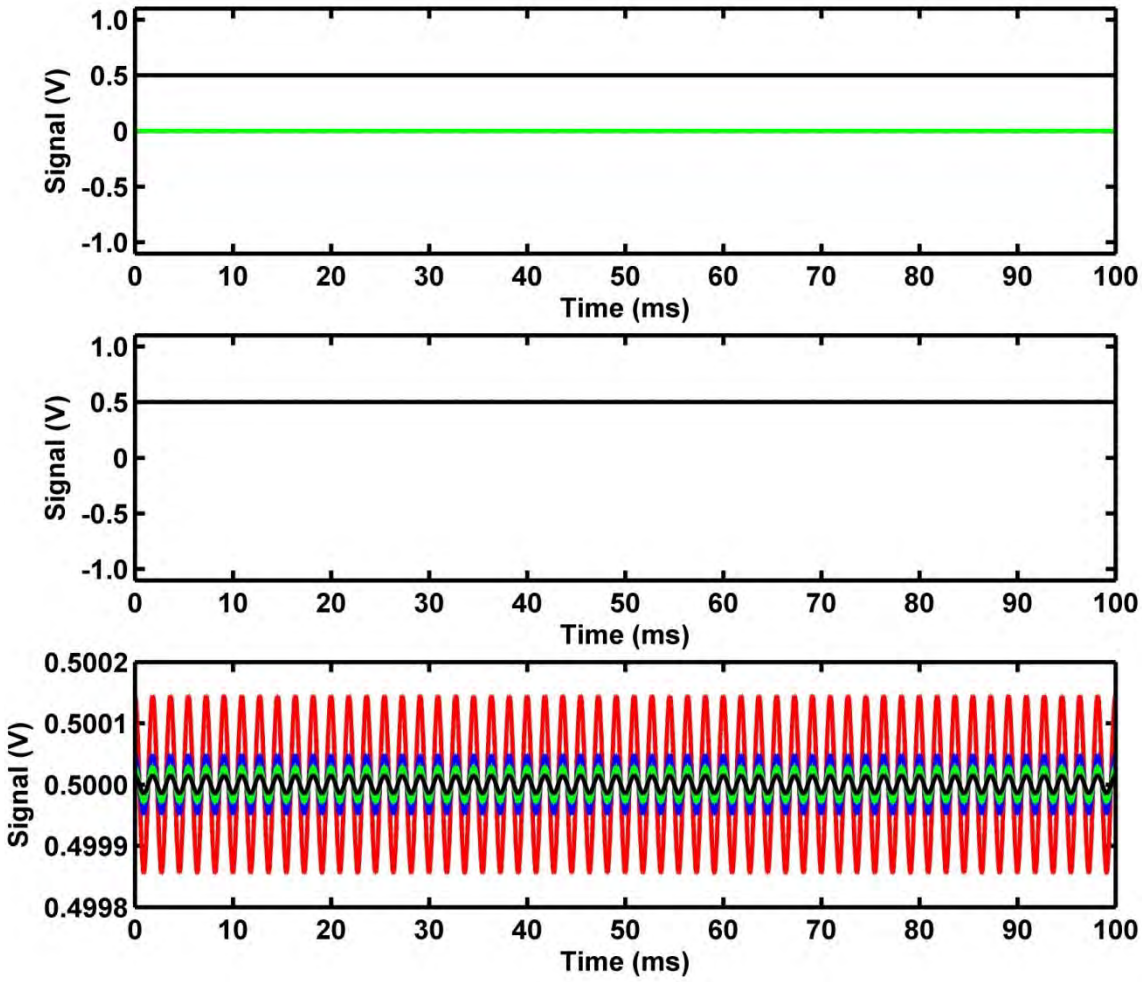


**Figure 3.6**: (Upper) plot of sum (green) and difference (black) components for the multiplication of waveform multiplication of waveforms $\psi_1$ and $\psi_2$; $\omega_1 = \omega_2 = 275$ Hz, $\phi_1 = \phi_2 = 0$ after low-pass filter. (Middle) Multiplication of waveforms $\psi_1$ and $\psi_2$. (Lower) blown-up scale of middle with different time constants, $\tau_c = 1$ s (red), 3 s (blue), 5 s (green), 10 s (black).

### 3.1.3. Streak Camera

A streak camera has been used to temporally and spectrally resolve emission profiles in a single measurement setup. Displayed in Fig.3.7 is a schematic diagram displaying the operation of the streak camera (Hamamatsu: Streak Scope C10627). Light emission collected from the microscope is directed toward the entrance slit (micrometer adjustable:

10μm to 3mm) of a 150mm focal length monochromator (Princeton Instruments: SP2150i). The interchangeable dual grating turret contains a 300 and 150gv/mm both blazed at 500nm gratings. Afterwards, the horizontally dispersed light strikes a photocathode (4.5mm w x 0.07mm h) which converts incident photons into electrons. These electrons are accelerated through a series of strategically placed electrodes. Next, the electrons are vertically dispersed through a sweeping voltage applied between top and bottom electrodes. Modulation of the voltage between the plates gives rise to a time-varying deflection of the electrons. The sweep electrodes can be operated up to 20MHz (1ns range). These electrons strike a multichannel plate amplifying the signal and then are directed to a phosphorous screen where they are converted back into photons. Finally, these photons are imaged onto a CCD camera (Hamamatsu: C9300-221 480pixels w x 640pixels h). The measured dispersion is 17.8 and 36.4nm/mm for the 300 and 150gv/mm gratings respectively. As a result the maximum resolution is 0.12 and 0.26nm/pixel while the spectral windows are 80.0 and 163.8 nm for the 300 and 150 gv/mm gratings respectively.

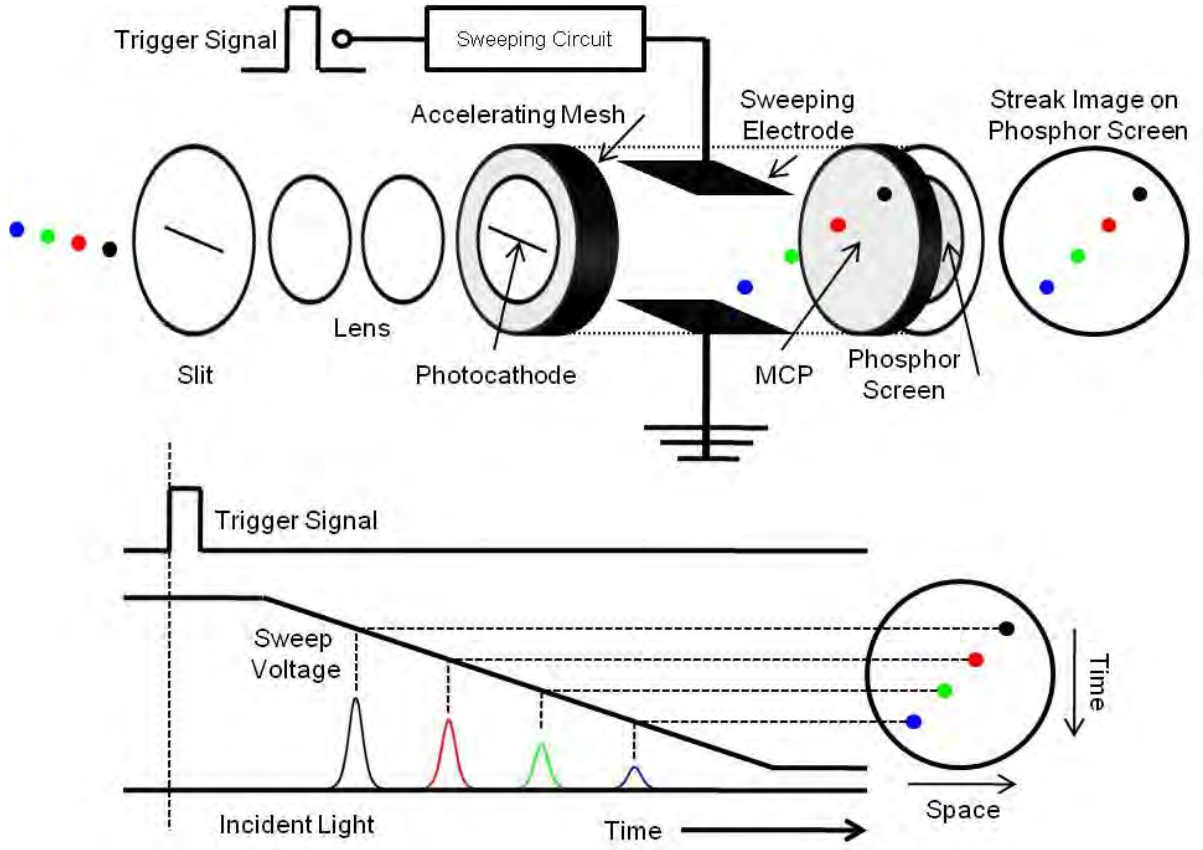


**Figure 3.7:** (Upper) Schematic diagram of streak camera. Incident light spatially dispersed after a monochromator enters the slit of the streak camera. A series of lens are used to focus the incoming light onto a photocathode. The expelled electrons are sent through the streak tube where a sweeping circuit triggers the sweeping electrode which applies a sweep voltage. The voltage dependent deflection smears the electrons out in time. Subsequent amplification with a multi channel plate (MCP) and conversion back to photon through collision on a phosphor plate a streak image is generated. (Lower) Trigger and sweep voltage diagram and sequential streak camera image on phosphor screen sent to CCD camera.

The precise timing of the sweep voltage is essential in production of a streak camera image. The sweep voltage must be applied when the emission converted electrons are between the sweeping electrodes. Displayed in Figure 3.8 is a schematic diagram how the optical source is synchronized with the streak camera. On the back of the streak scope is a

trigger signal input connector (TRIG.IN). Any signal less than 5V/50Ω amplitude will trigger the streak scope. First, a portion of the excitation laser is picked off and directed to a pin diode head (Hamamatsu: C1808-03) which puts out a constant 1.5V/50Ω peak to peak signal. Since experimentally the pin diode (origin of the streakscope trigger) arrives before the sweep voltage, a delay must be inserted into the path. Currently, there are two timing setups, one for high repetition (80.4 MHz to 8.04 MHz) and one for low repetition (less than 4.02 MHz) excitations respectively.

In the case of high repetition the output of the pin diode is delayed with physical delay units (i.e. Hamamatsu: C1097-05, Ortec 425A). Finally, this output is directly inserted into the streak scope TRIG.IN. The streak camera at 1 ns range has approximately < 10 ps IRF. In the case of low repetition the addition of the streak trigger unit (Hamamatsu: C4547-02) is required. This permits an extremely low jitter trigger for the streak camera that is unachievable with either the sync out of the AOM driver or digital delay unit. When used in the external trigger mode an IRF of 20 ps is easily achieved.

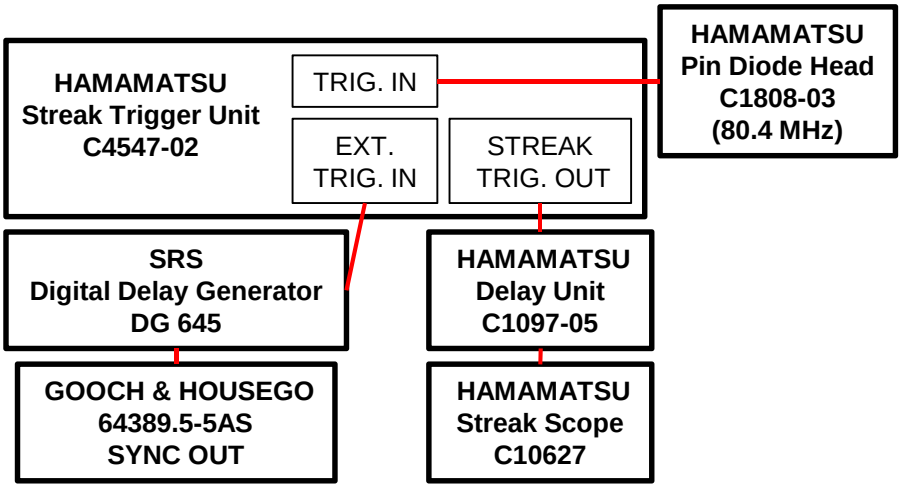


**Figure 3.8:** Diagram of timing electronics for of streak camera at a low repetition rate. The streak trigger unit generates a low jitter trigger that is synchronized with the excitation pulse.

### 3.2. TEMPORAL RESOLUTION

In order to measure any event in time you must use something faster. On femtosecond ($10^{-15}$) timescales options are limited. For that reason, when measuring an ultrafast pulse it is advantageous to use a similar pulse by means of a cross-correlation. Experimentally, this is achieved by taking two pulses delayed with respect to each other and measuring their instantaneous response in a nonlinear medium. Consequently, the intensity of the signal depends on how well the pulses are overlapped within the medium (i.e. the relative delay between pulses).[38] A schematic diagram for a cross-correlation used as a temporal benchmark in the pump-probe microscopy experiments is displayed in Figure 3.9.

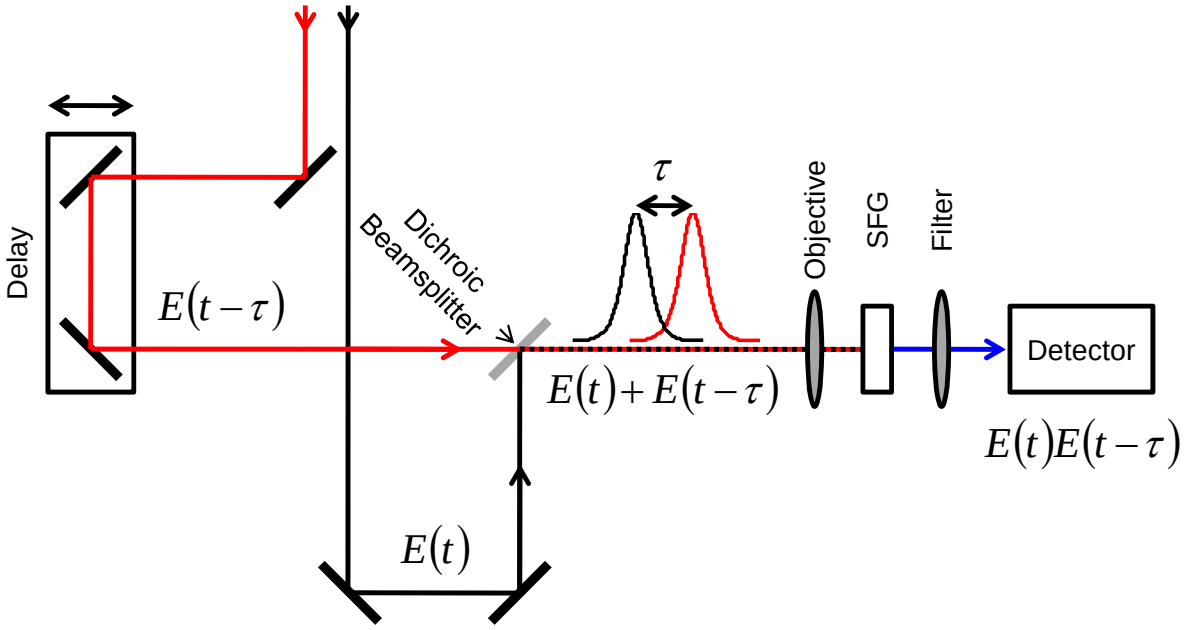


**Figure 3.9:** Experimental layout for pump-probe microscopy collinear cross-correlation using sum-frequency generation (SFG). A pulse from the Ti:sapphire (red) and a pulse from the OPO (black) are delayed with respect to each other by means of a translational stage placed in one of the pulses path. The pulses are sent collinear with the aid of dichroic beamsplitter. Subsequently, they are focused with a microscope objective into a nonlinear medium (lithium niobate powder: $LiNbO_3$) where light at the sum-frequency is generated

when the two pulses are overlapped in time. Next, a filter removes second-harmonic and fundamental frequencies. Finally, the SFG signal is detected by a photomultiplier tube.

Mathematically, the electric field signal cross-correlation from a second-order nonlinear process, $E_{sig}^{(2)}$ is given by the following,

$$E_{sig}^{(2)}(t,\tau) \propto E(t)E(t-\tau) \tag{3.9}$$

The time delay between pulses is defined by $\tau$. Accordingly, the intensity of the signal, $I_{sig}^{(2)}$ is proportional to the product of the intensities of the two individual pulses,

$$I_{sig}^{(2)}(t,\tau) \propto I(t)I(t-\tau) \tag{3.10}$$

For the purpose of experimental collection, measurements for an intensity cross-correlation are collected in a time integral form,

$$A^{(2)}(\tau) = \int_{-\infty}^{\infty} I(t)\, I(t-\tau)dt \tag{3.11}$$

When the two optical arms are of the same waveform, the cross-correlation is referred to as an autocorrelation. Displayed in Figure 3.10 are theoretical autocorrelations for a gaussian and hyperbolic secant squared pulse using Eq. 3.11. The full-width half max (FWHM) of the autocorrelation from a gaussian pulse is larger by a factor $\sqrt{2}$ relative to the FWHM of the pulse, while the autocorrelation from a hyperbolic secant squared pulse is approximately 1.54 larger.

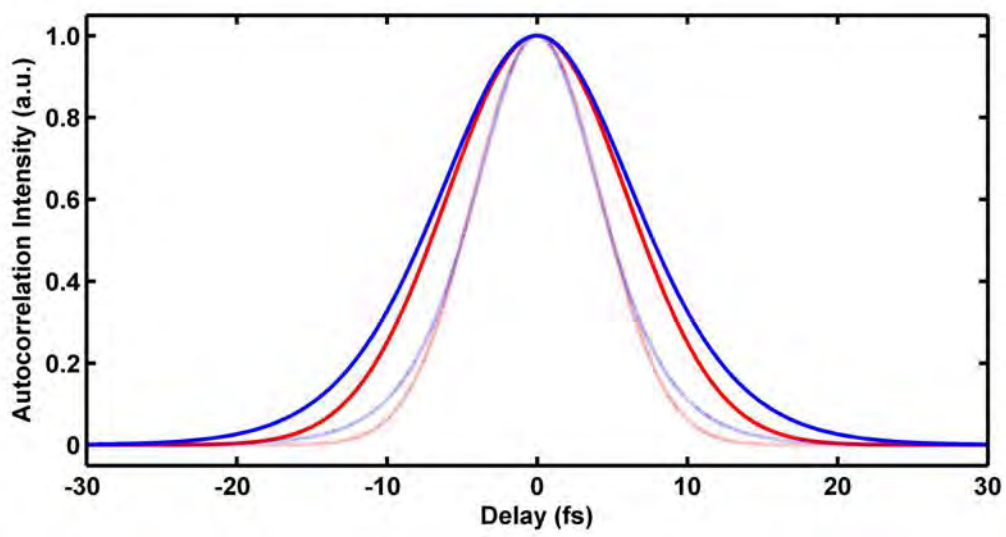


**Figure 3.10:** Autocorrelation from a gaussian pulse; $f(t) = e^{-(\tau_g)^2}$ where, $\tau_g = 2\sqrt{ln(2)}t/\tau_p^{FWHM}$, $\tau_p^{FWHM} = 10$ fs (dotted red). Autocorrelation intensity; $A_{gauss}^{(2)} = e^{-\left(\frac{\tau g}{\sqrt{2}}\right)^2}$ (solid red). Autocorrelation from a hyperbolic secant squared pulse; $f(t) = sech^2(\tau_s)$ where, $\tau_s = 2ln\left(1+\sqrt{2}\right)/\tau_p^{FWHM}$ (dotted blue). Autocorrelation intensity; $A_{sech^2}^{(2)} = \frac{3}{sinh(\tau_s)^2}(\tau_0 coth(\tau_s) - 1)$ (solid blue).

Further, when an autocorrelation is performed in a collinear fashion (Figure 3.11) interference patterns are observed. The fringe-resolved autocorrelation is due to the coherent combination of second-harmonic from the two different pulses along with that created by each individual pulse. The period of the oscillation is determined by the angular frequency of the waveform. The intensity of a fringe-resolved autocorrelation is given by the following.

$$A_{FRAC}(t,\tau) = \int_{-\infty}^{\infty} |E(t) + E(t-\tau)^2|^2 \, dt \qquad (3.12)$$

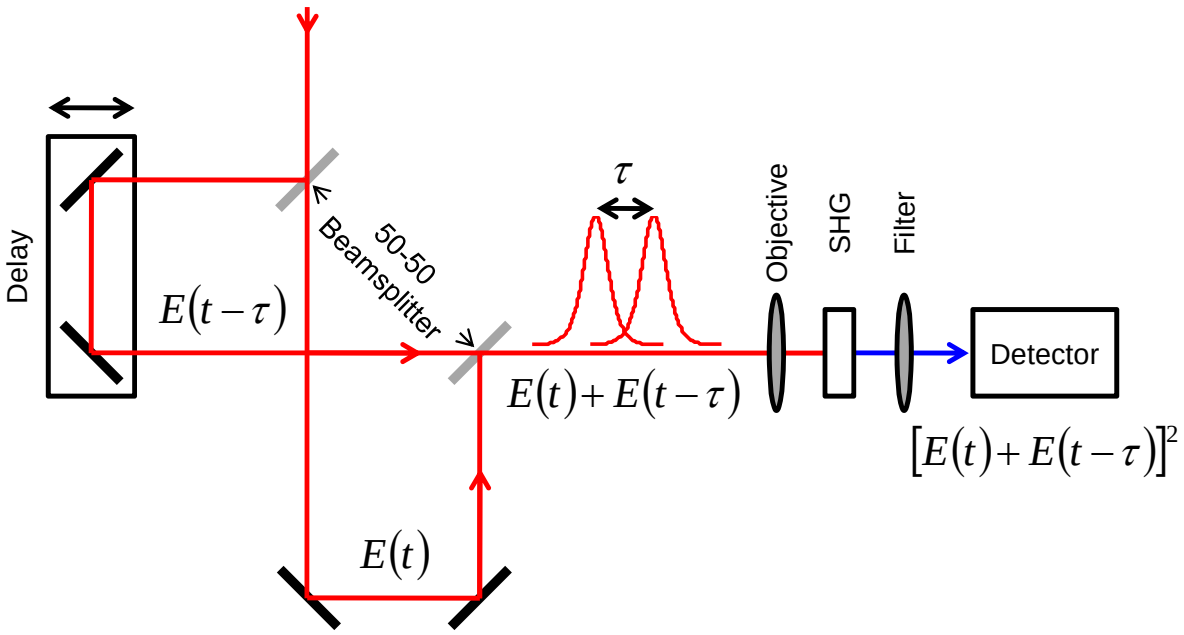


**Figure 3.11:** Experimental layout for a microscopy fringe-resolved interferometric autocorrelation. A pulse from the Ti:Sapphire (red) is split into two separate pulses by means of a 50-50 beamsplitter. One arm of the interferometer is delayed with respect to each other by means of a translational stage placed in one of the arms path. The pulses are sent collinear with the aid of an additional 50-50 beamsplitter. Subsequently, they are focused with a microscope objective into a nonlinear medium (lithium niobate powder: $LiNbO_3$) where light at the second-harmonic is generated when the two pulses are overlapped in time. Next, a filter removes the fundamental frequency. Finally, the SHG signal is detected by a photomultiplier tube.

Shown in Figure 3.12 are theoretical fringed-resolved autocorrelations from gaussian and hyperbolic secant squared pulses using Eq. 3.12.[39] The interferometric intensity displays a characteristic 8:1 ratio of maximum to background intensity.

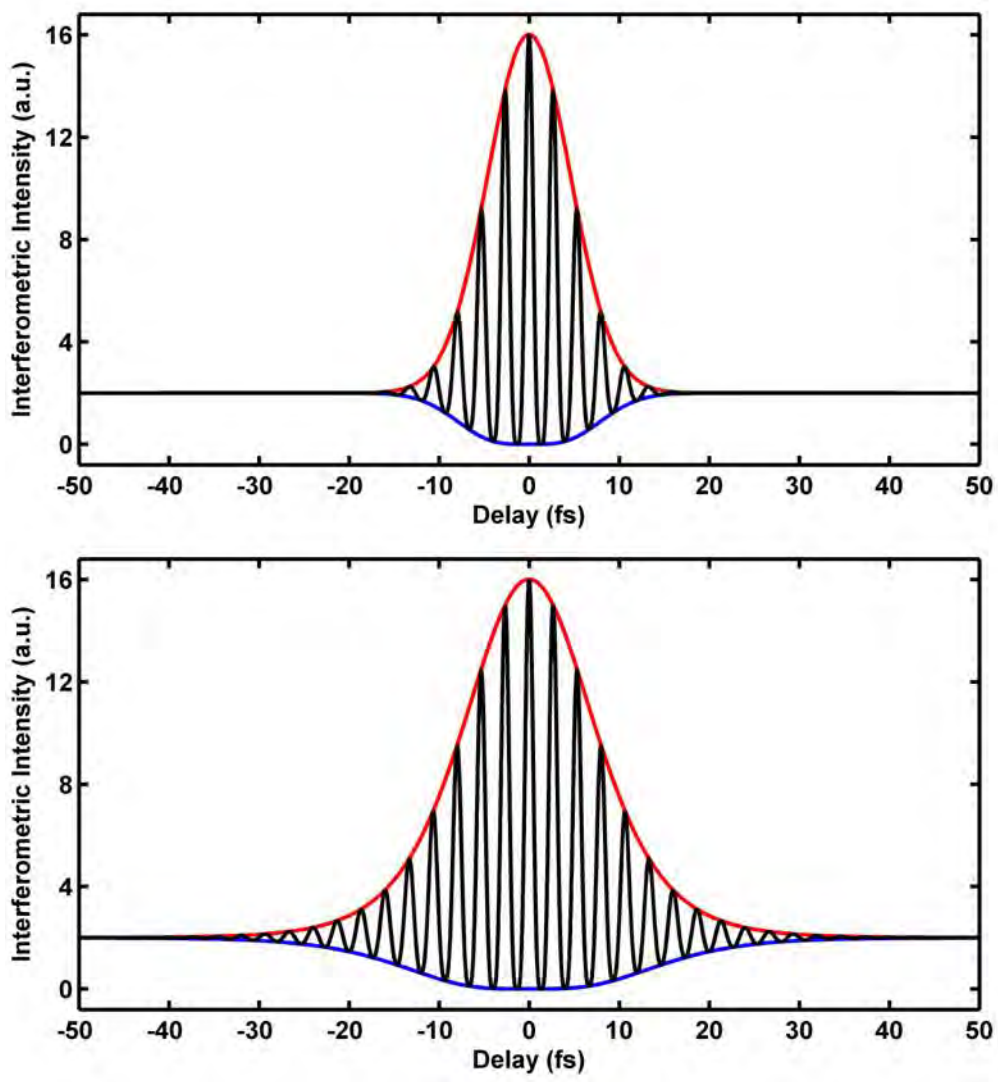


**Figure 3.12:** (Upper) Fringe-resolved autocorrelation from a gaussian pulse; $f(t) = e^{-(\tau_0)^2}$ where, $\tau_0 = \frac{t}{\tau_p}$, $\tau_p = \frac{10\text{ fs}}{2\sqrt{ln(2)}}$. Interferometric intensity; $A^{(2)}_{gauss}(\tau) = 1 + 2e^{-\tau_0^2} + 4e^{\frac{-3\tau_0^2}{4}}cos(\omega\tau) + e^{-\tau_0^2}cos(2\omega\tau)$. (Lower) Fringe resolved autocorrelation from a hyperbolic secant squared pulse; $f(t) = sech^2(\tau_0)$ where, $\tau_p = \frac{10\text{ fs}}{2ln(1+\sqrt{2})}$. Interferometric intensity; $A^{(2)}_{sech^2}(\tau) = 1 + \frac{6[\tau_0 cosh(\tau_0)]}{sinh^3(\tau_0)} + \frac{3[sinh(2\tau_0) - 2\tau_0]}{sinh^3(\tau_0)}cos(\omega\tau) + \frac{3[\tau_0 cosh(\tau_0) - sinh(\tau_0)]}{sinh^3(\tau_0)}cos(2\omega\tau)$. The interferometric intensity upper envelope; $\int |E(t) + E(t-\tau)|^4 dt$ (red) and lower envelope; $\int |E(t) - E(t-\tau)|^4 dt$ (blue).

Currently, the pump-probe microscopy cross-correlation is approximately 500 fs (Figure. 3.13). This is measured from the overlap of the pump at 730 nm (second-harmonic output of OPO) and the probe at 810 nm (output of Ti:sapphire) through a microscope objective (Olympus MSPlan 50x, NA 0.8). This cross-correlation may be improved with insertion of a prism pair to pre-compensate for the dispersion experienced in the objective. The fringe-resolved autocorrelation from the output of the Ti:sapphire has also been measured after passage through the objective (Figure 3.14). It should be noted that simple cross-correlations and fringe-resolved autocorrelations do not yield unique pulse intensities. Generally, assumptions are initially made about the pulse shape. However, it has been found that ultrashort pulses don't have simple intensity profiles. Consequently, pulse lengths determined from simple cross-correlations should be taken with caution.

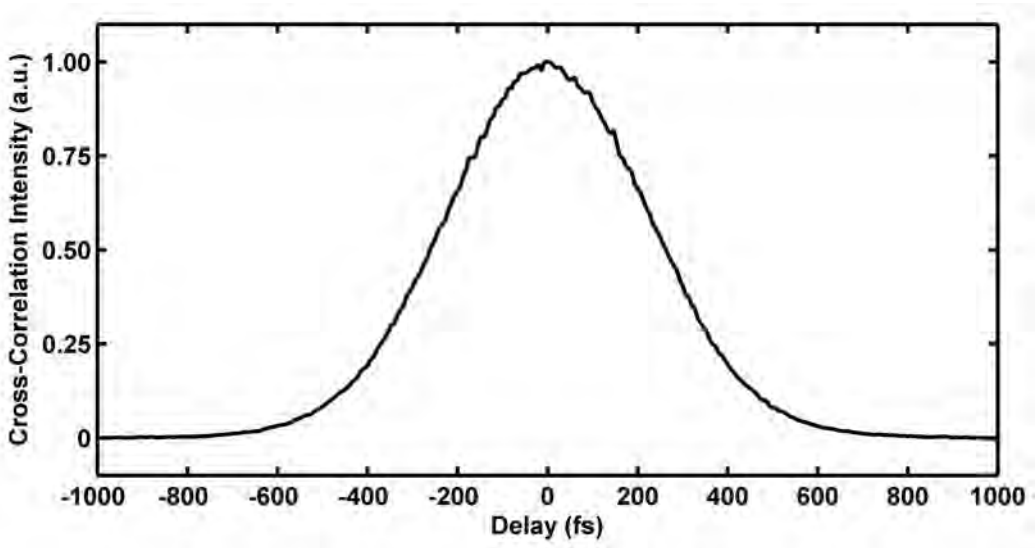


**Figure 3.13**: Experimentally measured pump-probe microscopy cross-correlation in ZnO with 730 and 810 nm pulses using the setup depicted in Figure 3.9.

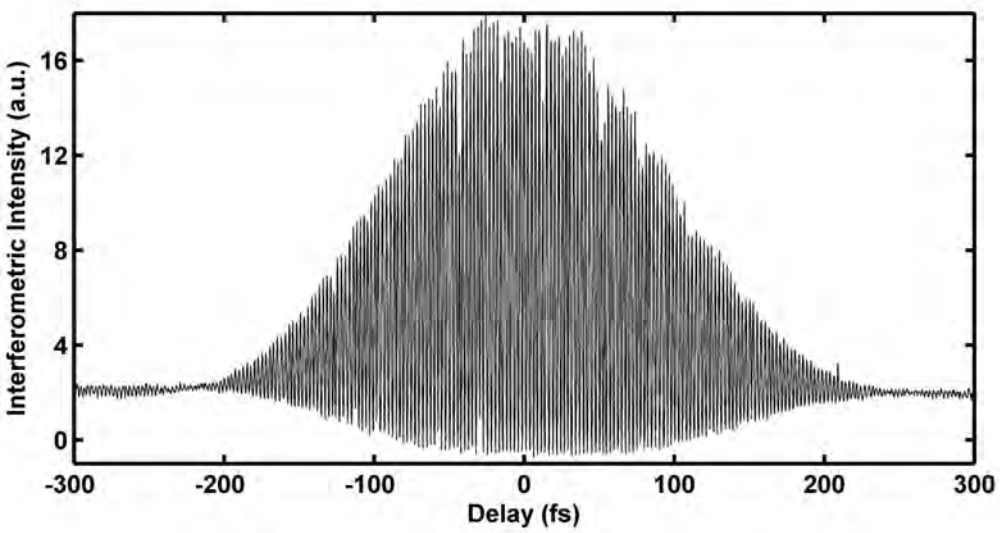


**Figure 3.14:** Experimentally measured microscopy fringe-resolved interferometric autocorrelation in lithium niobate powder at 800 nm using the setup depicted in Figure 3.11. While a characteristic 8:1 ratio exists, assuming an initial gaussian or $sech^2$ pulse fit this autocorrelation poorly.

### 3.3. SPATIAL RESOLUTION

In imaging spatial resolution is ultimately limited by diffraction. When imaging with a microscope objective a diffraction limited spot it achieved when the input beam overfills the input aperture of the microscope objective. In doing so, the input beam is truncated where the input aperture acts as a pupil. As to be shown, the greater the truncation the smaller the focused spot size and consequently, greater spatial resolution. On the other hand, greater truncation results in a larger power loss.

In order to determine the optimum truncation consider the following. When light uniformly illuminates a circular aperture the wave nature of light results in a far-field diffraction pattern. The intensity distribution in the far-field is displayed in Figure 3.15.[40-44]

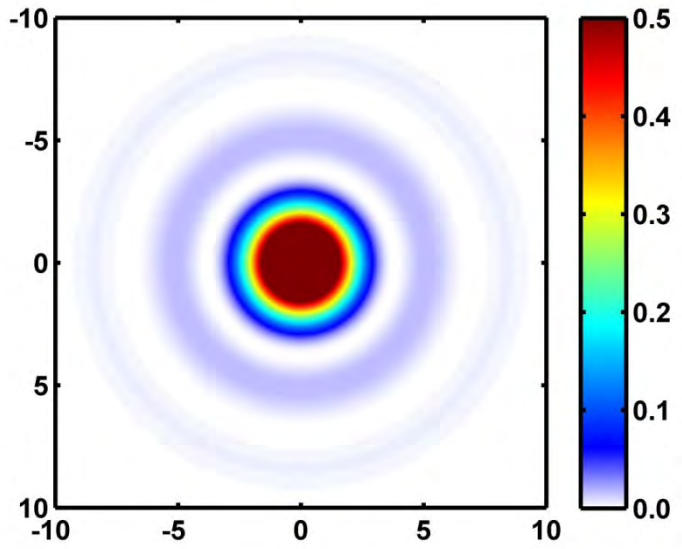


**Figure 3.15:** The diffraction pattern resulting from a uniformly illuminated circular aperture. The central bright region is known as the Airy disc. A series of less intense concentric rings surround the Airy disc. The rings are separated by regions where the intensity distribution goes to zero. The color bar has been scaled to 50% for ease of viewing the surrounding rings.

The intensity distribution as a function of angle of observation in the far-field, $\theta$ is given by the following,

$$I(\theta) = I_0 \left( \frac{2J_1(x)}{x} \right)^2 \tag{3.13}$$

where,

$$x = kasin(\theta)$$

Here, $k$ is the wavenumber and $a$ is the radius of the aperture. In Eq. 3.13, $J_1(x)$ is the Bessel function of the first kind of order one described by,

$$J_1(x) = x \sum_{n=1}^{\infty} (-1)^{n+1} \frac{x^{2n-2}}{(n-1)!\, n!\, 2^{2n-1}} \tag{3.14}$$

The location where the intensity goes to zero is found by solving for the roots of $J_1(x)$,

$$J_1(I(\theta) \to 0) = 3.8317, 7.0156, 10.1735 \ldots \quad (3.15)$$

Consequently, the location of the first dark ring (i.e. where the intensity is zero) is given by,

$$sin\theta = \frac{3.8317}{ka} = \frac{3.8317\lambda}{\pi d} \quad (3.16)$$

Here, $d$ is the diameter of the aperture. Eq. 3.16 is used to determine the diffraction limited spatial resolution.

The Rayleigh criterion is the standard for calculating the maximum possible spatial resolution. Consider two point sources. An image is considered to be diffraction limited when the center the Airy disk from point #1 overlaps the first dark ring $J_1(I(\theta) \to 0) = 3.8317$ of point #2. Mathematically, this distance, $\Delta l$ is described by the following,

$$\Delta l = Rsin\theta = \frac{3.8317\lambda R}{\pi d} = \frac{3.8317\lambda}{\pi} f/\# = \frac{3.8317\lambda}{2\pi NA} \quad (3.17)$$

Here, $R$ is the distance between the aperture and far-field image screen, $f/\#$ is the f-number of the lens, and $NA$ is the numerical aperture of the microscope objective.

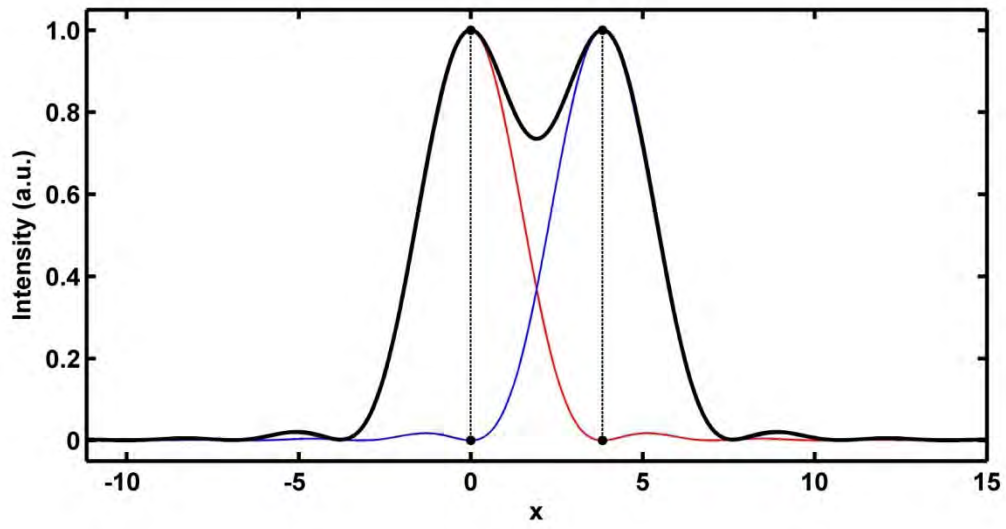


**Figure 3.16:** Two point sources are diffraction limited spatially resolved when the Airy disc from the first point source (red) is overlapped with the first dark ring of the second point

source (blue) (Rayleigh criterion). The sum of the two sources is displayed as a solid black line. The overlap of the Airy discs and first dark rings are represented as dotted black lines.

However, in microscopy illumination is not generally uniform. Consequently, any overfilling of the input aperture of the microscope objective results in a truncation of the assumed Gaussian profile. In fact, Gaussian illumination results in a Gaussian intensity profile, neglected of an Airy pattern. On the contrary, when illumination is in between a uniform and spatially distributed intensity profile, a hybrid of the two results. The truncation ratio, $T$ is defined as the Gaussian beam diameter, $D_b$ to the limiting aperture diameter of the lens, $D_t$,

$$T = \frac{D_b}{D_t} \tag{3.18}$$

The Gaussian beam diameter is defined as the point where the intensity drops to $1/e^2$ of its initial value (i.e. 13.5%). The diameter, $d$ of a diffraction limited spot is consequently adjusted from Eq. 3.16 to account for varying truncation.

$$d = \frac{K\lambda}{2NA} \tag{3.19}$$

For a given truncation ratio, $T$ the $K$value at $1/e^2$ is given by the following,

$$\mathrm{K}_{1/\mathrm{e}^2} = 1.6449 + \frac{0.6460}{(\mathrm{T} - 0.2816)^{1.821}} + \frac{0.6445}{(\mathrm{T} - 0.2816)^{1.891}} \tag{3.20}$$

The greater the truncation, the better the spatial resolution however this is accompanied with a loss in power. The power loss, $P_L$ is given by the following,

$$P_L = \mathrm{e}^{-2(1/T)^2} \tag{3.21}$$

Displayed in Table 3.2 are the diffraction limited diameter proportionalities and fractional power losses at four values of truncation.

| **Truncation Ratio, $T$** | **Diameter Proportionality, $K$** | **Power Loss, $P_L$** |
|---|---|---|
| $\infty$ | 1.6449 | 100% |
| 2.0 | 1.6948 | 60% |
| 1.0 | 1.8303 | 13.5% |
| 0.5 | 2.5105 | 0.03% |

When $T = 2$, a significant amount of the Gaussian profile is truncated such that the aperture is approximately uniformly illuminated and the intensity profile approaches an Airy distribution. While the diffraction limited spot size is only slightly increased by 3% this is also accompanied with an enormous, 60% loss in power. Contrary, when $T = 0.5$ an insignificant amount of the Gaussian profile is truncated such that the aperture is approximately Gaussian illuminated and the intensity profile approaches a Gaussian distribution. However, the diffraction limited spot size is increased 48% compared to when $T = 2$. Finally, when $T = 1$, the Gaussian profile is truncated at the $1/e^2$ diameter and the profile is a hybrid composed of Airy and Gaussian components. This is accompanied a minimum increase in the diffraction limited spot size and only a slight, 13.5% loss in power. Therefore, truncation ratios around 0.7-1.0 are typically used for small diffraction limited spot sizes with minimum power losses.

Two-photon microscopy involves the simultaneous absorption of two photons to promote an electron to an excited state followed by detection of fluorescence. To increase the probability of two photons interacting simultaneously requires the concentration of photons in space and time. Spatial concentration is achieved through focusing from a high

numerical aperture objective. Temporal concentration is obtained by use of ultrafast < 100 fs high repetition rate laser pulses. Since, fluorescence only arises from the focus in two-photon microscopy the effective resolution is generally better than confocal methods where scattering photons reduce the spatial resolution. The intensity near the focal volume in two-photon microscopy is described by the by the illumination point spread function, $IPSF(x, y, z)$. Given that two-photon absorption is proportional to the square of the intensity (Eq. 2.46) the optical resolution is better described by $IPSF^2$. The diffraction limited lateral, $\omega_{xy}$ and axial, $\omega_z$ radii at $1/e$ of the $IPSF^2$ for a two-photon microscope have been approximated by authors Richards and Wolf,[22,45,46]

$$\omega_{xy} = \left\{ \begin{array}{ll} \dfrac{0.320\lambda}{\sqrt{2}NA} & NA \leq 0.7 \\ \dfrac{0.325\lambda}{\sqrt{2}NA^{0.91}} & NA > 0.7 \end{array} \right\}$$
$$\omega_z = \frac{0.532\lambda}{\sqrt{2}}\left[\frac{1}{n - \sqrt{n^2 - NA^2}}\right] \tag{3.22}$$

Here, $\lambda$ is the wavelength, $NA$ is the numerical aperture of the objective, and $n$ is the index of refraction of the medium between the sample and objective. For a dry, $n = 1$ and $NA = 0.8$ and an input wavelength $\lambda = 730$ nm the diffraction limited lateral and axial radii as well as the two-photon focal volume at $1/e$ are calculated as follows,

$$\omega_{xy} = 205.5 \text{ nm}$$
$$\omega_z = 686.5 \text{ nm} \tag{3.23}$$
$$V_{TPE} = \frac{\pi^{3/2}\omega_{xy}^2\omega_z}{0.68} = 0.238 \text{ μm}^3$$

Conversions to the FWHM and $1/e^2$ radius can be obtained by multiplication by $2\sqrt{\ln 2}$ and $\sqrt{2}$ respectively.

Empirically, the spatial resolution of a two-photon microscope can be measured by raster scanning the focused laser over an emitting point source. This is easily achieved with sub-resolution florescent beads or quantum dots. The resulting image is a convolution of the point spread function of the laser with the point source.

Displayed in Figure 3.17 is an example of two different convolutions. The point spread function (B1 & B2) is a two-dimensional Gaussian. When an object (A1) has features that are much smaller than the point spread function, the resulting convolution (image C1) is unable to resolve the fine detail of the object. Conversely when the object (A2) is essentially a point, the resulting convolution (image C2) is that of the point spread function.

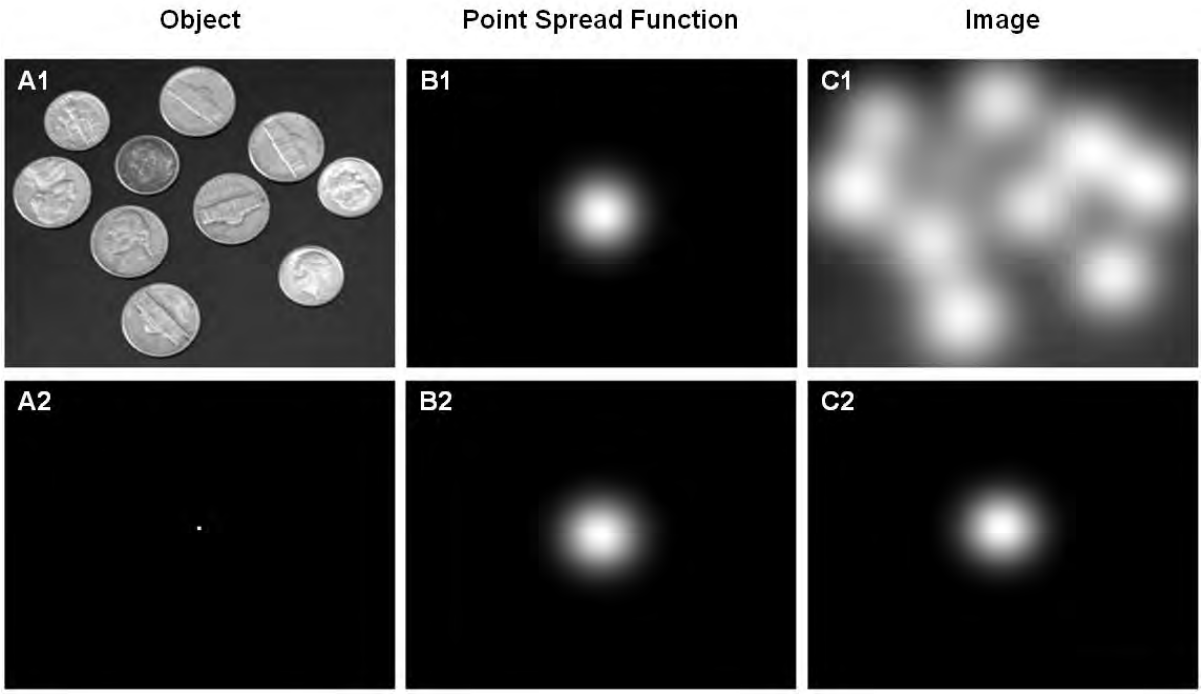


**Figure 3.17:** Convolutions of an object and point spread function and generated image. (A1, A2) Objects (coins and point). (B1, B2) Gaussian point spread function. (C1, C2) Resulting images. The point spread function can only resolve details that are much larger than the object.

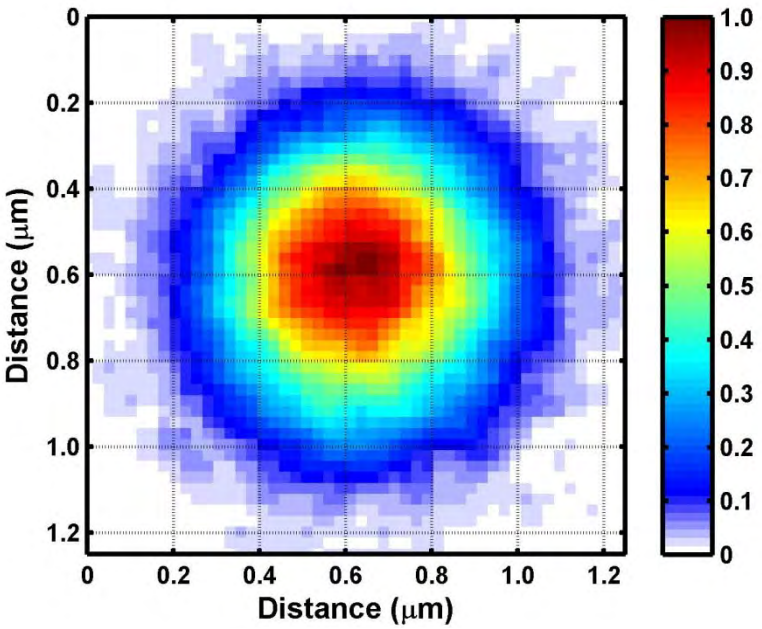


**Figure 3.18:** Experimental convolution of 100 nm quantum dot with 810 nm laser pulse. The experimental calculated FWHM is approximately 500 ±25 nm. Using Eq. 3.23, the theoretical FWHM is calculated to be 380 nm.

### 3.3.1. Thermal Fluctuations

Thermal fluctuations add complexity to spatially resolved measurements. For a given increase or decrease in temperature an object expands or contracts respectively based on their corresponding expansion coefficients. These small fluctuations influence the spatial stability and in the described experiments originate from two major sources, the excitation source and mechanical stages. Small thermal instabilities from excitation source (Ti:Sapphire / OPO) shifts the propagation direction of the output. Consequently, a slight change in output changes the input onto the microscope objective and subsequently the location of excitation. Further, mechanical drift from both nano and course positioning stages changes the location of the sample. The combined affect can be observed by raster-scanning an image at various times. The degree of the collective thermal drift is determined by the magnitude of xyz-

translations from the scanned images. Displayed in Figure 3.19 is a series of sixteen fluorescence based images from 2.0 μm, nile red, FluoSpheres® carboxylate-modified microspheres (Invitrogen). The images were taken throughout the day over a period of 4 hours and 33 minutes at a resolution of 100 nm. The images are translated relative to one another in both X and Y axes. Plotted in Fig. 3.20 (left) is the translation in nanometers X and Y relative to image #1. The maximum X-axis translation is 500nm ± 100nm whereas the maximum Y-axis translation is 700nm ± 100nm. In addition to translation in the image plane the signal magnitude also varies as a function of time. Plotted in Figure 3.20 (right) is the integrated intensity normalized to image #1. The signal variations could originate from laser power fluctuations or more problematic focal plane drift related to piezoelectric positioning of the microscope objective.

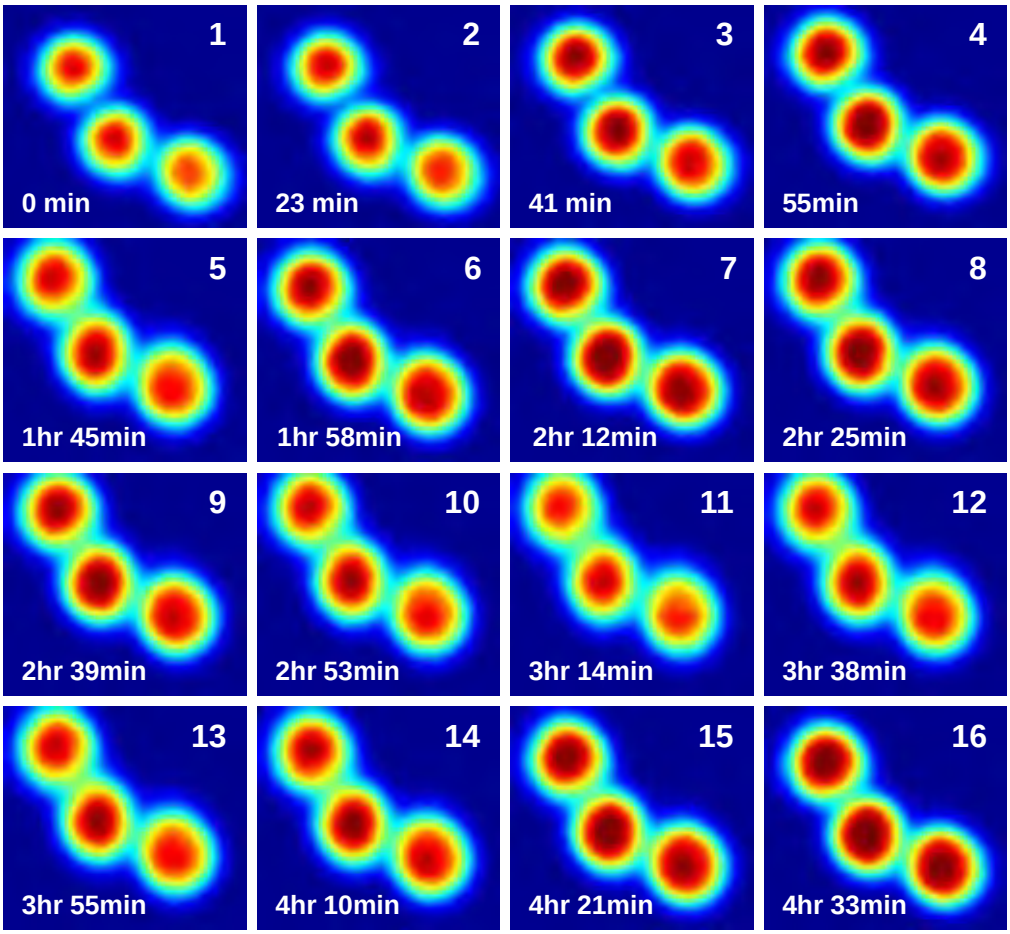


**Figure 3.19:** Fluorescence imaging of 2.0 µm nile red beads taken over a period of 4 hours and 33 minutes. Translation in all three axes is observed (X & Y-axis image plane translation; Z-axis signal intensity).

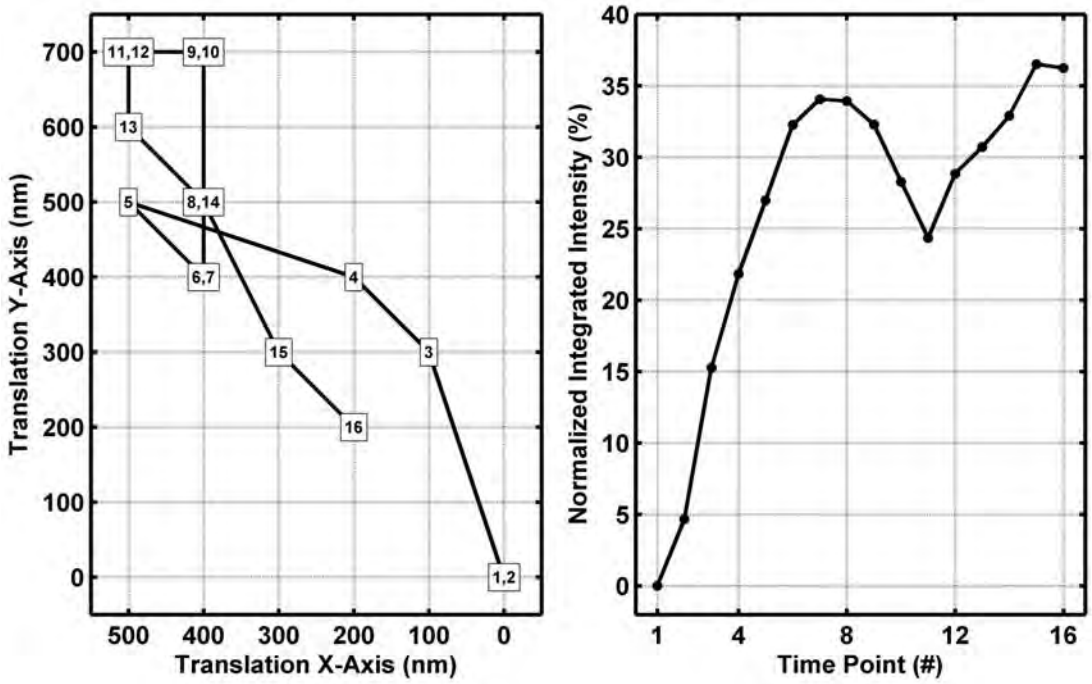


**Figure 3.20:** Translation of X & Y-axis (Left) and normalized integrated intensity (Right) for the sixteen fluorescence images relative to image #1 (Figure 3.19).

# CHAPTER 4. ZNO BACKGROUND

## 4.1. BAND STRUCTURE

The natural crystal structure of ZnO is of hexagonal wurtzite with lattice constants: $a = b = 3.249$Å, $c = 5.2042$ Å and lattice angles: $\alpha = \beta = 90°$, $\gamma = 120°$. This corresponds to a density of 5.675 g/cm$^{-3}$. The point and space groups for hexagonal wurtzite ZnO is 6mm, $P6_3mc$ in international notation and $C_{6v}$, $C^4_{6v}$ in Schoenflies notation respectively.[47] Displayed in Figure 4.1 is the crystal structure of hexagonal wurtzite ZnO.

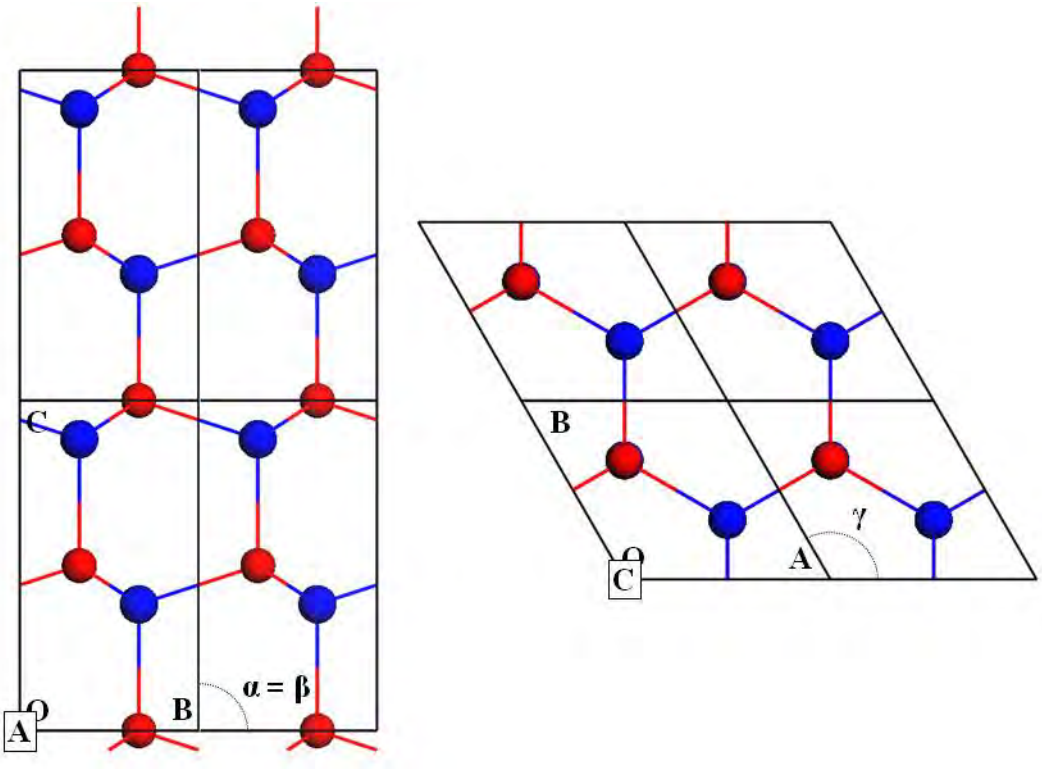


**Figure 4.1:** Crystal structure of hexagonal wurtzite ZnO.

For an atom the transfer of energy is quantized and transitions occur between energy levels described by their corresponding atomic orbitals. As atoms combine to form a solid the overlap of the wavefunctions and their mutual interactions creates a series of energy bands. It is the energetics of these bands that determine the fundamental properties of solid state materials. As opposed to atomic energy levels, the calculation of energy bands in solid

materials is an extremely difficult problem due to the abundance of interacting particles. However, the dispersion (energy vs. wavevector) of solid state materials may be estimated using one-electron approximations.[35]

First, consider the dispersion of a free electron of mass, $m_0$ which is derived from solving the Schrödinger equation for an electron trapped in a box with zero potential energy.

$$E = \frac{\hbar^2 k^2}{2m_0} \tag{4.1}$$

The dispersion of a free electron $E(k)$ is parabolic and is displayed in Figure 4.2 as a solid black line. Notice that free electrons can acquire any value of $k$. Conversely, the dispersion is absent of any discontinuities. However, for electrons in solid state materials, periodic potentials generate energies in which no eigenvalues exist referred to as band gaps. Three different energy bands and corresponding band gaps are displayed in color in Figure 4.2

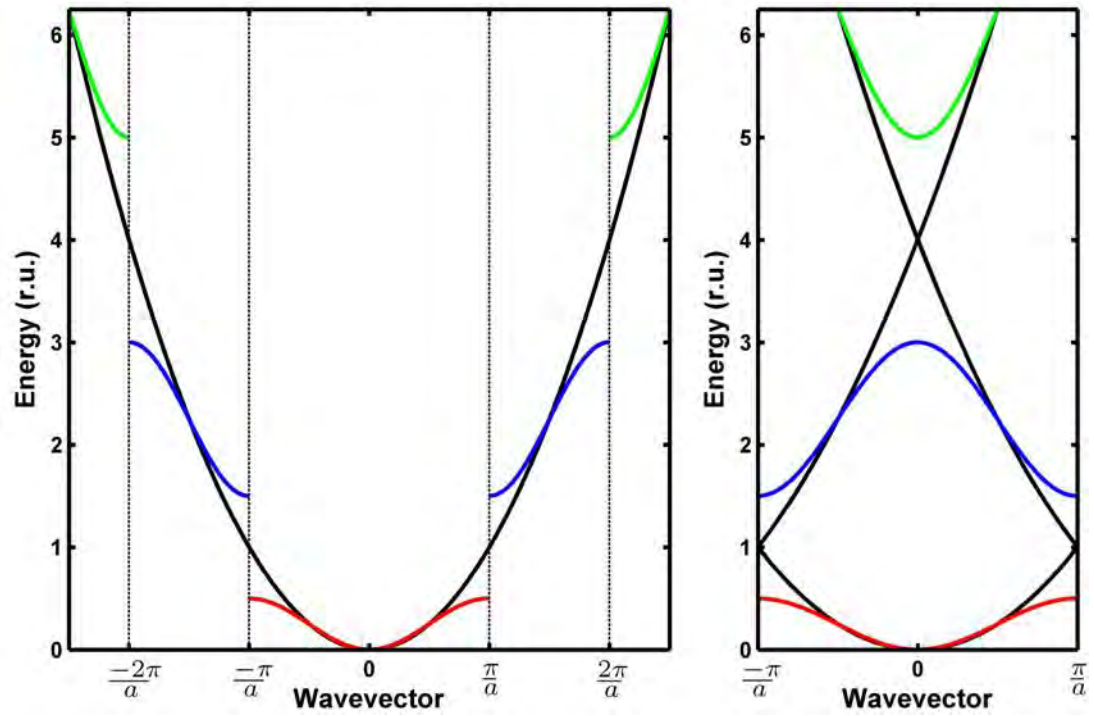


**Figure 4.2:** (Left) Dispersion of a free electron (black) and an electron in a periodic potential (color) plotted in an extended zone scheme. The Brillioun zones are indicated by

dotted black lines. (Right) Dispersion of a free electron (black) and electron in a periodic potential (color) in a reduced zone scheme.

The source of these energy gaps can be determined by considering an electron in a one-dimensional periodic lattice where the negatively charged electrons and the positive nuclei produce a periodic potential. This periodic potential can be approximated as a sum of Columbic potentials innate to the individual atoms within the lattice. When the wavelength of the electron is far from the lattice constant, $a$: the distance between lattice atoms; the electron moves freely and the dispersion may be approximated by Eq. 4.1. On the other hand, when the wavelength of the electron approaches the lattice constant the electron wave is back-scattered (Bragg diffraction) and a standing wave is formed. This is the physical origin of the band gap in solid state materials, where forbidden electron energies exist due to the interference that occurs at the Brillioun zone boundaries, $k = \pm\pi/a$. Further, at the Brillioun zone the group velocity, $v_g$ of the electron is zero,

$$v_g = \frac{1}{\hbar}\frac{\partial E}{\partial k_{k=\pm\pi/a}} = 0 \tag{4.2}$$

The simplest description of a standing wave in one-dimension is given by the combination of oppositely traveling wavefunctions.

$$\begin{aligned} \psi_+ &= e^{ikx} + e^{-ikx} = 2cos\left(\frac{\pi x}{a}\right) \\ \psi_- &= e^{ikx} - e^{-ikx} = 2isin\left(\frac{\pi x}{a}\right) \end{aligned} \tag{4.3}$$

The corresponding electron probability densities can then be described as followed,

$$\rho_+ = \psi_+\psi_+^* \propto cos^2\left(\frac{\pi x}{a}\right)$$
$$\rho_- = \psi_-\psi_-^* \propto sin^2\left(\frac{\pi x}{a}\right) \tag{4.4}$$

Displayed in Figure 4.3 is a periodic potential composed of a series of Coulombic potentials overlaid with the electron probability densities. The electron probability density, $\rho_+$ has its maximum electron density when the potential is at its greatest magnitude. This occurs at atomic lattice sites, $x = na$. While, $\rho_-$ has its maximum electron density in between the atoms, $x = na/2$. The different potential energy interaction with the electron wavefunctions results in different energies. The electron wavefunction, $\psi_+$ will feel a greater attractive force to the positive nuclei when compared to $\psi_-$. Consequently, $E_+$ will lye lower in energy than $E_-$, the difference resulting in a band gap.

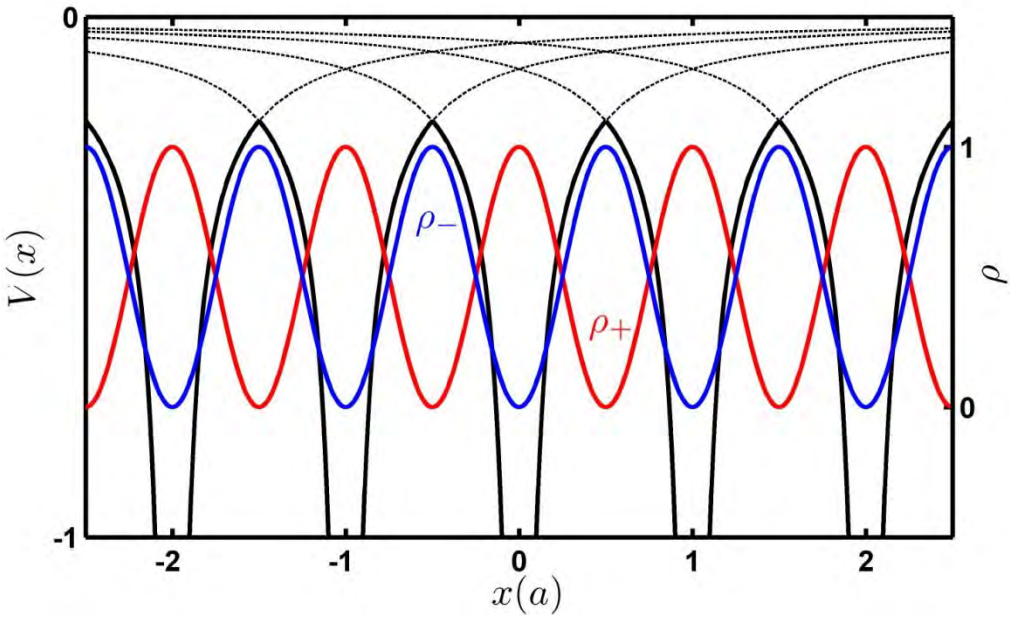


**Figure 4.3:** A periodic potential composed of a series of Columbic potentials: $V(x) = \frac{q_1 q_2}{4\pi\varepsilon_0}\frac{1}{x}$, in reduced units $\frac{q_1 q_2}{4\pi\varepsilon_0} = 0.1$ (black lines) overlaid with probability density, $\rho_+$ (red lines) and $\rho_-$ (blue lines).

Electrons fill the energy bands according to Fermi-Dirac statistics. The bands that are completely filled when at T = 0 K are referred to as valence bands where as partly or empty bands are conduction bands. The energy gap between the conduction band and valance band is known as the fundamental band gap, $E_g$. A material is metallic if any conduction bands are partly filled at T = 0 K, while semiconductors are defined as having a fundamental band gap between $0 < E_g < 4\ eV$ and insulator when $E_g \geq 4$ eV. ZnO is a semiconductor with a fundamental band gap of approximately 3.4 eV (Figure 4.4).

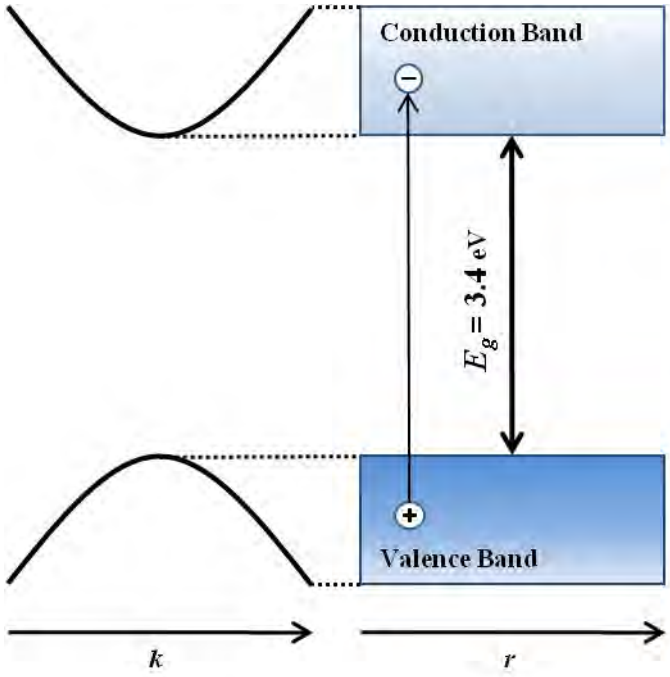


**Figure 4.4:** Illustration of dispersion and corresponding energy diagram for ZnO in spatial coordinates. The fundamental band gap is approximately $E_g = 3.4$ eV.

## 4.2. EXCITONS

Optical transitions occur between the fundamental band gap where electrons are promoted to the conduction band and analogous holes are left in the valence band (Figure 4.4). Holes have a positive charge with a wave vector and spin that are opposite to the

removed electron. The Coulombic attraction between the negatively charged electron and the positively charged hole results in a new quasi-particle, the exciton. This electron-hole pair is analogous to the hydrogen atom. As a result, a series of excitonic energy states lie below the band gap and are described by the following,

$$E_{ex}(n, \boldsymbol{K}) = E_g - E_b \frac{1}{n^2} + \frac{\hbar^2 \boldsymbol{K}^2}{2M} \tag{4.5}$$

with the principle quantum number $n = 1,2,3, \ldots$, exciton binding energy,

$$E_b = 13.6eV \frac{\mu}{m_0} \frac{1}{\varepsilon^2} \tag{4.6}$$

translation mass of the exciton,

$$M = m_e + m_h \tag{4.7}$$

and translational wavevector wave vector of the exciton,

$$\boldsymbol{K} = \boldsymbol{k}_e + \boldsymbol{k}_h \tag{4.8}$$

where $m_0$ is the free electron mass, $m_e$ and $m_h$ are the effective mass of the electron and hole respectively, and $\mu$ is the reduced mass,

$$\mu = \frac{m_e m_h}{m_e + m_h} m_0 \tag{4.9}$$

An illustration of the excitonic transitions for ZnO is displayed in Figure 4.5. The valence band in ZnO is split into three non-degenerate bands from the spin-orbit coupling and hexagonal crystal field. The exciton binding energy has been measured for ZnO and is approximately $E_b = 60$ meV.[48] The exciton Bohr radius, the radial distance between the electron-hole pair is given by the following,

$$a_B^{ex} = a_B^H \varepsilon \frac{m_0}{\mu} \tag{4.10}$$

The excitonic Bohr radius is approximately $a_B^{ex} = 1.8$ nm. With a lattice constant of $a = 3.2$ Å the exciton extends over many unit cells (Figure 4.5) and are referred to as Wannier excitons. Compared to other direct semiconductors ZnO has a relatively high exciton binding energy and fundamental band gap (Figure 4.6).

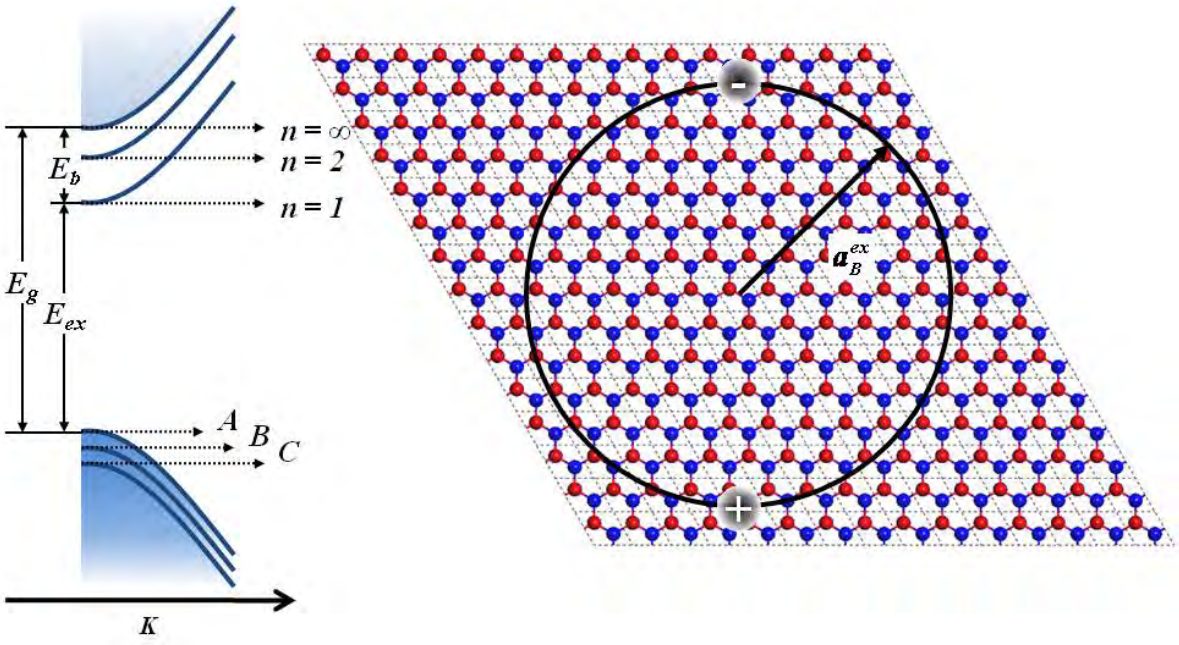


**Figure 4.5:** (Right) Illustration of excitonic energy levels from the A valence band. (Left) Illustration of an exciton overlaid on top of ZnO's crystal lattice.

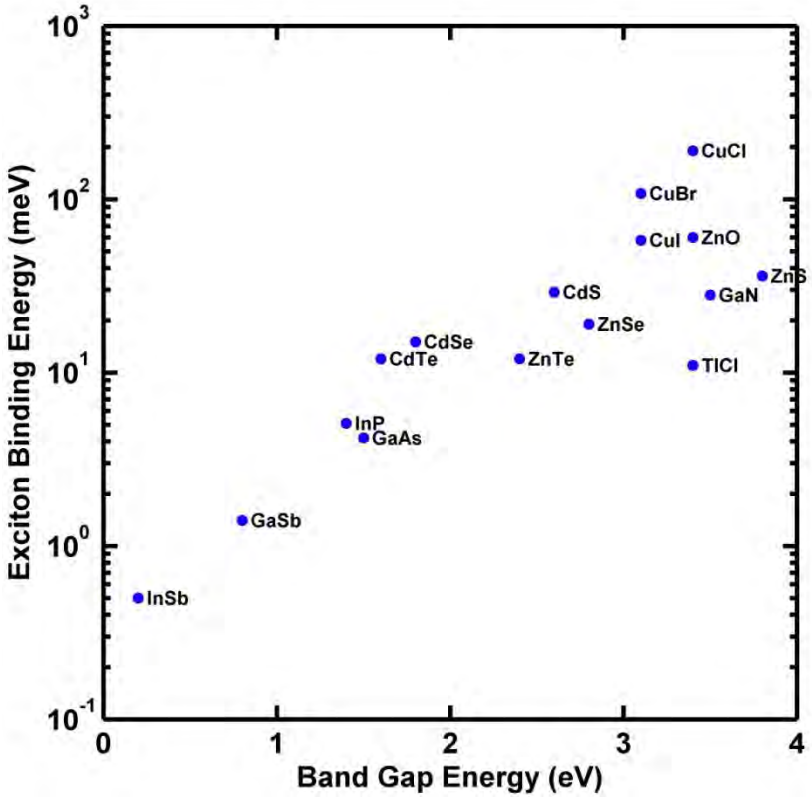


**Figure 4.6:** Comparison of exciton binding energy vs. band gap energy for a series of direct gap semiconductors.[47]

### 4.3. HIGH-DENSITY EFFECTS

In systems where high densities of electron-hole pairs are generated free carriers screen the Columbic interaction between the electrons and holes within excitons. The Coulombic screening is generally modeled as a Yukawa potential,

$$V(|\overrightarrow{r_e} - \overrightarrow{r_h}|) = \frac{-e^2}{4\pi\varepsilon_0\varepsilon(n_p)} \cdot \frac{1}{|\overrightarrow{r_e} - \overrightarrow{r_h}|} e^{-\frac{|\overrightarrow{r_e} - \overrightarrow{r_h}|}{l_s}} \quad (4.11)$$

where $l_s$ is the screening length.[35,49,50] Plotted in Figure 4.7 is a Yukawa type potential for a series of screening lengths. For a small screening length the potential decays to zero faster than a Columbic potential ($l_s = \infty$).

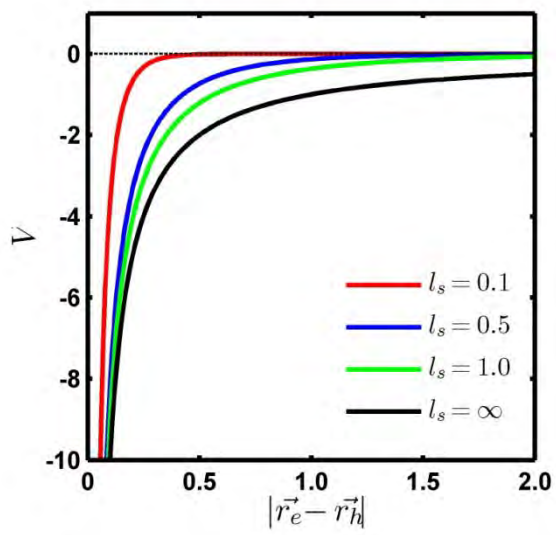


**Figure 4.7:** A Yukawa type potential as a function of vector distance between electrons and holes, $|\vec{r_e} - \vec{r_h}|$ for a series of screening lengths, $l_s$. The potential becomes Coulombic for an infinite screening length. The potential has been normalized such that $-e^2/4\pi\varepsilon_0\varepsilon(n_p) = 1$.

As the number of electron-hole pairs, $n_p$ increases the screening length is decreased and the exciton binding energy, $E_{ex}^b$ is reduced. At a critical screening length, $l_c \rightarrow E_{ex}^b(n_p) = 0$ individual excitons are no longer distinguishable from one another and a collective electron-hole plasma (EHP) is created. The electron-hole pair density at which the crossover between the excitonic and EHP regimes occurs is referred to as the Mott density, $n_m$. (Figure 4.8).

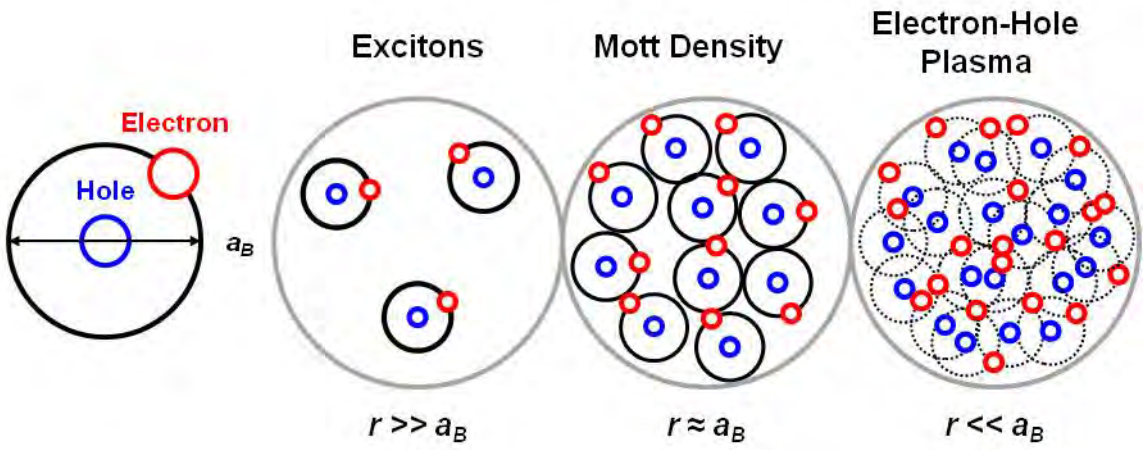


**Figure 4.8:** Illustration of electron-hole pairs at three carrier densities. When $n_p$ is low such that the radius between excitons, $r$ is much larger than the exciton Bohr radius, $a_B$ the electron-hole pairs are well described as excitons. However when $n_p$ is high such and $r \gg a_B$ free carrier screening interrupts the exciton binding energy and the collection of carriers is referred to as an electron-hole plasma. The Mott density occurs when $r \approx a_B$.

A simple approximation of the Mott density is determined by considering the relationship between the exciton Bohr radius and the critical screening length in a static Columbic potential [35,51]

$$\frac{a_B}{l_c} = 1.19 \tag{4.12}$$

Additionally, Debye-Hückel screening theory gives a reasonable approximation for the critical screening length at room temperature. The Debye-Hückel screening length, $l_{DH}$ is given by the following relationship,

$$l_{DH} = \sqrt{\frac{\varepsilon_0 \varepsilon k_B T}{e^2 n_p}} \tag{4.13}$$

Replacement of $l_{DH}$ in Eq. 4.13 for $l_c$ in Eq. 4.12 results in a simple equation for determining the Mott density at room temperature that depends on the reduced excitonic Rydberg energy units, $Ry^*$ and exciton Bohr radius.

$$n_M = (1.19)^2 \frac{\varepsilon_0 \varepsilon k_B T}{e^2 a_B^2} = (1.19)^2 \frac{k_B T}{2 a_B^3 Ry^*}$$

where (4.14)

$$a_B Ry^* = \frac{\hbar^2 \varepsilon \varepsilon_0}{\mu e^2} \cdot \frac{e^4 \mu}{2(\varepsilon \varepsilon_0)^2} = \frac{e^2}{2 \varepsilon \varepsilon_0}$$

Using typical values for ZnO; $Ry^* = 60$ meV and $a_B = 1.8 \times 10^{-9}$ m, the approximation of the Mott density becomes: $n_M \approx 5.0 \times 10^{19}$ cm$^{-3}$.

As stated above, when $n_p$ increases the exciton binding energy decreases. However, the absolute energy of the exciton is maintained. This is attributed to screened carriers which are compensated by the renormalization of the band-gap. The reduction of the band gap as $n_p$ increases is due to a combination of exchange and correlation interactions. The exchange energy encompasses a reduction of repulsive energy of the system by increasing the average distance between electron-electron and hole-hole pairs with parallel spin as a result of the Pauli exclusion principle. While the correlation energy is spin independent and refers to the preferred distribution between holes and electrons, where an electron (hole) will be found with a higher probability in the vicinity of hole (electron), further reducing of the total energy of the system.

The shift in band gap energy, $\Delta E_g$ is calculated by the following,[52]

$$\Delta E_g = \frac{\partial}{\partial n_p}\left(n_p E_{xc}\right) \quad (4.15)$$

where, $E_{xc}$ is sum of exchange and correlation energies. While there are numerous theoretical methods for determining the exchange and correlation energies [51-60], Vashishta and Kalia,[58] found that $E_{xc}$ is nearly independent of band-structure details, including electron-hole mass ratio, degeneracy, and anisotropy of band extrema. Consequently, calculations from a self consistent approximation has yielded a universal equation describing $E_{xc}$ in reduced excitonic Rydberg energy units ($Ry^*$) (i.e. for ZnO; $Ry^* = 60$ meV).

$$E_{xc} = \frac{-4.8316 \pm 5.0879 r_s}{0.0152 + 3.0426 r_s + r_s^2} \quad \text{(4.16)}$$

where

$$r_s = \left( \frac{3}{4\pi a_B^2 n_p} \right)^{1/3}$$

In the above equation $r_s$ is a normalized distance that is equal when the average volume allotted to each electron-hole pair in the plasma equals the volume of the exciton. Plotted in Figure 4.9 is the renormalization of the band gap energy as a function of both the normalized distance and electron-hole carrier density. A second equivalent definition of the Mott density is defined when band gap energy is renormalized such that it is equivalent to the absolute exciton energy, $E_g(n_p) = E_{ex}$. In Figure 4.9 the Mott density occurs at the intersection of $\Delta E_g(Ry^*) = -1$; $r_s \approx 4.7$ and $n_p \approx 4 \times 10^{17}\text{cm}^{-3}$. For ZnO Mott densities have been experimentally determined from $10^{17}\text{cm}^{-3}$ to $10^{19}\text{cm}^{-3}$.[35,51,61-64]

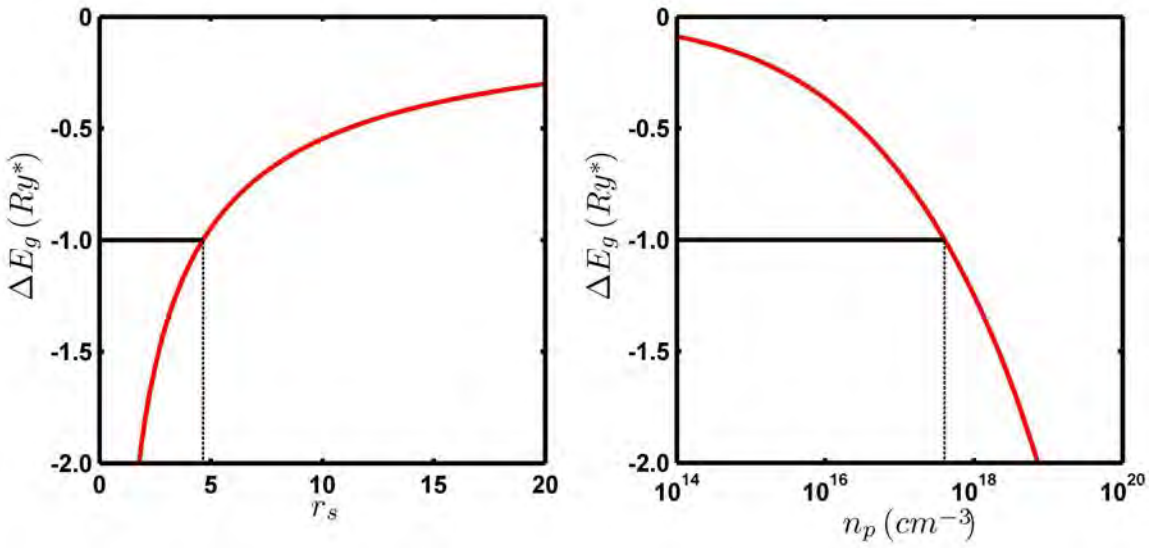


**Figure 4.9:** (Left) Band-gap renormalization energy, $\Delta E_g$ (red) in reduced exciton Rydberg energy as a function of normalized distance $r_s$. The intersection of the exciton binding energy occurs at $r_s \approx 4.7$. (Right) band-gap renormalization energy, $\Delta E_g$ (red) as a function of electron-hole pair density, $n_p$ given by (Eq. 1.3). The maintained absolute exciton binding energy (solid black) and Mott density $n_m \approx 4 \times 10^{17}\text{cm}^{-3}$, (dotted black) are also displayed.

# CHAPTER 5. DIRECT IMAGING OF OPTICAL CAVITY MODES IN ZNO RODS USING SECOND-HARMONIC GENERATION MICROSCOPY

## 5.1. INTRODUCTION

The increasing demand for miniature optoelectronic and photonic devices that access new spectral regions has fueled intense interest in a variety of wide band gap semiconductors that assume complex geometrical architectures.[63,65] Exciton emission is ideal for many applications but restricts operating wavelengths, limiting device applications. Second-harmonic generation (SHG) and other nonlinear mixing processes have the potential to circumvent this limitation. Efficient SHG requires a large second-order susceptibility ($\chi^{(2)}$) and a mechanism to maintain phase coherence between the fundamental and second-harmonic optical waves, i.e., phase matching. In many common bulk SHG materials, with large $\chi^{(2)}$ values, phase-matching is achieved by exploiting an intrinsic birefringence. However, the formation of these materials into nanostructures is limited.[66] On the other hand, there are many semiconductors that have large $\chi^{(2)}$ values and can also adopt intricate forms, but they often lack the capacity to achieve phase matching through conventional means.[67,68]

Cavity modes in micro-structured materials can play an important role in the nonlinear mixing processes, resulting in new phenomena not present in macroscopic systems. For example, micro-resonators formed from second-order materials can circumvent phase-matching and exhibit efficient SHG when the fundamental and/or second-harmonic optical fields are resonant with cavity eigenmodes.[67-75] Experimental observations of this phenomenon date back to the 1960s when Ashkin et al.[69] explored the enhancement of SHG in KDP though optical cavity resonance. More recent efforts used electrochemical, photolithographic, and molecular beam epitaxy techniques to develop complex high-finesse cavities in order to achieve a quasi-phase matching condition with increased conversion

efficiency. In addition to efficiency enhancement, microcavity resonances can result in phase matching conditions that yield second-harmonic intensity propagating in new directions. The second-harmonic produced in conventional frequency doubling emerges collinear with the fundamental, in the forward scattered direction; however, microcavities can produce a counter propagating beam as well. This back scattered radiation, which could be thought of as arising from a standing polarization wave, cannot be achieved in bulk materials and is one signature of the optical cavity's influence on the SHG process. While most examples of cavity effects in nonlinear mixing have come from engineered systems, similar effects should be visible in nanoscale structures that have well-defined cavity eigenmodes. Here the shape of the object (e.g., rods, ribbons, tetrapods, etc.) can lead to more complex cavity modes and is expected to play an even greater role in the nonlinear mixing process.

Zinc oxide has emerged as an ideal material for exploring structurally dependent optical phenomena.[61] The diverse set of synthetically available crystalline structures that include wires, rods, and tetrapods provide an array of complex geometrical architectures to investigate.[76] Its wide band gap (3.37 eV, 368nm) and strong exciton binding energy (60 meV)[48] lead to an intense violet-blue emission under UV excitation that is targeted for many next generation optical device applications. When an object's dimensions are comparable to the wavelength, its size and shape play a central role in determining its optical properties. The hexagonal cross section of the ZnO structure can support both Fabry-Pérot (i.e., standing wave) and whispering gallery modes, and several groups have studied the effects of these optical resonator modes on the ZnO photoluminescence.[77-82] Optical waveguiding and photon confinement are observed in a variety of structures, resulting in modulated spectral properties. These processes, which are integral to the function of many devices including

nanowire lasers,[62] are present even when the transverse dimension is smaller than the emission wavelength. While cavity effects on the emission properties of nanostructured materials have been studied, their influence on second-order nonlinear optical processes has remained largely unexplored.

This chapter examines the effect of cavity modes on the SHG process in individual needle-like ZnO rods using second-harmonic microscopy. The images show areas of cavity-enhanced second-harmonic intensity along the longitudinal axis (c-axis) of the rod that are periodically distributed, symmetrically situated relative to the rod midpoint, and have positions that vary with the fundamental frequency. The spatial modulation is a direct consequence of the fundamental ($\omega$) coupling into cavity modes of the ZnO resonator that are oriented transverse to the rod axis, resulting in enhanced back scattered second-harmonic light. Second-harmonic generation in bulk materials propagates in a forward direction due to phase matching, where as the presence of backward propagating SHG is a direct consequence of nonlinear mixing in a microcavity. Our results point to the potential for exploiting the resonator properties of individual objects, possibly paving the way for the development of novel nonlinear optical devices.

## 5.2. EXPERIMENTAL

The nonlinear microscope consists of an ultrafast laser source coupled to a far-field microscope (Figure 5.1). A mode-locked Ti:sapphire laser (Spectra-Physics: Tsunami) pumped by a 5 W frequency-doubled continuous-wave diode laser (Spectra-Physics: Millenia) is used as the excitation source. The system produces 80 fs pulses at a 76 MHz repetition rate and can be tuned between 720 and 850 nm with a maximum power output of

approximately 1 W. The laser output is sent through a Faraday isolator and prism-pair compressor operated in a double pass configuration. A half-wave plate and polarizing cube serve as a variable attenuator, reducing the average power entering the microscope to about 10 mW. The beam diameter is expanded by a factor of 4 and directed, by reflection off a dichroic mirror (R: 680-1000 nm; T: 360-650 nm), into the objective (Olympus MSPlan 50×, NA 0.8) of an inverted microscope, overfilling its back aperture. Light focused by the objective onto the sample results in two-photon emission and/or second-harmonic generation. Light collected by the objective is transmitted through the beamsplitter, focused onto the entrance slit of a monochromator, and detected by a photomultiplier tube operated in a photon-counting mode. Under typical experimental conditions, a signal photon is detected for every 500-1000 laser pulses. Images are compiled by raster-scanning the excitation spot over the sample using a piezoelectric x-y translation stage with a step-size and reproducibility that are both less than 20 nm. The spatial resolution of the microscope is determined by the size of the laser beam at the focus of the objective. Since the probability of two-photon excitation and second harmonic generation scales with the square of the laser intensity, efficient excitation occurs only at the focal point, resulting in confocal like behavior and a lateral dimension that is smaller than the diffraction limit. The diameter ($\delta$) of the excitation region is estimated[22] from $\delta = 2(\ln 2)^{1/2}\,(0.325\lambda)/2^{1/2}\,NA^{0.91}$ to be approximately 350 nm. Images obtained from 100 nm fluorescent beads yielded a point spread function with a width of ~ 400 nm ZnO.

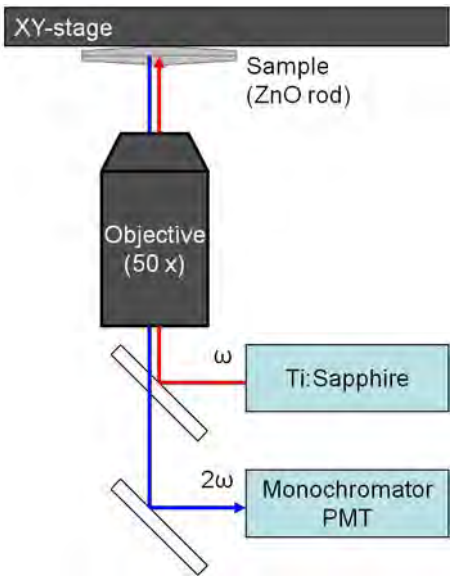


**Figure 5.1:** Schematic representation of the nonlinear microscope. Individual rods are excited by a femtosecond laser pulse from a mode-locked Ti:sapphire laser that is focused to a diffraction limited spot by a microscope objective placed below the sample plane. Two-photon photoluminescence and second-harmonic light emanating from the rod is collected by the objective, transmitted through a dichroic beamsplitter, focused onto the entrance slit of a monochromator and detected by a photomultiplier tube. Imaging is achieved by raster scanning the sample across the focal point of the objective.

## 5.3. SYNTHESIS

ZnO structures were grown using hydrothermal and solution phase techniques adapted from Cheng et al.[83] and Li et al..[84] Rods analyzed in this work are synthesized by incubating a 0.05 M solution of $Zn(NO_3)_2$ and methenamine ($(CH_2)_6N_4$) under hydrothermal conditions for 3 hr at 150 °C. The needle-like rods, which range in length from 1 to 30 μm, are collected on glass slides placed at the bottom of the reaction container. After completion of the reaction, the slide is removed from the container and sonicated in ethanol (200 proof) to harvest the rods. Microscopy samples are prepared by drop casting ~250 μL of the ZnO/ethanol suspension onto a microscope slide. Once the ethanol evaporates, the slide is

placed on the scanning stage with the ZnO rods directly facing the objective lens. Imaging is performed without a coverslip under ambient conditions.

## 5.4. RESULTS AND DISCUSSION

A scanning electron microscopy (SEM) image of a typical ZnO rod is displayed in Figure 5.2A. The SEM image shows a faceted ZnO rod that is ~9 μm in length with a hexagonal cross section whose c-axis is directed along the primary growth direction. The diameter varies along the length of the rod from about 500 nm at the ends to approximately 1.5 μm at its widest point. Figure 5.2E shows the emission spectrum following two-photon excitation at 730 nm (1.70 eV) of the ZnO rod shown in Figure 5.2A. Since the spatial extent of the excitation (400 nm) is smaller than the rod (9 μm), the emission collected by the objective originates from a localized region of the structure, which in this case is the midpoint of the rod. The spectrum contains a sharp SHG peak at 365 nm (3.40 eV), a band edge emission peak at 390 nm (3.18 eV), and a broad peak centered at 550 nm (2.25 eV) that is commonly assigned to trap states arising from defects in the crystal structure.[63] Panels B-D of Figure 5.2 show the images obtained at the second-harmonic, band edge, and trap state emission wavelengths, respectively. The band edge and trap state emission images show increased intensity at the ends of the rod, and a reduction in emission intensity at the midpoint that could be evidence of a grain boundary not observed in the SEM.

The SHG image differs considerably from the two emission images, displaying a periodic pattern of enhanced intensity along the rod axis. Although not apparent in this particular rod, periodic variations are occasionally observed in band edge and trap state emission images; however, the contrast is much lower and exists in only a very small portion

of analyzed rods. While the periodic SHG pattern is a general phenomenon that is reproduced in a large number of needle-like rods, it is not observed in all rod shapes. SHG images of ZnO nanowires obtained by other groups using near-field and far-field methods do not show periodic variation of the type observed here.[82,85] The pattern is also not observed in rods with parallel sides, i.e., rectangular profiles (data not shown), suggesting that the phenomenon is associated with the variation in diameter that occurs along the length of the rod in the needle-shaped structure.

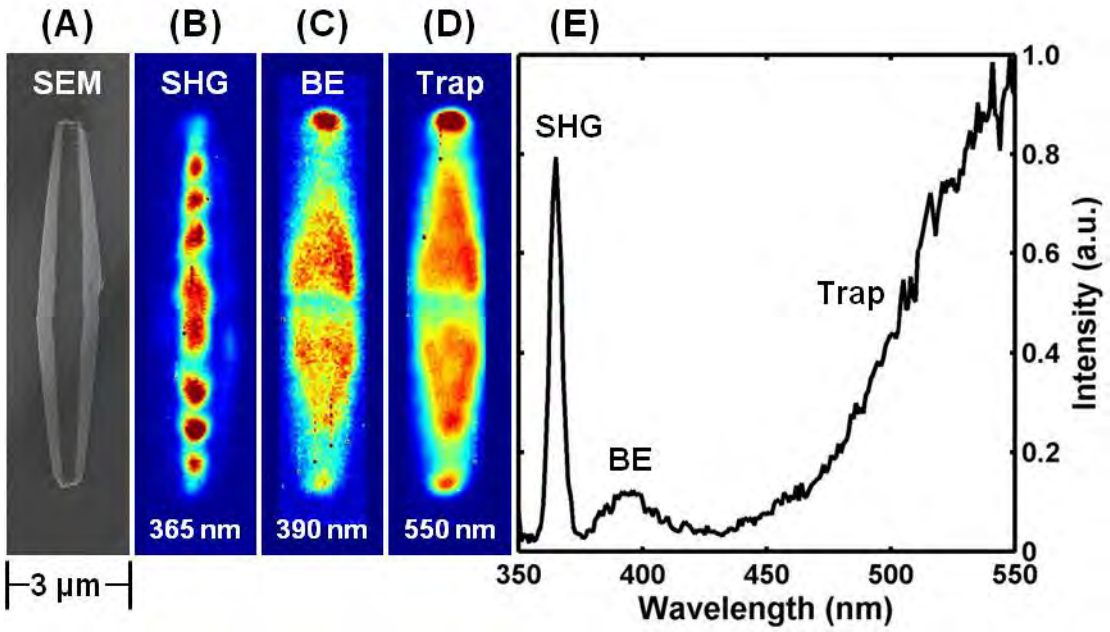


**Figure 5.2:** Nonlinear second-harmonic and two-photon emission microscopy of an individual ZnO rod. (A) Scanning electron microscopy image of a needle-like ZnO rod that is approximately 9 μm in length with its c-axis as the primary growth direction. (B) Second-harmonic microscopy image (365 nm) and two-photon photoluminescence images corresponding to (C) band edge (BE) emission (390 nm) and (D) trap state emission (550 nm) observed following excitation at 730 nm (1.7 eV). Periodic variation is clear in the second-harmonic image, whereas the photoluminescence images show no such variation. (E) The steady-state emission spectrum observed following excitation at the midpoint of the rod.

These observations invoke the question: What is the physical explanation for the periodic pattern? The periodic nature suggests that the phenomenon is linked to optical cavity modes supported by the ZnO resonator. Such an assertion is not without precedence. A variety of ZnO structures are observed to support optical cavity modes, and because of the short cavity lengths, the spacing between adjacent resonances is oftentimes large enough that they can be resolved in the emission spectrum.[62,77-82,86,87] The image in Figure 5.2B is a direct manifestation of the cavity and its affect on the SHG process. In principle the active modes could either lie longitudinal or transverse to the rod axis; however, the geometry of our experiment (Figure 5.1) suggests that it is modes supported by the cross section of the rod that are giving rise to the periodic pattern.

The simplest cavity that can be supported by the hexagonal cross section of a ZnO rod is a Fabry-Pérot resonator formed from two plane-parallel facets (Figure 5.3F). For the needle-like structures, excitation at different points along the rod axis corresponds to interaction with resonators of varying cavity lengths. The intensity of the fundamental stored within a Fabry-Pérot resonator of cavity length $d$ is given by,[1]

$$I_\omega(d) = I_0 \frac{1}{1 + F sin^2\left(2\pi \frac{n_2 d}{\lambda_\omega}\right)} \qquad (7.1)$$

where the finesse $F = 4R/(1-R)^2$ can be determined from the indices of refraction inside $(n_2)$ and outside $(n_1)$ the resonator with the reflection at the boundaries given by $R = (n_1 - n_2)^2/(n_1 + n_2)^2$ at normal incidence. $I_\omega(d)$ is a periodic function with maximum coupling into the cavity occurring for values of $d$ equal to an integer number of half-wavelengths, i.e.,$d = m(\lambda_\omega/2n_2)$ with $m = 1, 2, 3$, etc. Depicted in Figure 5.3B is $I_\omega(d)$ obtained with $n_1 = 1.0$ (air), $n_2 = 2.3$ (ZnO), and $\lambda_\omega = 746$ nm. The intensity stored in the

cavity exhibits a series of broad resonances spaced at multiples of 162 nm. The widths of the resonances are a result of the low reflectivity at the interfaces (~15%). It is the periodic nature of $I_\omega(d)$ combined with a varying facet separation along the rod axis that is the qualitative origin of the second harmonic generated images.

We have taken this qualitative idea one step further and used the resonance function, $I_\omega(d)$ shown in Figure 5.3B to simulate the second-harmonic patterns observed in our images. Displayed in panels D and E of Figure 5.3 are the SHG and SEM images of a 9 μm long ZnO rod. The procedure involves first using the SEM image to measure the diameter of the rod, $d_r$ (Figure 5.3F) as a function of distance along the rod axis. The facet separation is then estimated from the diameter assuming that the cross section is a perfect hexagon $d_{FP} = 3^{1/2} d_r/2$ the result is displayed in Figure 5.3A. The SHG intensity along the rod axis is obtained by mapping the square of the intensity values ($I_{2\omega} = I_\omega^2$) in Figure 5.3B onto the facet separation in Figure 5.3A. Since the plane-parallel plates of the hexagon do not extend toward infinity but only span the length of a facet ($s$ Figure 5.3F), the spatial intensity variation perpendicular to the rod axis is approximated as a Gaussian with a full width at half-maximum of $s$. The result is a matrix of intensity values displayed in Figure 5.3C. Despite the simplicity of the model the simulated image is in remarkable agreement with the experimental image. The relatively minor differences between the experimental and simulated images may be due to an uncertainty in the refractive index for ZnO since a range of values between 2.2 and 2.4 have been reported for the wavelengths of interest,[63] or they reflect an imperfect hexagonal cross section (i.e., not all facets are of equal length implying $d_{FP} = 3^{1/2} d_r/2$ is only approximate). Furthermore, the simulation models the needle-like structure of the rod as a series of hexagonal slabs calculating the energy stored in the cavity

assuming the facets are parallel and using that to determine the intensity of the second-harmonic. The facets are not quite parallel, and in this respect our model is only approximate. The tapered shape introduces walk-off that would decrease the finesse of the cavity relative to the parallel geometry assumed in the model. Since ZnO has low reflectivity at the interfaces (~15%), it already has a low finesse and walk-off would just reduce this further. Despite this limitation, the similarity between the simulated and experimental images suggests that the additional reduction in the cavity finesse introduced by nonparallel facets is a relatively minor effect.

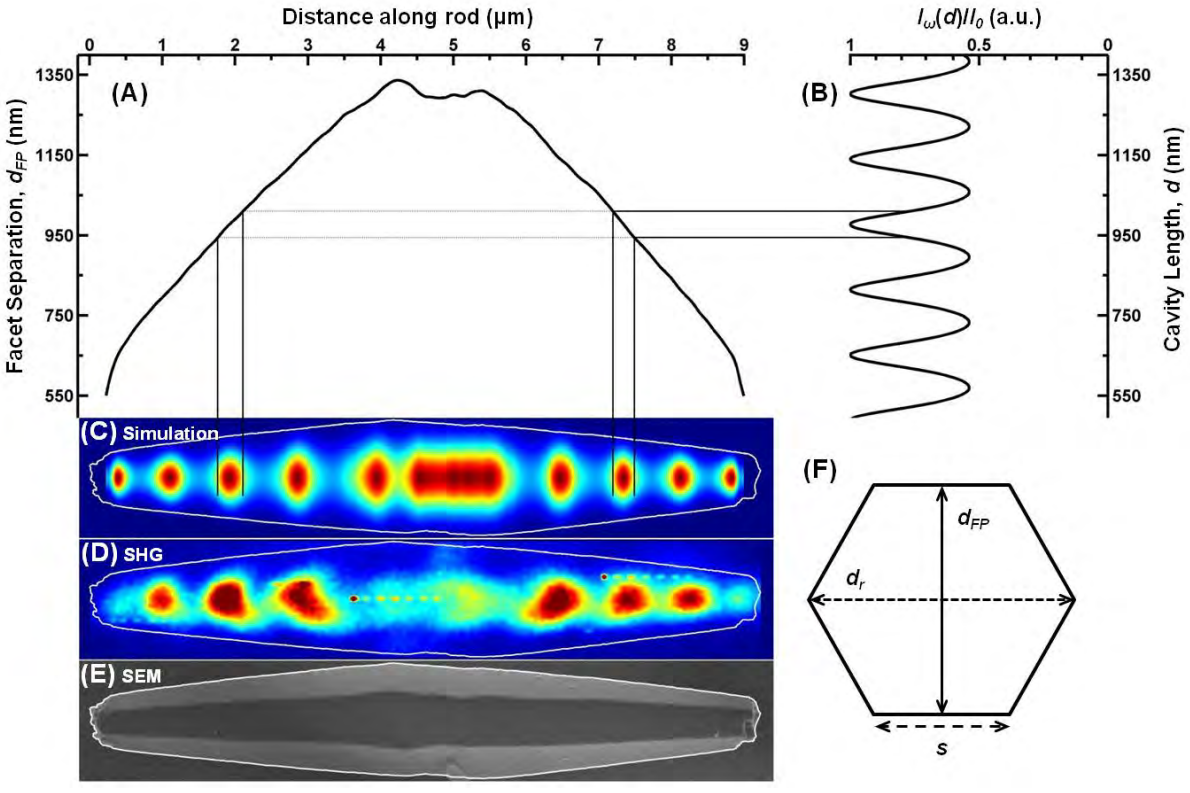


**Figure 5.3:** Cavity mode analysis of the second harmonic images. (A) A plot of facet separation ($d_{FP}$) as a function of distance along the rod axis measured form the SEM image of the needle-like ZnO rod shown in panel (E). (B) Intensity of the fundamental ($I_\omega$) stored inside a Fabry-Pérot resonator as a function of cavity length. Obtained using Eq. 5.1 with $n_1 = 1.0$ (air), $n_2 = 2.3$ (ZnO) and $\lambda_\omega = 746$ nm. The intensity stored in the cavity exhibits

a series of broad resonances spaced at multiples of 162 nm. The widths of the resonances are a result of the low reflectivity at the interfaces (~15%). The solid lines represent the FWHM ($I_\omega$) of integer $m = 6$ half-wavelengths which fit inside the resonator. (C) Simulated second-harmonic generated microscopy image using (A) and (B). (D) Experimentally collected second-harmonic generated microscopy image. (E) Scanning electron microscopy image of a needle-like ZnO rod used to generate (A). (F) Illustration of the hexagonal cross section of a ZnO rod with facet separation ($d_{FP}$), diameter ($d_r$), and facet length ($s$).

The resonance condition ($d = m(\lambda_\omega/2n_2)$) predicts that for a given mode number ($m$), the resonant cavity length will increase linearly with the fundamental wavelength. Figure 5.4 displays a series of SHG images collected over a range of excitation wavelengths. The images obtained from 726 to 750 nm ($\lambda_{2\omega} = 363 - 375$ nm) are relatively similar, each displaying the clear periodic pattern that was also present in Figure 5.2B. Inspection of multiple rods confirms that in general each resonance spot moves toward the midpoint of the rod (in the direction of larger $d_{FP}$) as $\lambda_\omega$ is tuned to the red. This general trend is apparent in Figure 5.5, which represents data obtained from four different rods. The figure shows the facet separation ($d_{FP}$) at three SHG resonances, which correspond to $m = 5, 6, 7$ standing wave modes, as a function of excitation wavelength. The shaded areas depict the resonant cavity lengths predicted by $d = m(\lambda_\omega/2n_2)$ for $n_2$ between 2.2 and 2.4.

The absence of the same modulation in the two-photon emission images (Figure 5.2C, D) indicates that the physical origin of the pattern is not simply a consequence of the spatial variation in light intensity along the rod due to the coupling of fundamental optical field into the Fabry-Pérot modes of the ZnO resonator. The pattern instead stems from the standing wave that is created between the two parallel facets. This standing wave, which can be thought of as a superposition of two propagating waves traveling in opposite directions, in

turn produces a second-order polarization wave with zero phase velocity that extends throughout the rod. The standing-wave nature of this polarization leads to the generation of second-harmonic photons that propagate in both forward and back directions. The back scattered second-harmonic is not produced in bulk ZnO and is a direct consequence of second-harmonic generation in an optical resonator. When the near-infrared photon energy is larger than half the ZnO band gap, the second-harmonic will likely travel only 100 nm before it is reabsorbed by the ZnO. Under these conditions it is unlikely that the second-harmonic couples into a resonator mode. It is the nonlinear polarization standing wave that is responsible for the observed enhanced back scattered SHG; when the facet separation is such that the fundamental is off resonance, the standing wave is not formed and the back scattered second-harmonic generation is suppressed.

Excitation above the ZnO band gap (726-750 nm) results in SHG images that are dominated by the standing wave pattern with the most intense second-harmonic along the center of the rod. When the fundamental wavelength is tuned below the band gap, from 750 to 810 nm, a qualitatively different SHG behavior is observed (Figure 5.4). At the lowest energies ($\lambda_\omega = 775 - 810$ nm) the second-harmonic intensity shifts to the outside of the rod to coincide with the rod vertices and angled facets giving rise to a complicated intensity pattern. The images obtained at intermediate excitation wavelengths (755 and 762 nm) appear to be a combination of these two extremes. The origin of this shift is not entirely clear but may reflect a competition between different types of cavity modes supported by the rod cross section.

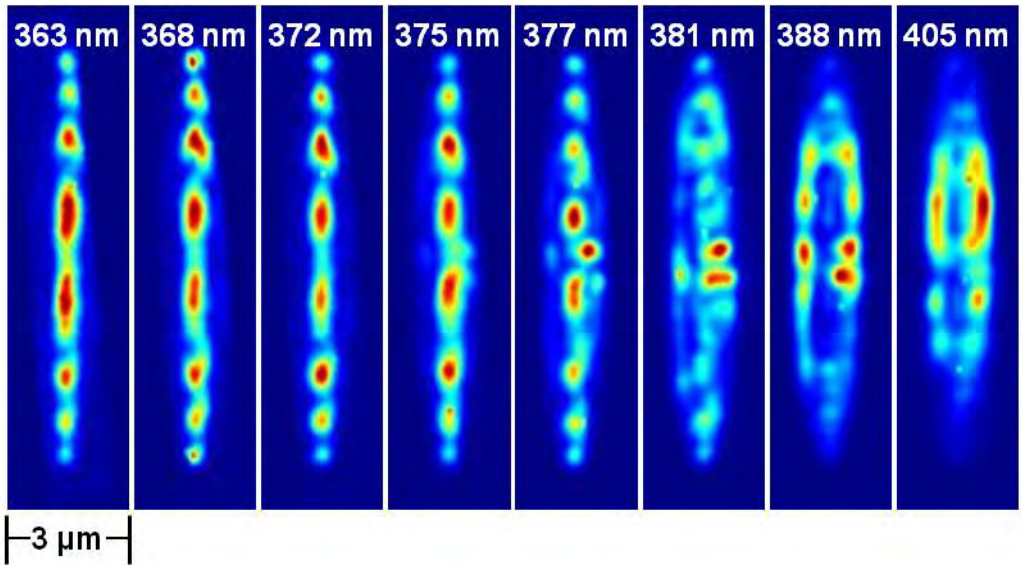


**Figure 5.4:** Second-harmonic images as a function of excitation wavelength. An array of second-harmonic generation microscopy images of a needle-like ZnO rod after photoexcitation over a range of fundamental wavelengths (726-810 nm). The images show periodic areas of enhanced SHG intensity. The SHG intensity pattern qualitatively changes around 377 nm, correlating with excitations falling below the band gap. Each SHG image is scaled individually, masking the variation in the absolute intensity that is observed across this range. In particular, as the second-harmonic photon energy in tuned toward the exciton resonance (380 nm), we observe an increase in the SHG efficiency due to resonance enhancement.

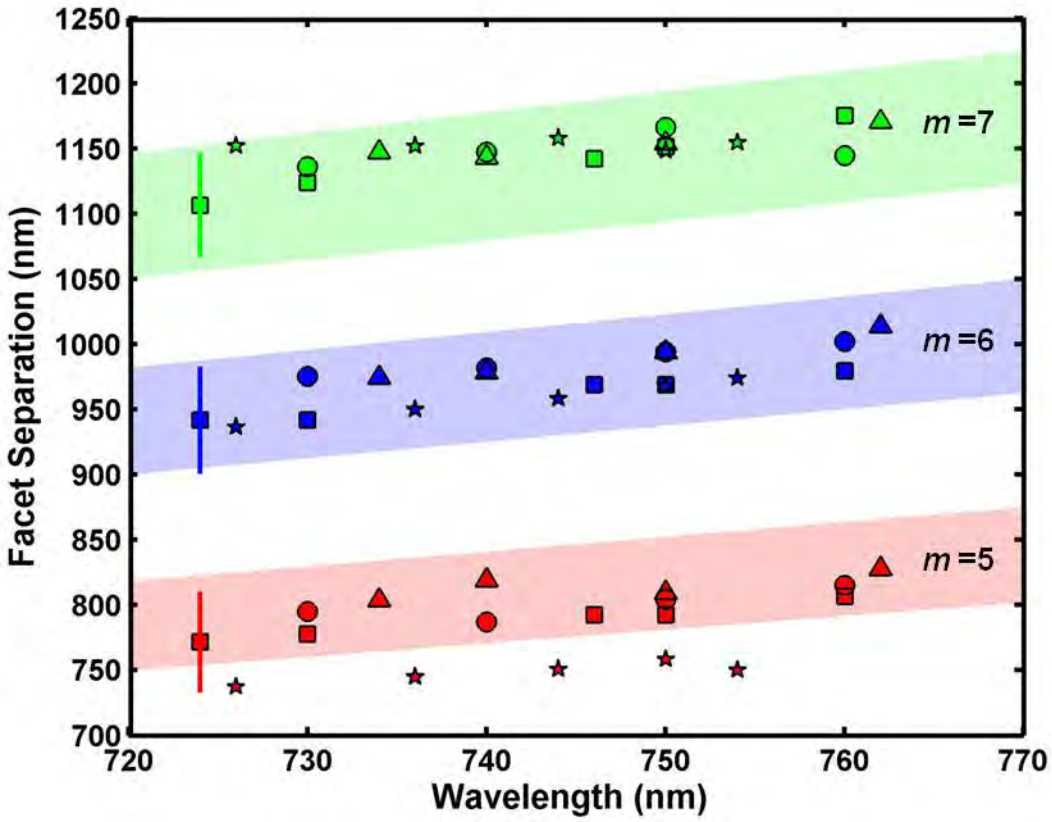


**Figure 5.5:** Facet separation measured from the SEM image at the positions of the $m = 5, 6, 7$ SHG resonances for a series of different laser excitation wavelengths. The figure is a compilation of data from four different needle-like ZnO rods (▲,■,★,●). The error bars represent the average uncertainty associated with measuring the facet separation. The shaded regions highlight the resonance conditions, $d = m(\lambda_\omega / 2n_2)$ for $m = 5, 6, 7$, with $n_2$ between 2.2 and 2.4.

While a Fabry-Pérot cavity is the simplest cavity that could be formed inside a hexagon cross section, it is not the only one available. Whispering gallery modes (WGM) correspond to the circulation of light around the perimeter of the rod due to total internal reflection off each of the six facets, resulting in larger *Q*-factors when compared to standing wave Fabry-Pérot modes, where the reflectivity is only ~15%. The main cavity loss for WGM occurs at the vertices,[88] which is in qualitative agreement with the increased SHG

intensity observed at the edges of the facets. The primary evidence for the presence of these modes in ZnO structures has come from modulation in their emission spectra,[77-79,81,86,87] with far fewer observations resulting from direct imaging. One recent exception to this is the report of periodic modulation in SHG images of ZnO tetrapods,[89] consistent with our results; however, the resolution of those images precluded the direct observation of preferential emission from the vertices and the assignment was made on the basis of geometrical arguments. The competition between the WGM and Fabry-Pérot modes may stem from the reabsorption of the second harmonic at the blue end of the excitation range, giving rise to a path-length-dependent loss that would favor the shorter Fabry-Pérot cavity. We are currently employing the finite difference time-domain (FDTD) method,[90] using a freely available software package,[91] to further explore this competition.

## 5.5. CONCLUSION

Spatial imaging of single needle-shaped ZnO structures using second-harmonic generation microscopy exhibit cavity-enhanced second-order mixing. Images obtained from individual structures show areas of enhanced second-harmonic intensity along the longitudinal axis of the rod that are periodically distributed and symmetrically situated relative to the rod midpoint while both band edge and trap state emissions do not. It is the periodic nature of the intensity of the fundamental contained inside the cavity combined with a varying facet separation along the rod axis that is the qualitative origin of the second-harmonic generated images. The spatial modulation is a direct consequence of the fundamental optical field coupling into standing wave resonator modes of the ZnO structure, leading to an enhanced backscattered second-harmonic condition that cannot be achieved in

bulk ZnO. As the fundamental wavelength is tuned below the band gap, a qualitative change in the SHG image is observed. The complicated image is most likely due to the competition between Fabry-Pérot and whispering gallery modes.

# CHAPTER 6. SPATIALLY DEPENDENT DYNAMICS IN ZNO RODS OBSERVED BY FEMTOSECOND PUMP-PROBE MICROSCOPY

## 6.1. INTRODUCTION

The polydispersity intrinsic to nanoscale and microscale semiconductor materials poses a major challenge to using individual objects as building blocks for device applications. Early work showed that surfaces, which trap mobile carriers, result in band bending and internal electric fields that give rise to significant variation in the electronic and photophysical behavior from one object to the next. Modern nanomaterials have moved beyond simple particles, and the complex geometrical architectures that are available (e.g., needles, ribbons, tetrapods) have both expanded the range of potential applications and raised new questions regarding the connection between shape and function.[61] This report addresses a fairly simple one: Can different locations within a single structure exhibit different dynamical signatures? Do the ends of a rod behave differently than the middle? Spatial differences can arise from a variety of physical sources and mechanisms. Carrier confinement in the sharp features of high-aspect structures and variation in defect density are two examples. Both would influence carrier relaxation and could result in behavior that differs from one location to another. While such effects are easy to envision, experimental observation requires techniques with combined spatial and temporal resolution.

The pursuit of such methods is not new, and time-resolved optical microscopies have been applied to the study of a wide variety of problems. The most common are luminescence-based approaches, which are the simplest to implement but are limited to the study of phenomena on the picosecond time scale.[21] Pump-probe methods can follow dynamics on faster time scales; however, incorporation into microscopy is more difficult, and far fewer examples exist. While near-field and scanning probe microscopies offer the greatest spatial resolution, their combination with pump-probe methods significantly

increases the experimental complexity.[92-94] In this respect, far-field methods are more attractive, and a few examples have begun to appear on a variety of systems and materials.[95-101] While several studies of carrier dynamics in semiconductor particles achieved femtosecond time resolution, their spatial resolution was lower than the diffraction limit, and the excitation of whole structures generated carriers throughout the object.[96,98,100,101]

Exposing dynamical differences from point to point requires localized excitation with high lateral resolution. Spatially localized excitation in pump-probe microscopy has been reported in just a few cases, including the study of graphene sheets,[99] semiconductor nanowires,[95] molecular crystals,[97] and composite materials.[102-104] The greatest spatial variation was observed in composites, which stemmed from distinct chemical domains, while the nanomaterials exhibited only slight differences from one point to the next. Here, we combine pump-probe methods with far-field microscopy to study the spatial variation of the electron-hole (e-h) recombination dynamics in needle-shaped ZnO rods on a femtosecond time scale with high lateral resolution (350 nm). Time-resolved images show significant variation in the dynamical response, with the ends of the rods exhibiting dramatically faster e-h recombination than at points in the interior.

The ability to manipulate the shape of ZnO structures is enormous, and through a variety of synthetic methods, many different structural forms have been demonstrated, making it an ideal material for studying shape-dependent phenomena. The rods used in this work were grown using solution-based methods by incubating a 0.05 M solution of $Zn(NO_3)_2$ and methenamine ($(CH_2)_6N_4$) under hydrothermal conditions for 3 h at 150 °C.[83] The resulting structures were sonicated in ethanol to disperse aggregates, drop-cast onto a microscope slide, and then annealed at 550 °C to reduce the overall defect density.[105]

## 6.2. EXPERIMENTAL

Photoexcitation of ZnO by a single UV photon (or simultaneous two-photon excitation in the near-infrared) promotes electrons from the valence band to the conduction band, resulting in free charge carriers (Figure 6.1A). These free carriers can either associate into excitons that lie just below the conduction band edge or become trapped at defect sites in the crystal lattice. Exciton recombination results in a UV-blue emission that is centered at 390 nm, while defect emission gives rise to a broad visible emission band centered at 550 nm.[63]

A schematic diagram of the nonlinear microscope used in this work is displayed in Figure 6.2. Individual rods are excited by a 730 nm femtosecond laser pulse (1 nJ/pulse) generated by the frequency-doubled output of an optical parametric oscillator (OPO). The excitation pulse is focused to a diffraction-limited spot by a microscope objective, resulting in a two-photon absorption that creates charge carriers in a localized region of the structure. On the basis of the magnitude of the two-photon cross section,[106] we estimate that the pump pulse produces$\sim 10^{21}$ carriers/cm$^3$. Emission is then collected in the backward-scattered direction by the objective and focused onto the slit of a scanning monochromator and photomultiplier tube. Two-photon emission imaging is achieved by raster scanning the sample across the focal point of the objective with a piezoelectric nano-positioning stage. The spatial resolution of the two-photon microscope is determined by the size of the laser spot at the focus of the objective. Because two-photon absorption scales with the square of the optical intensity, efficient excitation occurs only at the focus, resulting in confocal-like behavior and a lateral excitation dimension that is smaller than the diffraction limit. For our microscope, the spatial extent of the excitation is approximately 350 nm.

Shown in Figure 6.1B is the scanning electron microscopy (SEM) image of a typical rod used in this work. The structures vary in length from 15 to 20 μm and have faceted hexagonal cross sections with tapered ends (Figure 6.1B). We have developed the protocols for locating objects found in the SEM in the optical microscope, which enable us to correlate the photophysical observations with detailed structural information. The two-photon emission image shown in Figure 6.1C depicts the 390 nm band-edge emission from the same rod. The image shows significant variation in the intensity across the structure, with the most prominent features being bright emission from the rod ends and enhanced emission along the vertices and outer facets. The modulated intensity within the interior of the rod is attributed to the influence of Fabry-Pérot and whispering gallery cavity modes supported within the hexagonal cross section of the rod that concentrate the optical field at certain points within the structure.[62,78,107]

Spectroscopic measurements are performed by positioning the excitation spot at specific points. Photoluminescence spectra obtained at two different locations (Figure 6.1D) show both the characteristic narrow exciton and broad trap emission bands. The relative intensities of the two emission bands vary across the structure, with the end showing a more intense band-edge emission that suggests a greater propensity for e-h recombination across the band gap at that location.

Transient absorption microscopy incorporates a second laser pulse (810 nm, 50 pJ) focused onto the position of the excitation spot by the objective (Figure 6.2). The probe beam is collected by a condenser lens and focused onto the entrance slit of a monochromator and detected by a photomultiplier tube. A long-pass filter placed before the monochromator rejects unwanted pump light. An optical chopper modulates the excitation beam at 4 kHz,

and pump-induced changes in the intensity of the probe pulse are monitored by a digital lock-in amplifier. The pump and probe polarizations were parallel to each other and oriented perpendicular to the long axis of the rod. The time resolution of the microscope is ~ 500 fs.

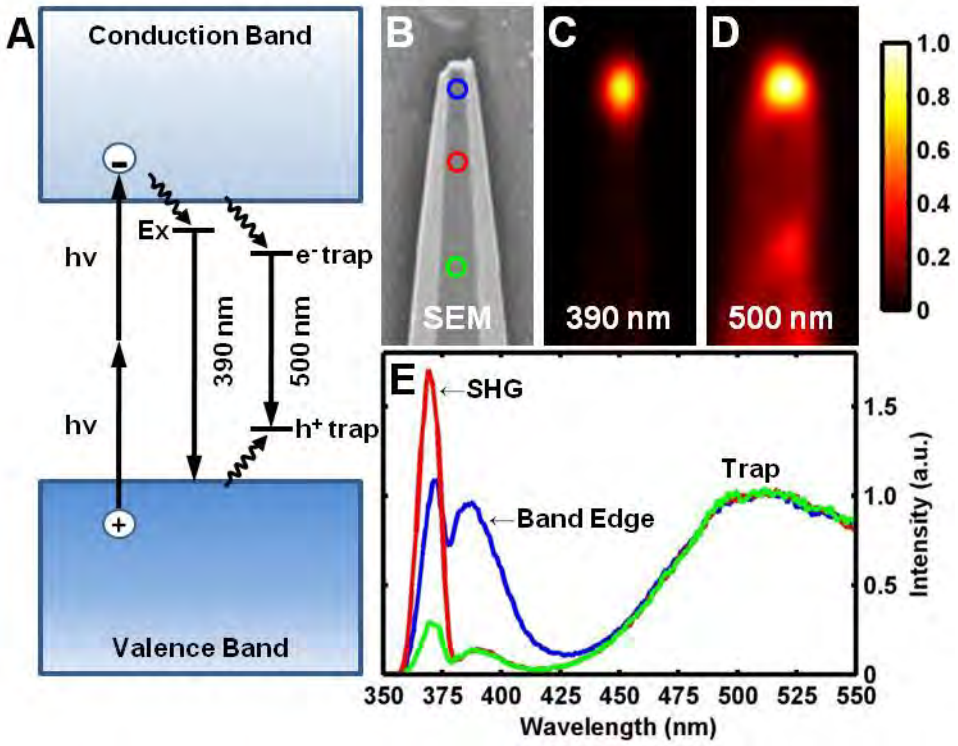


**Figure 6.1:** (A) Illustration of ZnO band structure depicting two-photon excitation, band-edge emission at 390 nm from an exciton state (EX), and trap-mediated emission at 500 nm. (B) SEM image of a typical structure; circles indicate locations of spectroscopic measurements. (C) Band-edge emission image obtained by raster scanning the focused excitation laser across the rod. (D) Emission spectra observed at a point near the end of the rod (blue circle in (B)) and within the interior (red and green circle (B)). Spectra show the band-edge, trap emission and second-harmonic generation.

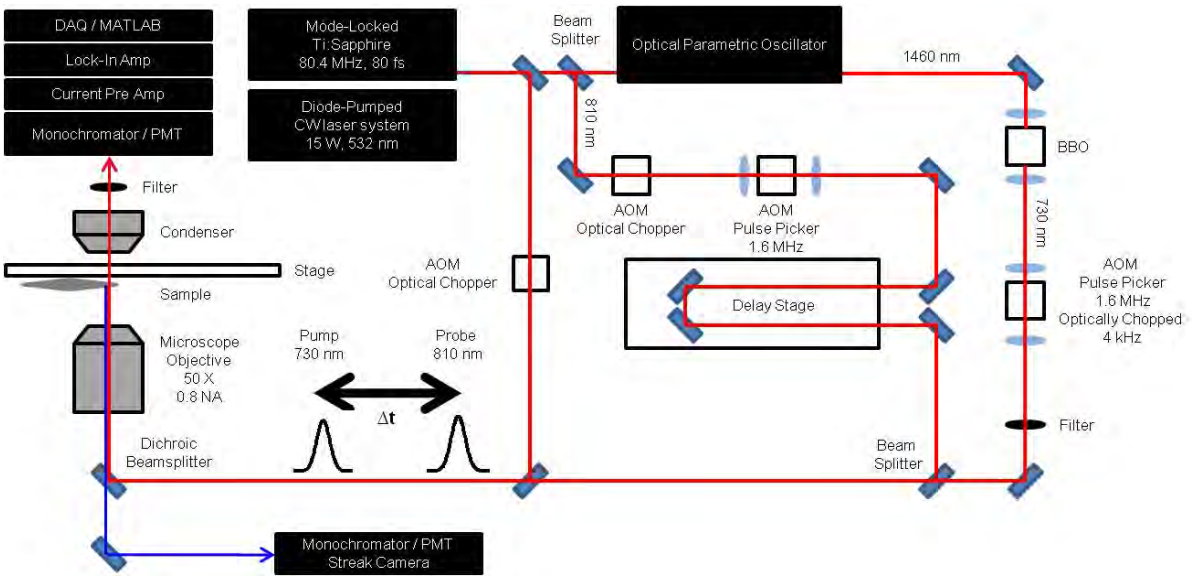


**Figure 6.2:** Schematic diagram of a two-photon pump-probe microscope. The frequency-doubled output of an optical parametric oscillator (OPO) at 730 nm is directed on the back aperture of the microscope objective and focused to a diffraction-limited spot at the sample. Imaging is achieved by raster scanning the sample stage across the focused laser spot and monitoring the emission collected by the objective. The lateral resolution is approximately 350 nm. Pump-probe microscopy incorporates a second laser beam focused onto the location of the excitation beam. The beam that emerges from the sample is collected by a condenser lens, and its intensity is monitored by lock-in detection. Two acousto-optic modulators (AOM) are used to reduce the repetition rate of the laser to 1.6 MHz. Time-resolved emission measurements are performed by monitoring the emission intensity using a streak camera.

## 6.3. ORIGIN OF PUMP-PROBE SIGNAL

The pump-probe signals include contributions from an induced absorption arising from near-infrared excitation of free-carriers or electrons in shallow traps[108], and a Kerr lensing component originating from a spatial variation in the index of refraction due to the localized charge carrier distribution produced by excitation.[93,106,109,110] The magnitude of both contributions depends upon the presence of free carriers, and the decay of the pump-

probe signal is attributed to a decrease in their concentration as a result of recombination and trapping events. While an induced absorption always produces a decrease in probe transmission the Kerr lensing component may provide either an increase or decrease in signal.

The sign of the Kerr contribution is strongly coupled to the relative overlap between the pump and probe beams along the c-axis of the structure. In traditional pump-probe experiments the volume of the probe beam is smaller than the pump, ensuring that the probe beam only monitors a small portion of the pump's excitation volume. Unfortunately, in a two-photon excitation, one-photon probe experiment the probe's volume is much larger than the pump's, this allows for some flexibility in relative overlap between the pair of pulses. Plotted in Figure 6.3A are normalized pump-induced signals as a function of pump-probe separation, $d_{pps}$ measured along the c-axis and y-axis (⊥ c-axis). These measurements were performed by fixing the probe at a site located within the interior of the structure while the pump beam was scanned along a chosen axis. An approximate 1 ps time delay was placed between the pump and probe pulses. A pump-probe separation, $d_{pps} = 0$ along the c-axis and y-axis are arbitrarily set at the inflection point and absolute maximum respectively. Complications in determining the absolute zero separation arises from the difference in excitation and probing volumes. In the current experimental setup the two-photon absorption volume is approximately half of the diffraction limited probe volume. Generally collinear beams with good spatial overlap are achieved by aligning transmission images produced from the pump and probe beams separately. It has been observed that the largest sum-frequency signals generated from the pump and probe beams do not always correlate to the

best collinear spatial overlap. The error associated with our current overlapping procedure is on the order of ± 100 nm along the c and y axes.

When the pump beam is scanned along the c-axis of the rod in proximity to the probe, the pump-induced signal takes on a derivative line shape. Scanning from a negative to positive separation at location #1 (Figure 6.3A), the signal goes from a pump-induced increase (positive signal) to decrease (negative signal) in probe transmission. In comparison to location #2 (Figure 6.3A), the contours of the pump-induced signal are inverted. When the probe beam is scanned along the y-axis at location #1 (Figure 6.3A) the pump-induced signal is absent of any change in sign. However, the sign of the y-axis scan is determined by the pump-probe separation along the c-axis. The y-axis scan displayed in Figure 6.3A was performed with a c-axis $d_{pps} = 0.4$ μm. A similar but inverted (positive) signal is observed when the c-axis $d_{pps} < 0$ (not shown).

The magnitudes of the signals decay to zero as the overlap decreases and the separation increases between the pump and probe beams. The $d_{pps}$ waist of the y-axis scan (FWHM) is comparable to the separation of extrema for the c-axis scans, approximately 700 nm. The focused gaussian waist (FWHM) of the probe beam is calculated to be 640 nm. The similarity between these values suggests that the pump-induced signals are only observed when the pump and probe beams are overlapped at early delay times. Based on the carrier diffusion constant in ZnO (~10 $cm^2$ $s^{-1}$),[29,30] we estimate a field-free diffusion length of ≈ 30 nm during the first 1 ps after excitation. Consequently, we ignore any diffusion based effects in these pump-scanned fixed-probed traces.

A comparative scan is also applied in the z-direction and is displayed in Figure 6.3B. This z-scan does not examine the separation of the pump-probe beams but varies the focus of

the objective relative to the sample. Negative and positive depths correspond to the focus arriving before and after the sample respectively. Similar to the y-axis scan no derivative line shape is observed where once again the sign of the signal is dependent on the c-axis separation. At location #1 and a c-axis $d_{pps} < 0$ the signal is positive where as when the c-axis $d_{pps} > 0$ the signal is negative. A summary of the c-axis separation and corresponding signs of the signals are displayed in Table 6.1.

| | Location #1 | | Location #2 | |
|---|---|---|---|---|
| | c-axis $d_{pps} < 0$ | c-axis $d_{pps} > 0$ | c-axis $d_{pps} < 0$ | c-axis $d_{pps} > 0$ |
| c-axis scan | + | - | - | + |
| y-axis scan | + | - | - | + |
| z-axis scan | + | - | - | + |

Additionally, pump-induced images were collected at c-axis $d_{pps} < 0$ and $d_{pps} > 0$ (Figure 6.3C). Both images contain an inflection in sign that occurs near the middle of the rod. At a c-axis $d_{pps} < 0$ in accordance with Figure 6.3C and the top of Figure 6.3A the probe pulse is closer to the left end when compared to the pump. Experimentally this corresponds to a positive left half and negative right half image. In opposition at a c-axis separation $d_{pps} > 0$ the probe pulse is closer to the right end when compared to the pump and the left half of the image is negative while the right half is positive.

The shapes of the signals displayed in these pump-scanned fixed-probe traces are similar to those measured through traditional z-scan methods used to investigate optical nonlinearities.[111] z-scan methods measure the amount of transmitted light collected through

an aperture in the far-field after propagation through a focusing lens and subsequent sample. The amount of light collected is monitored as a function of sample location relative to the focal length of the lens. The derivative line shapes are a consequence of the nonlinear index of refraction in combination with an aperture displayed in the far-field. In reference to our axis-scanned experiments, the separation of the beams along the c-axis suggests that an analogous combination of nonlinear index of refraction in conjunction with an intrinsic aperture exists within the rod that is not present in y and z-axis scans. Consequently, the sign of the Kerr component is directly related to the relative spatial separation of the pump and probe beams along the c-axis.

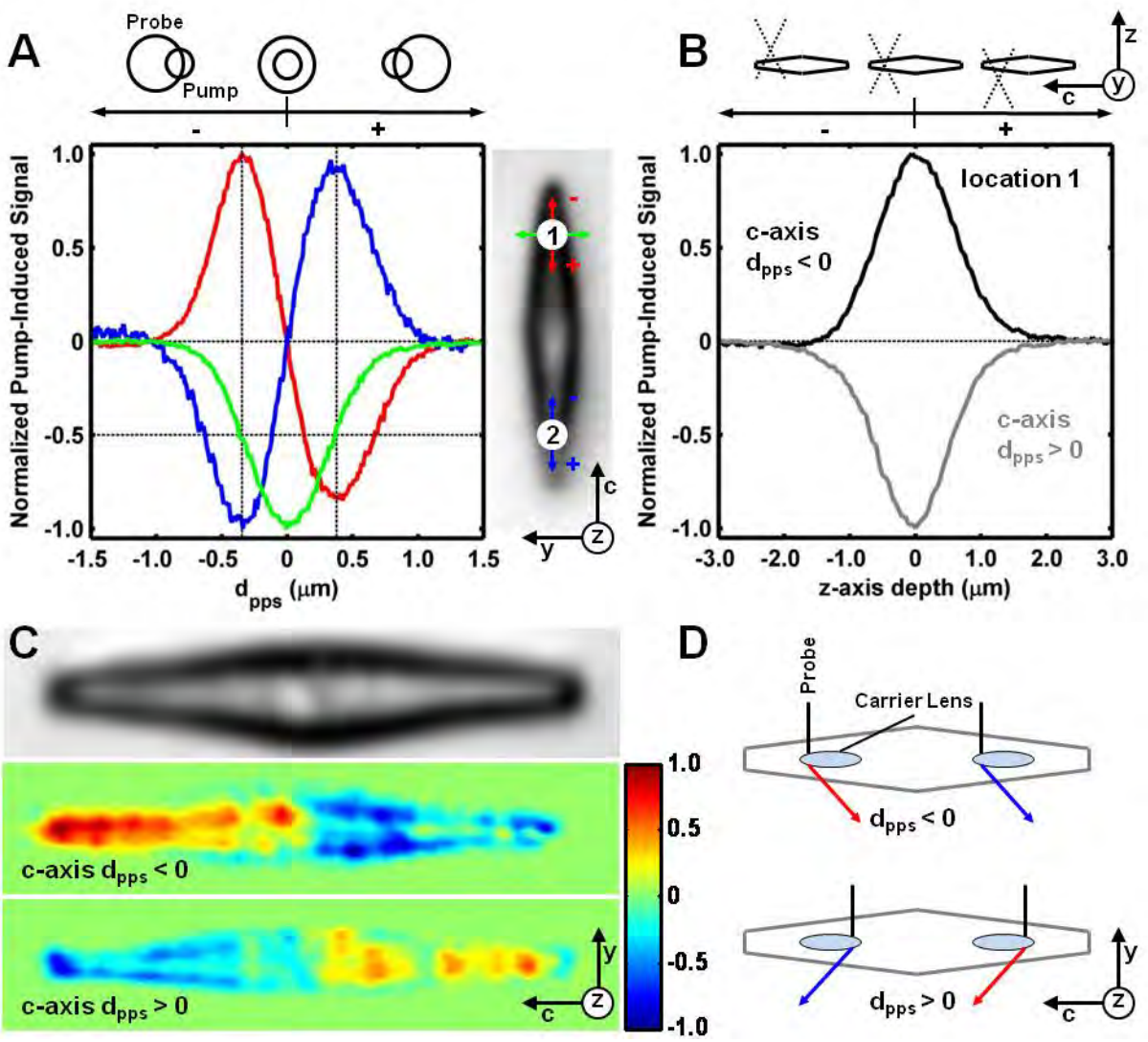


**Figure 6.3:** (A) Normalized pump-induced signals as a function of pump-probe separation along the c-axis (location #1: red; location #2: blue) and y-axis (location #1: green, c-axis $d_{pps} = 0.4$ μm). Black dotted lines indicate the intersection of y-axis scan signal at FWHM and extrema separation from c-axis scans. To the right of the plot are the spatial locations along with the color-coded scanned axes overlaid on top of the brightfield image of the ZnO structure. Above is a schematic overlap of the pump and probe beams as a function of separation. (B) Normalized pump-induced signals as a function of scanned depth along the z-axis at a c-axis $d_{pps} < 0$ (black) and $d_{pps} > 0$ (gray) at location #1 in (A). Above is a schematic diagram of the focus relative to the focus of depth within the structure. (C) Brightfield image along with two normalized pump-induced images at a c-axis $d_{pps} < 0$ and

$d_{pps} > 0$. (D) Cartoon of pump-induced carrier lens and subsequent and geometric ray trace of probe beam for a given c-axis separation. Probe propagation through the lens is deviated towards the center or ends of the rod depending on the c-axis separation. Refraction towards the center (end) of the rod corresponding to a positive (negative) signal and is displayed in red (blue).

Given that the excitation pulse assumes a spatial intensity distribution a corresponding distribution in refractive index change is also produced. In turn, the two-photon absorption generates a lens whose decay is proportional to the recombination of charge carriers. Considering now the spatial separation along the c-axis when the probe beam is in between one end of the rod and the pump beam the transient lens shifts the direction of the probe towards the end of the rod and less light is collected. However when the pump beam is in between one end of the rod and the pump beam the transient lens shifts the direction of the probe towards the middle of the rod and more light is collected. The narrowing of the rod diameter acts as an aperture to reduce the transmission of the probe while the larger cross-sections allow for more light to be collected.

The variation in sign can be described by considering a Kerr transient lensing contribution to the pump-induced signal. At high irradiances the index of refraction is intensity dependent where the change in refractive index, $\Delta n$ is given by two terms:

$$\Delta n = \gamma I + \sigma_r N \qquad (6.1)$$

an electronic component, where $\gamma$ is the bound-electron nonlinear refractive index and a free carrier component, where $\sigma_r$ is the change in the index of refraction per unit photoexcited charge-carrier density *N*. In the absence of one-photon absorption the carrier density is given by the following,

$$\frac{dN}{dt} = \frac{\beta I^2}{\hbar\omega} \tag{6.2}$$

where $\beta$ is the two-photon absorption coefficient, $I$ is the intensity, and $\omega$ is the angular frequency. Consequently, the change in refractive index due to the absorption of free carriers is proportional to the time integral of $I^2$. The electronic component will be dominant at low irradiance levels, whereas the free carrier component will dominate at high irradiance levels. For low linear absorption the carrier density may be approximated by the following,[106,111]

$$N = \frac{0.23\beta t_0 I^2}{\hbar\omega} \tag{6.3}$$

where $t_0$ is the pulse duration of the excitation. For $\beta = 718\,\mathrm{cm/GW}$ @ $730\,\mathrm{nm}$ [106], $t_0 = 100\,\mathrm{fs}$, and $I = 100\,\mathrm{GW/cm^2}$, Approximately $N = 10^{21}\,\mathrm{carriers/cm^3}$ are produced experimentally which suggests that the generation of free carriers strongly influences the nonlinear index of refraction. Values for the bound-electron and free carrier nonlinear refractive index have been previously calculated through traditional z-scan measurements; $\gamma = 2.26 \times 10^{-11}\,\mathrm{cm^2/W}$ and $\sigma_r = 9.28 \times 10^{-20}\,\mathrm{cm^3}$.[106] At the experimental intensity and initial carriers generated here, it is approximated that the free carrier contribution to the nonlinear refractive index is on the order of 40 times greater than the bound-electron component.

Displayed in Figure 6.4 are pump-scanned fixed-probe traces at several pump-probe delays at a location within the interior of a rod. The transient absorption signal contains a derivative line shape which decays as the pump-probe delay is increased. The fact that the derivative line shape decays and is not simply an instantaneous response supports the idea that the electronic component of the nonlinear index of refraction is relatively weak and the change in index of refraction is dominated by the generation of free carriers, and the decay of

the pump-probe signal is attributed to a decrease in their concentration as a result of recombination and trapping events. Further, both peaks decay with roughly the same rate. Consequently, the dynamics do not depend on the sign of the signal.

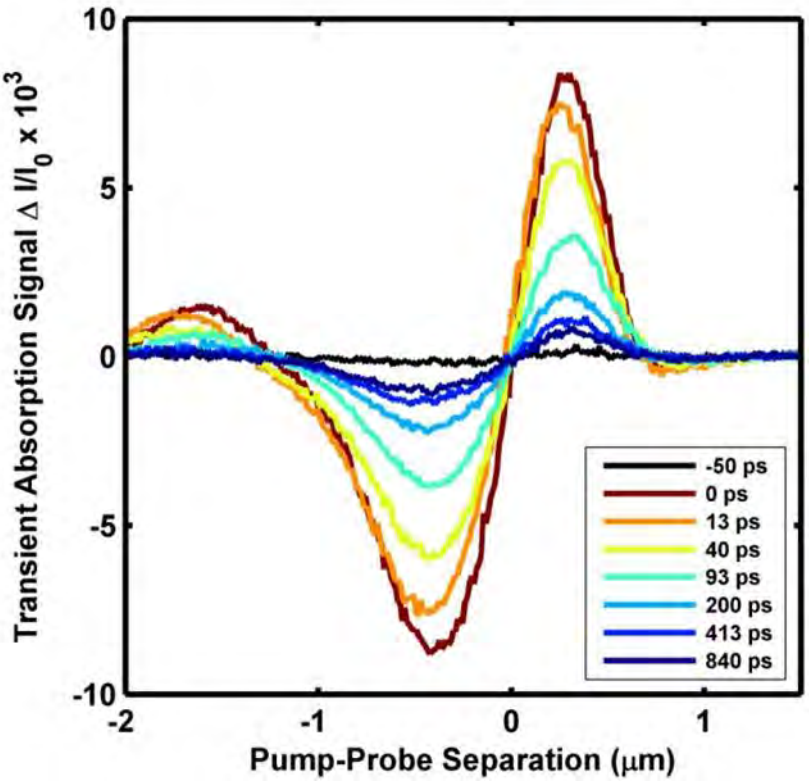


**Figure 6.4:** Transient absorption signal as a function of pump-probe separation along the c-axis for a series of pump-probe delays.

It is important to reiterate that the pump-probe signals include contributions from an induced absorption arising from near-infrared excitation of free-carriers or electrons in shallow traps, and a Kerr lensing component originating from a spatial variation in the index of refraction due to the localized charge carrier distribution produced by excitation. While, the relative amount that each component contributes is difficult to quantize, the Kerr lensing component appears to have less of an effect within the middle of the rod. c-axis pump-scanned fixed-probe traces were collected at a series of locations along the c-axis of the rod

(Figure 6.5). For locations near the top end of the rod (locations #1, #2, & #3) the pump-induced signals contain a derivative like shape that is analogous to the signal displayed in Figure 6.3 location #1. As the scan location approaches the middle of the rod the magnitude of the positive portion is reduced and the negative section is increased, shifting the pump-probe separation at which the signal switches signs. At the middle of the rod (locations #4, #5, & #6) the positive contribution is only observed in location #4 while no positive contribution is observed at locations #5 and #6. The FWHM of location #5 is approximately 700 nm the same value observed in Figure 6.3A. As the scan location is further moved towards the bottom end (locations #7, #8, & #9) the signs are opposite of to the scans at the top of the rod analogous to Figure 6.3A location #2. The pump-induced decrease in probe intensity during a c-axis scan near the middle of the rod has the smallest Kerr lensing component due to the large size and minimal taper. Therefore, the pump-induced decrease in probe intensity during a c-axis scan near the middle of the rod is a relative measure of the near infrared absorption component where an induced absorption always produces a decrease in probe transmission.

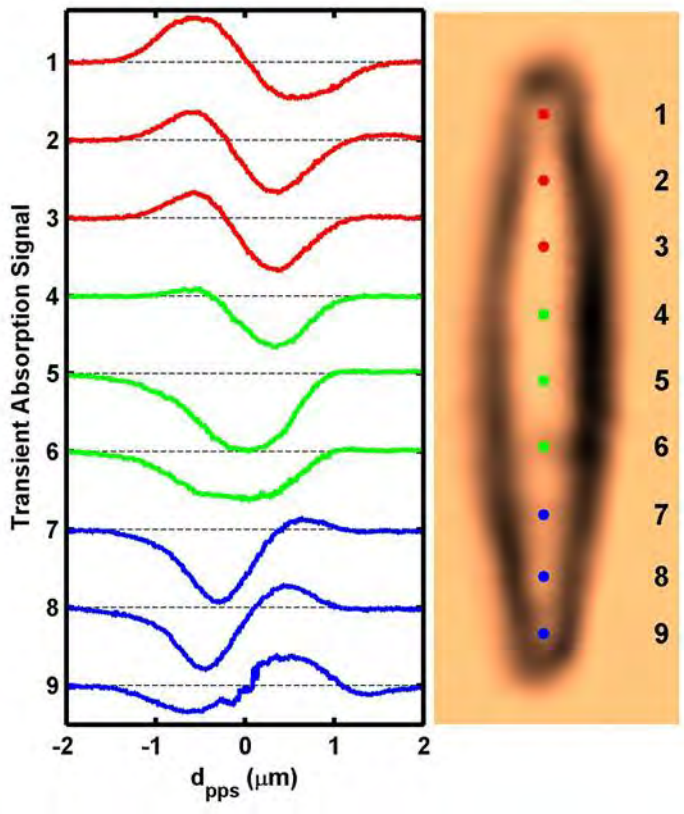


**Figure 6.5:** (Left) Transient absorption signal vs. pump-probe separation at nine different locations. (Right) Transmission image at 810 nm with nine different locations depicting position of c-axis scans.

## 6.4. PUMP-PROBE MICROSCOPY

Pump-probe microscopy data are shown in Figure 6.6 for three different rods, denoted **R1**, **R2** and **R3**. Transient absorption $\Delta I/I$ data for three different points in each rod are displayed (Figure 6.6A), and colored circles on the corresponding SEM images (Figure 6.6B) indicate their locations. The negative-going signal signifies a pump-induced decrease in probe intensity. The magnitude of the signal depends on the presence of free carriers, and the decay of the pump-probe signal is attributed to a decrease in their concentration due to recombination and trapping events.

The electronic dynamics at the end of the rod differ dramatically from those observed at the interior, with the ends showing typically more intense signals with generally faster recombination rates than any other point in the structure. Spatial variation in the e-h recombination is particularly apparent in images obtained by fixing the pump-probe delay and monitoring $\Delta I$ as a function of position (Figure 6.6C). At early delays, the largest signal appears at the end of the rod. Less intense but localized regions of increased signal that coincide with the vertices are also observed. This modulation in the signal intensity is likely the result of cavity modes supported within the cross section of the structure.[62,78,107] At longer delays, the bright spot at the end diminishes, becoming less intense than the interior and eventually disappearing. Although there are examples of pump-probe microscopy that reveal differences from structure to structure, this is the first time that significant spatial variation in the dynamical response of an individual object has been observed.

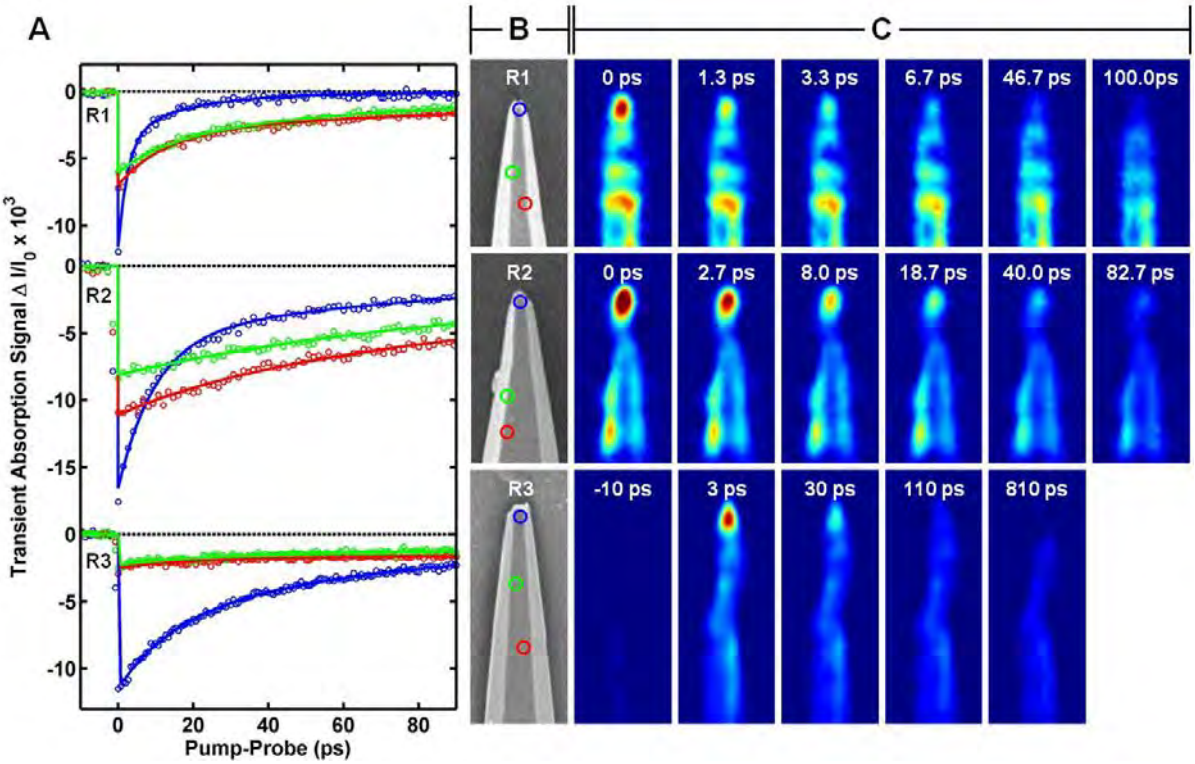

**Figure 6.6:** Pump-probe transients ($\Delta I/I$) collected from the end (blue) and two different points within the interior (green & red) from three different rods, **R1**, **R2** and **R3**. The locations of the collected points for the three transients are indicated in the corresponding SEM images (B), where the horizontal dimension of each image is 3 μm. The transients exhibit complex decay kinetics with fast (< 30 ps), intermediate (100-200 ps) and long (> 500 ps) components, whose relative amplitudes depend upon position. While the interior exhibits all three components with the fastest contributing only 25-50% of the total amplitude, the ends are dominated by this component, which accounts for 60-100% of the amplitude. (C) A series of transient absorption images ($\Delta I$) obtained at different pump-probe delays for the three rods. The series of pump-probe images show the rapid loss of the signal at the rod end, which ultimately decays to zero signal, while response from the interior persists significantly longer.

## 6.5. TIME-RESOLVED PHOTOLUMINESCENCE

Transient photoluminescence provides a direct view of the band-edge and trap-mediated e-h recombination processes. A spectral-temporal intensity map (Figure 6.7A) of the time resolved emission data collected from the end of a fourth rod, **R4**, shows a rich evolution of the band-edge emission, which shifts to the blue as it decays during the first 15-20 ps. Horizontal slices through the map correspond to snapshots of the emission spectrum at different times. The emission band appears with $\lambda_{max} \approx 400$ nm and then narrows as it blue shifts to a limiting position of 390 nm. Spectral shifts of this type are one signature of the electron-hole plasma (EHP) emission that occurs at high excitation intensities in II-IV semiconductors.[23] When the carrier density exceeds the Mott threshold, Coulombic and exchange interactions weaken the exciton binding and reduce the band gap (i.e., band gap renormalization). This phenomenon gives rise to a collective EHP state with an intense, red-shifted emission relative to the exciton. As electrons and holes recombine, the charge carrier

density decreases, and the excitonic state resumes, resulting in the time-dependent blue shift in the emission spectrum. The EHP to exciton transition that occurs during the first 15-20ps is consistent with observations in bulk and nanostructured ZnO.[112,113] Similar measurements performed at the interior show a significantly smaller spectral shift (Figure 6.7B) and decreased propensity for EHP formation compared to the end.

Vertical slices through this surface provide the photoluminescence decay (Figure 6.7C,D). The band-edge emission at the end of the rod decays with 22 and 88 ps components ($\tau_{avg}$ = 30 ps). The faster component is assigned to EHP recombination. The slower component is attributed to exciton emission, which emerges as the carrier density decreases and the exciton becomes most stable. The presence of the fast component in the interior is less obvious, and the slightly slower ($\tau_{avg}$ = 55 ps) decay is consistent with a smaller contribution from EHP recombination.

The decays of the pump-probe and trap emission are similar to each other at two locations (Figure 6.7C,D) but differ in their relationship to the band-edge emission. At the end of the rod, they match the decay of the band-edge emission at early times, suggesting that band-edge recombination is the primary cause of the decay in the free carrier population.

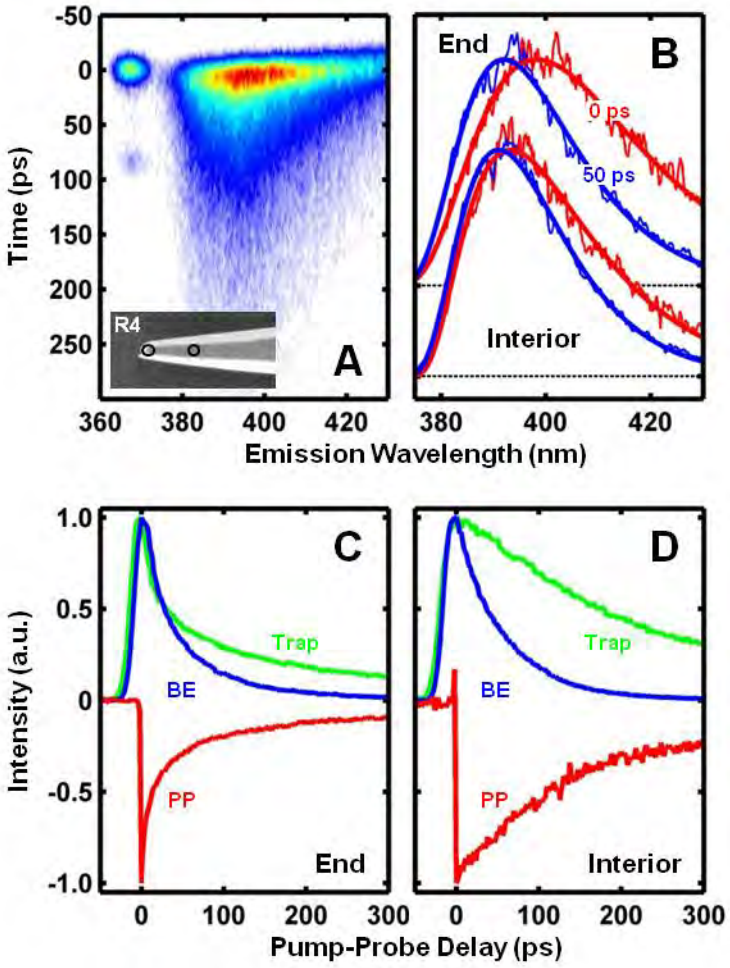


**Figure 6.7:** (A) Spectral-temporal intensity map of the emission collected from the end of the rod (**R4**) and dected using a streak camera. The main feature is the band-edge emission; the narrow peak at 365 nm is the second-harmonic of the excitation pulse and provides the instrument repose (17 ps). The inset shows the SEM image and locations of spectroscopic measurements (end versus interior). The vertical dimension of the SEM image is 3μm. (B) Time-resolved spectra obtained at 0 (red) and 50 ps (blue) from the end of the rod (upper set) and interior (lower set). (C,D) Comparison of the band-edge (BE), trap emission, and pump-probe (PP) data collected at the two points.

## 6.6. CONCLUSION

At the end of the structure, where the diameter is comparable to the size of the excitation spot (~350 nm), the physical confinement of the charge carriers helps maintain the

close interaction and leads to a prolonged overlap of the electron and hole wave functions, increasing the propensity for EHP formation. An increased correlation between the electrons and holes results in a greater oscillator strength (i.e. excitonic enhancement), and a brighter emission results.[114] This increase in oscillator strength could explain the more intense band-edge emission observed at the ends of the structure (Figure 6.1B).

Our recent report (REF) looked at the intensity of the band-edge and trap emission as a function of laser power at different locations. While the trap emission exhibited a linear increase. The band-edge emission intensity increased super-linearly with the carrier density. This upward curvature was more pronounced at the end of the rod, where the red shift in the emission spectrum and contribution from the EHP was the greatest. The intensity dependence of the BE emission indicated a spatially dependent propensity for EHP formation.

The interior is qualitatively different, however here, the band-edge emission decays more quickly compared to the pump-probe and trap emission, indicating that a significant free carrier population persists following the initial band-edge recombination events. In the interior of the structure carriers can migrate away from the excitation region, either through simple diffusion, or perhaps driven by internal fields that separate the electrons and holes. Based on the carrier diffusion constant in ZnO (~10 $cm^2$ $s^{-1}$),[29,30] we estimate a field-free diffusion length of ≈300 nm during the first 100 ps after excitation. Band-bending in ZnO is anticipated to result in electric fields and a depletion zone that extends a hundred nanometers or more into the bulk, which could increase this even further.(REF) The net result is a decrease in the charge density that makes it more difficult to form and sustain the EHP. Expansion of the charge cloud and the spatial separation of electrons and holes would make

EHP formation more difficult, suppress band-edge recombination (consistent with the emission spectra, Figure 6.1D), and lead to slower recombination.

Additionally, the differentiation in decay rates may well be influenced by where the carriers are originally generated in the structure. Initial finite-difference frequency domain (FDFD) simulations have shown that the fundamental electric field is preferentially concentrated within the center of the rod's cross section at diameters that are similar to the excitation size. As the cross section is increased the concentration of the electric field shifts towards periphery of the structure. The segregation of carriers based the structures cross section to support the electric field would strongly influence the potency of carrier confinement effect, even assuming that there is no spatial discrepancy in the number of initial carriers. Surface effects and band-bending hinder the stability of an EHP for carriers created around the periphery of the rod. Continuing FDTD simulations may provide additional insight into the spatial differ of EHP formation. While heterogeneous behavior in nanomaterials is often ascribed to polydispersity and variation between structures is observed here too, the presence of different dynamical behaviors from different parts of the same object cannot be overlooked.

## REFERENCES


(1) Demtröder, W. *Laser spectroscopy : basic concepts and instrumentation*; 3rd ed.; Springer: Berlin, 2003.
(2) Madelung, O. *Semiconductors--basic data*; 2nd rev. ed.; Springer: Berlin ; New York, 1996.
(3) Burda, C.; Chen, X. B.; Narayanan, R.; El-Sayed, M. A. *Chemical Reviews* **2005**, *105*, 1025.
(4) Ekimov, A. I.; Onushchenko, A. A. *Jetp Letters* **1981**, *34*, 345.
(5) Rossetti, R.; Nakahara, S.; Brus, L. E. *Journal of Chemical Physics* **1983**, *79*, 1086.
(6) Lieber, C. M. *Solid State Communications* **1998**, *107*, 607.
(7) Alivisatos, A. P. *Science* **1996**, *271*, 933.
(8) Peng, X. G.; Manna, L.; Yang, W. D.; Wickham, J.; Scher, E.; Kadavanich, A.; Alivisatos, A. P. *Nature* **2000**, *404*, 59.
(9) Vahala, K. J. *Nature* **2003**, *424*, 839.
(10) Becker, W. *Advanced time-correlated single photon counting techniques*; Springer: Berlin ; New York, 2005.
(11) O'Connor, D. V.; Phillips, D. *Time-correlated single photon counting*; Academic Press: London ; Orlando, 1984.
(12) Hamamatsu *http//sales.hamamatsu.com/assets/pdf/hpspdf/Guidetostreak.pdf*.
(13) Zewail, A. H.; Ortalan, V. *Journal of the American Chemical Society* **2011**, *133*, 10732.
(14) Pohl, D. W.; Denk, W.; Lanz, M. *Applied Physics Letters* **1984**, *44*, 651.
(15) Betzig, E.; Trautman, J. K. *Science* **1992**, *257*, 189.
(16) Binning, G.; Rohrer, H.; Gerber, C.; Weibel, E. *Physical Review Letters* **1982**, *49*, 57.
(17) Nechay, B. A.; Siegner, U.; Achermann, M.; Bielefeldt, H.; Keller, U. *Review of Scientific Instruments* **1999**, *70*, 2758.
(18) Siegner, U.; Achermann, M.; Keller, U. *Measurement Science & Technology* **2001**, *12*, 1847.
(19) Berweger, S.; Atkin, J. M.; Olmon, R. L.; Raschke, M. B. *Journal of Physical Chemistry Letters* **2010**, *1*, 3427.
(20) Neacsu, C. C.; Berweger, S.; Olmon, R. L.; Saraf, L. V.; Ropers, C.; Raschke, M. B. *Nano Letters* **2010**, *10*, 592.
(21) Suhling, K.; French, P. M. W.; Phillips, D. *Photochemical & Photobiological Sciences* **2005**, *4*, 13.
(22) Zipfel, W. R.; Williams, R. M.; Webb, W. W. *Nature Biotechnology* **2003**, *21*, 1368.
(23) Klingshirn, C. F.; Meyer, B. K.; Waag, A.; Hoffmann, A.; Geurts, J. M. M. *Zinc Oxide: From Fundamental Properties Towards Novel Applications*; Springer.
(24) Franken, P. A.; Weinreich, G.; Peters, C. W.; Hill, A. E. *Physical Review Letters* **1961**, *7*, 118.
(25) Bass, M.; Hill, A. E.; Franken, P. A.; Peters, C. W.; Weinreich, G. *Physical Review Letters* **1962**, *8*, 18.
(26) Wang, C. C.; Racette, G. W. *Applied Physics Letters* **1965**, *6*, 169.
(27) Giordmai.Ja; Miller, R. C. *Physical Review Letters* **1965**, *14*, 973.
(28) Boyd, R. W. *Nonlinear optics*; 3rd ed.; Academic Press: Burlington, MA, 2008.

(29) He, G.; Liu, S. *Physics of nonlinear optics*; World Scientific: Singapore ; River Edge, NJ, 1999.
(30) Sutherland, R. L. *Handbook of nonlinear optics*; Marcel Dekker: New York, 1996.
(31) Bloembergen, N. *Nonlinear optics*; 4th ed.; World Scientific: Singapore ; River Edge, N.J., 1996.
(32) Yariv, A. *Quantum electronics*; 3rd ed.; Wiley: New York, 1989.
(33) Yariv, A.; Yeh, P. *Optical waves in crystals : propagation and control of laser radiation*; Wiley: New York, 1984.
(34) Shen, Y. R. *The principles of nonlinear optics*; J. Wiley: New York, 1984.
(35) Klingshirn, C. F. *Semiconductor optics*; Springer: Berlin ; New York, 1995.
(36) Blair, D. P.; Sydenham, P. H. *Journal of Physics E-Scientific Instruments* **1975**, *8*, 621.
(37) *Operating Manual: SR830 DSP Lock-In Amplifier*; Stanford Research Systems.
(38) Trebino, R. *Frequency-resolved optical gating : the measurement of ultrashort laser pulses*; Kluwer Academic: Boston, 2000.
(39) Diels, J. C. M.; Fontaine, J. J.; Mcmichael, I. C.; Simoni, F. *Applied Optics* **1985**, *24*, 1270.
(40) Born, M.; Wolf, E. *Principles of optics : electromagnetic theory of propagation, interference and diffraction of light*; 7th (expanded) ed.; Cambridge University Press: Cambridge ; New York, 1999.
(41) Hecht, E.; Zaj*ac, A. *Optics*; 2nd ed.; Addison-Wesley Pub. Co.: Reading, Mass., 1987.
(42) Smith, W. J. *Modern optical engineering : the design of optical systems*; 2nd ed.; McGraw-Hill: New York, 1990.
(43) https://cvimellesgriot.com/products/Documents/TechnicalGuide/fundamental.
(44) https://cvimellesgriot.com/Products/Documents/TechnicalGuide/Gaussian.
(45) Richards, B.; Wolf, E. *Proceedings of the Royal Society of London Series a-Mathematical and Physical Sciences* **1959**, *253*, 358.
(46) Sheppard, C. J. R.; Gu, M. *Optik* **1990**, *86*, 104.
(47) *Landolt-Bornstein, New Series, Group III*; Rossler, U., Ed.; Springer: Heidelberg, 1999; Vol. 17B,22,41B.
(48) Thomas, D. G. *Journal of Physics and Chemistry of Solids* **1960**, *15*, 86.
(49) Haug, H.; Koch, S. W. *Quantum theory of the optical and electronic properties of semiconductors*; World Scientific, 2004.
(50) Zimmermann, R. *Many-particle theory of highly excited semiconductors*; BSB B.G. Teubner, 1988.
(51) Klingshirn, C.; Hauschild, R.; Fallert, J.; Kalt, H. *Physical Review B* **2007**, *75*.
(52) Zimmermann, R. *Physica Status Solidi B-Basic Research* **1988**, *146*, 371.
(53) Banyai, L.; Koch, S. W. *Zeitschrift Fur Physik B-Condensed Matter* **1986**, *63*, 283.
(54) Beni, G.; Rice, T. M. *Physical Review B* **1978**, *18*, 768.
(55) Inagaki, T. J.; Aihara, M. *Physical Review B* **2002**, *65*.
(56) Lu, J. G.; Fujita, S.; Kawaharamura, T.; Nishinaka, H.; Kamada, Y.; Ohshima, T.; Ye, Z. Z.; Zeng, Y. J.; Zhang, Y. Z.; Zhu, L. P.; He, H. P.; Zhao, B. H. *Journal of Applied Physics* **2007**, *101*.
(57) Roth, A. P.; Webb, J. B.; Williams, D. F. *Physical Review B* **1982**, *25*, 7836.
(58) Vashishta, P.; Kalia, R. K. *Physical Review B* **1982**, *25*, 6492.
(59) Versteegh, M. A. M.; Kuis, T.; Stoof, H. T. C.; Dijkhuis, J. I. *Physical Review B* **2011**, *84*.
(60) Ye, J. D.; Gu, S. L.; Zhu, S. M.; Liu, S. M.; Zheng, Y. D.; Zhang, R.; Shi, Y. *Applied Physics Letters* **2005**, *86*.
(61) Djurisic, A. B.; Leung, Y. H. *Small* **2006**, *2*, 944.

(62) Johnson, J. C.; Yan, H. Q.; Yang, P. D.; Saykally, R. J. *Journal of Physical Chemistry B* **2003**, *107*, 8816.
(63) Ozgur, U.; Alivov, Y. I.; Liu, C.; Teke, A.; Reshchikov, M. A.; Dogan, S.; Avrutin, V.; Cho, S. J.; Morkoc, H. *Journal of Applied Physics* **2005**, *98*, 041301.
(64) Xu, C. X.; Dai, J.; Wu, P.; Guo, J. Y.; Li, Z. H.; Shi, Z. L. *Applied Physics Letters* **2010**, *97*.
(65) Morkoc, H.; Strite, S.; Gao, G. B.; Lin, M. E.; Sverdlov, B.; Burns, M. *Journal of Applied Physics* **1994**, *76*, 1363.
(66) Nakayama, Y.; Pauzauskie, P. J.; Radenovic, A.; Onorato, R. M.; Saykally, R. J.; Liphardt, J.; Yang, P. D. *Nature* **2007**, *447*, 1098.
(67) Berger, V. *Journal of the Optical Society of America B-Optical Physics* **1997**, *14*, 1351.
(68) Rosencher, E.; Vinter, B.; Berger, V. *Journal of Applied Physics* **1995**, *78*, 6042.
(69) Ashkin, A.; Boyd, G. D.; Dziedzic, J. M. *Ieee Journal of Quantum Electronics* **1966**, *Qe 2*, 109.
(70) Cao, H.; Hall, D. B.; Torkelson, J. M.; Cao, C. Q. *Applied Physics Letters* **2000**, *76*, 538.
(71) Dolgova, T. V.; Maidykovski, A. I.; Martemyanov, M. G.; Fedyanin, A. A.; Aktsipetrov, O. A.; Marowsky, G.; Yakovlev, V. A.; Mattei, G. *Applied Physics Letters* **2002**, *81*, 2725.
(72) Fiore, A.; Rosencher, E.; Bravetti, P.; Nagle, J.; Berger, V. *Nature* **1998**, *391*, 463.
(73) Mondia, J. P.; van Driel, H. M.; Jiang, W.; Cowan, A. R.; Young, J. F. *Optics Letters* **2003**, *28*, 2500.
(74) Pellegrini, V.; Colombelli, R.; Carusotto, I.; Beltram, F.; Rubini, S.; Lantier, R.; Franciosi, A.; Vinegoni, C.; Pavesi, L. *Applied Physics Letters* **1999**, *74*, 1945.
(75) Simonneau, C.; Debray, J. P.; Harmand, J. C.; Vidakovic, P.; Lovering, D. J.; Levenson, J. A. *Optics Letters* **1997**, *22*, 1775.
(76) Wang, Z. L. *Journal of Physics: Condensed Matter* **2004**, *16*, R829.
(77) Liu, J. Z.; Lee, S.; Ahn, Y. H.; Park, J. Y.; Koh, K. H.; Park, K. H. *Applied Physics Letters* **2008**, *92*, 263102.
(78) Nobis, T.; Grundmann, M. *Physical Review A: Atomic, Molecular, and Optical Physics* **2005**, *72*, 063806.
(79) Nobis, T.; Kaidashev, E. M.; Rahm, A.; Lorenz, M.; Grundmann, M. *Physical Review Letters* **2004**, *93*, 103903.
(80) Ruhle, S.; van Vugt, L. K.; Li, H. Y.; Keizer, N. A.; Kuipers, L.; Vanmaekelbergh, D. *Nano Letters* **2008**, *8*, 119.
(81) Sun, L. X.; Chen, Z. H.; Ren, Q. J.; Yu, K.; Bai, L. H.; Zhou, W. H.; Xiong, H.; Zhu, Z. Q.; Shen, X. C. *Physical Review Letters* **2008**, *100*, 156403.
(82) van Vugt, L. K.; Ruhle, S.; Ravindran, P.; Gerritsen, H. C.; Kuipers, L.; Vanmaekelbergh, D. *Physical Review Letters* **2006**, *97*, 147401.
(83) Cheng, B.; Shi, W. S.; Russell-Tanner, J. M.; Zhang, L.; Samulski, E. T. *Inorganic Chemistry* **2006**, *45*, 1208.
(84) Li, F.; Li, Z.; Jin, F. J. *Materials Letters* **2007**, *61*, 1876.
(85) Johnson, J. C.; Yan, H. Q.; Schaller, R. D.; Petersen, P. B.; Yang, P. D.; Saykally, R. J. *Nano Letters* **2002**, *2*, 279.
(86) Czekalla, C.; Sturm, C.; Schmidt-Grund, R.; Cao, B. Q.; Lorenz, M.; Grundmann, M. *Applied Physics Letters* **2008**, *92*, 241102.
(87) Wang, D.; Seo, H. W.; Tin, C. C.; Bozack, M. J.; Williams, J. R.; Park, M.; Tzeng, Y. *Journal of Applied Physics* **2006**, *99*, 093112.
(88) Wiersig, J. *Physical Review A: Atomic, Molecular, and Optical Physics* **2003**, *67*, 023807.

(89) Zhang, Y.; Zhou, H. J.; Liu, S. W.; Tian, Z. R.; Xiao, M. *Nano Letters* **2009**, *9*, 2109.
(90) Taflove, A.; Hagness, S. C. *Computational electrodynamics : the finite-difference time-domain method*; 3rd ed.; Artech House: Boston, 2005.
(91) Farjadpour, A.; Roundy, D.; Rodriguez, A.; Ibanescu, M.; Bermel, P.; Joannopoulos, J. D.; Johnson, S. G.; Burr, G. W. *Optics Letters* **2006**, *31*, 2972.
(92) Anderson, A.; Deryckx, K. S.; Xu, X. J. G.; Steinmeyer, G.; Raschke, M. B. *Nano Letters* **2010**, *10*, 2519.
(93) Okamoto, K.; Scherer, A.; Kawakami, Y. *Applied Physics Letters* **2005**, *87*.
(94) Terada, Y.; Yoshida, S.; Takeuchi, O.; Shigekawa, H. *Nature Photonics* **2010**, *4*, 869.
(95) Carey, C. R.; Yu, Y. H.; Kuno, M.; Hartland, G. V. *Journal of Physical Chemistry C* **2009**, *113*, 19077.
(96) Djurisic, A. B.; Kwok, W. M.; Leung, Y. H.; Phillips, D. L.; Chan, W. K. *Journal of Physical Chemistry B* **2005**, *109*, 19228.
(97) Fujino, T.; Fujima, T.; Tahara, T. *Journal of Physical Chemistry B* **2005**, *109*, 15327.
(98) Gundlach, L.; Piotrowiak, P. *Optics Letters* **2008**, *33*, 992.
(99) Huang, L. B.; Hartland, G. V.; Chu, L. Q.; Luxmi; Feenstra, R. M.; Lian, C. X.; Tahy, K.; Xing, H. L. *Nano Letters* **2010**, *10*, 1308.
(100) Johnson, J. C.; Knutsen, K. P.; Yan, H. Q.; Law, M.; Zhang, Y. F.; Yang, P. D.; Saykally, R. J. *Nano Letters* **2004**, *4*, 197.
(101) Song, J. K.; Willer, U.; Szarko, J. M.; Leone, S. R.; Li, S.; Zhao, Y. *Journal of Physical Chemistry C* **2008**, *112*, 1679.
(102) Cadby, A.; Dean, R.; Fox, A. M.; Jones, R. A. L.; Lidzey, D. G. *Nano Letters* **2005**, *5*, 2232.
(103) Fu, D.; Ye, T.; Matthews, T. E.; Grichnik, J.; Hong, L.; Simon, J. D.; Warren, W. S. *Journal of Biomedical Optics* **2008**, *13*.
(104) Polli, D.; Grancini, G.; Clark, J.; Celebrano, M.; Virgili, T.; Cerullo, G.; Lanzani, G. *Advanced Materials* **2010**, *22*, 3048.
(105) House, R. L.; Mehl, B. P.; Kirschbrown, J. R.; Barnes, S. C.; Papanikolas, J. M. *Journal of Physical Chemistry C* **2011**, *115*, 10806.
(106) Lin, J. H.; Chen, Y. J.; Lin, H. Y.; Hsieh, W. F. *Journal of Applied Physics* **2005**, *97*.
(107) Mehl, B. P.; House, R. L.; Uppal, A.; Reams, A. J.; Zhang, C.; Kirschbrown, J. R.; Papanikolas, J. M. *Journal of Physical Chemistry A* **2010**, *114*, 1241.
(108) Bauer, C.; Boschloo, G.; Mukhtar, E.; Hagfeldt, A. *Chemical Physics Letters* **2004**, *387*, 176.
(109) Okamoto, K.; Fujita, S.; Kawakami, Y.; Scherer, A. *Physica Status Solidi B-Basic Research* **2003**, *240*, 368.
(110) Okamoto, K.; Inoue, K.; Kawakami, Y.; Fujita, S.; Terazima, M.; Tsujimura, A.; Kidoguchi, I. *Review of Scientific Instruments* **2003**, *74*, 575.
(111) Said, A. A.; Sheikbahae, M.; Hagan, D. J.; Wei, T. H.; Wang, J.; Young, J.; Vanstryland, E. W. *Journal of the Optical Society of America B-Optical Physics* **1992**, *9*, 405.
(112) Hendry, E.; Koeberg, M.; Bonn, M. *Physical Review B* **2007**, *76*.
(113) Yamamoto, A.; Kido, T.; Goto, Y. F.; Chen, Y.; Yao, T.; Kasuya, A. *Applied Physics Letters* **1999**, *75*, 469.
(114) Pavesi, L.; Staehli, J. L.; Capozzi, V. *Solid State Communications* **1987**, *61*, 321.